UC Berkeley
UC Berkeley Electronic Theses and Dissertations

Title

Atomistic-informed Finite Temperature Crystal Plasticity Finite Element Modeling of Body-centered Cubic Single Crystals

Permalink

https://escholarship.org/uc/item/5xt6018n

Author

xie, yuxi

Publication Date

2021

Peer reviewed|Thesis/dissertation

Atomistic-informed Finite Temperature Crystal Plasticity Finite Element Modeling of
Body-centered Cubic Single Crystals

by

Yuxi Xie

A dissertation submitted in partial satisfaction of the

requirements for the degree of

Doctor of Philosophy

in

Engineering – Civil and Environmental Engineering

in the

Graduate Division

of the

University of California, Berkeley

Committee in charge:

Professor Shaofan Li, Chair
Professor Khalid M. Mosalam
Professor Lin Lin

Summer 2021

Atomistic-informed Finite Temperature Crystal Plasticity Finite Element Modeling of Body-centered Cubic Single Crystals

Abstract

Atomistic-informed Finite Temperature Crystal Plasticity Finite Element Modeling of
Body-centered Cubic Single Crystals

by

Yuxi Xie

Doctor of Philosophy in Engineering – Civil and Environmental Engineering

University of California, Berkeley

Professor Shaofan Li, Chair

Crystal plasticity is a long-standing problem in computational materials. Understanding
deep mechanism of plasticity, such as dislocation, multiplication, interaction, has been a
great challenge of major scientific significance since there exist many physical and technical
difficulties.
It is believed that plasticity in a crystal is strongly influenced by the aggregated dislocations.
The aggregated dislocations usually form definite dislocation networks or substrates when
plastic loading happens and the networks or substrates are usually called as dislocation
patterns. It is commonly known that dislocation patterns and their interactions determine
plasticity of crystalline material. Based on lots of experimental observations, it is found
that under the same loading and boundary conditions, the specific type of atomic crystal
structures usually generates very similar dislocation patterns. Therefore, it is believed that
the dislocation patterns emerged in crystalline materials are strongly related to the atomic
crystal structures of crystalline materials at the beginning stage of plastic deformation.
On the other hand, for metallic materials, especially Body-centered Cubic (BCC) crystal
materials, the thermally-activated dislocation glide has a tight link to crystal plasticity, such
as constitutive relation (stress-strain curve), screw dislocation glide and temperature-induced
Peierls-stress. Because the thermally-activated screw dislocation glide results to thermally-
induced Peierls-stress and yield stress decreasing.
In this dissertation, it is developed that a temperature-dependent higher-order Cauchy-
Born (THCB) rule for Multiscale Crystal Defects Dynamics (MCDD) of crystalline solids
based on harmonic approximation. The THCB rule is employed to develop an atomistic-
informed constitutive model and the corresponding higher order stress are used to model
crystal plasticity of single crystals. It is shown in the dissertation that the developed finite
temperature atomistic-informed crystal plasticity finite element method is able to capture the
temperature-dependent dislocation substructure and hence crystal plastic deformation. The
main contributions and novelties of the present work are highlighted by following findings: (1)
A temperature-dependent higher-order Cauchy-Born rule and an atomistic-informed strain

gradient theory have been developed, and the corresponding temperature-related higher-order stress and elastic tensor formulations are derived; (2) The finite temperature MCDD provides an atomistic-informed crystal plasticity finite element method that can simulate anisotropic crystal plasticity in any orientation within the stereographic triangle at micron scale and above; (3) The developed multiscale crystal defect dynamics (MCDD) is able to capture the non-Schmid effects of BCC single crystals; (4) The developed multiscale crystal defects dynamics (MCDD) is able to capture the size effect of single crystal plasticity, and (5) The finite temperature MCDD can simulate the temperature dependent dislocation substructure, and it captures cross-slip in single crystal at low temperature ($\sim 20 K^o$) and captures dislocation cell structures at high temperature ($\sim 500 K^o$).

To my mother

Contents

List of Figures

List of Tables

Acknowledgments

I would like to be grateful to Professor Shaofan Li for his offering the precious opportunity to study at Berkeley. He helped me each time when I came across difficulties in research as well as in life. I feel so lucky to meet such a wise and kind person as my advisor and worked with him during my Ph.D. period.

I owe my special thanks to Professor Khalid M. Mosalam and Professor Lin Lin for serving on my thesis committee. The Finite Element Analysis courses I took from Professor Khalid M. Mosalam and numerical analysis courses from Professor Lin Lin have provided me the theoretical foundation and mathematical implementation skills for my research.

I really appreciate my mother and my family for supporting and helping me so that I always have strength from their encouragement.

I would like to thank my colleagues Dandan Lyu, Luwen Zhang, Tiange Li, Haicheng Yu, Xin Lai, Jiale Yan and Chao Wang among others for their help and kindness, which is nice experience at Berkeley Campus.

Chapter 1

Introduction

1.1 Motivation and Background

Crystal plasticity is a very common physical phenomenon, no matter a metal shovel is bent in normal lives or residual strain of steel beam under distortion in engineering application (see Fig.1.1(a)-(b)).

With deeper understanding of crystal plasticity, scholars realize that the crystalline atomistic dislocations are responsible for its plastic behavior (Fig.1.1(c)). At very beginning of studying crystal plasticity, some phenomenological models were developed to describe plastic behavior of metals. But this kind of methods require parameters fitting and experimental calibration so that they are NOT mechanism-based methods.

With the help of computation technologies, massive parallel simulation becomes possible. Therefore, two bottom-up methods based on dislocation theory have been proposed. The first method is atom-level method including Molecular Dynamics and first-principle method. For Molecular Dynamics simulation, massive parallel computation makes it possible that micron-scale objects simulation but larger size becomes bottleneck of this method. Alterna-

(a)   (b)   (c)
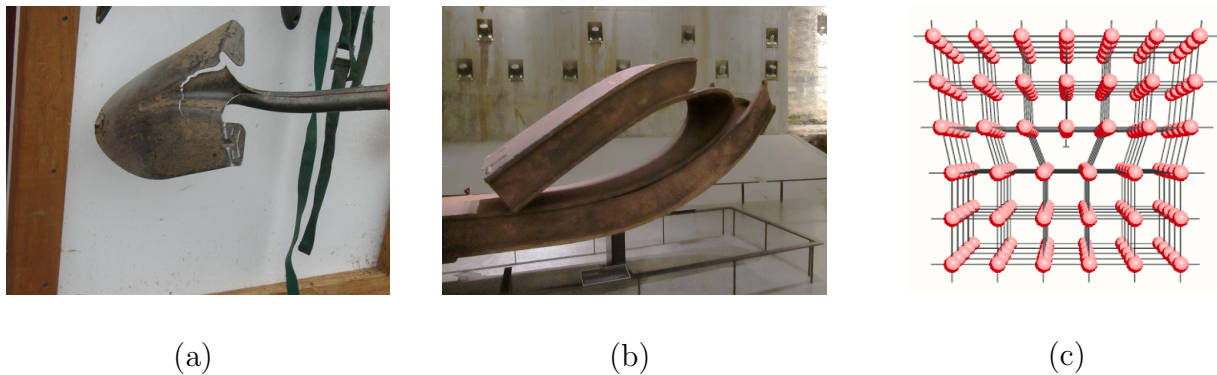
Figure 1.1: Crystal plasticity: (a) a shovel bent; (b) metal plate bent([1]); (c) atomic dislocation.
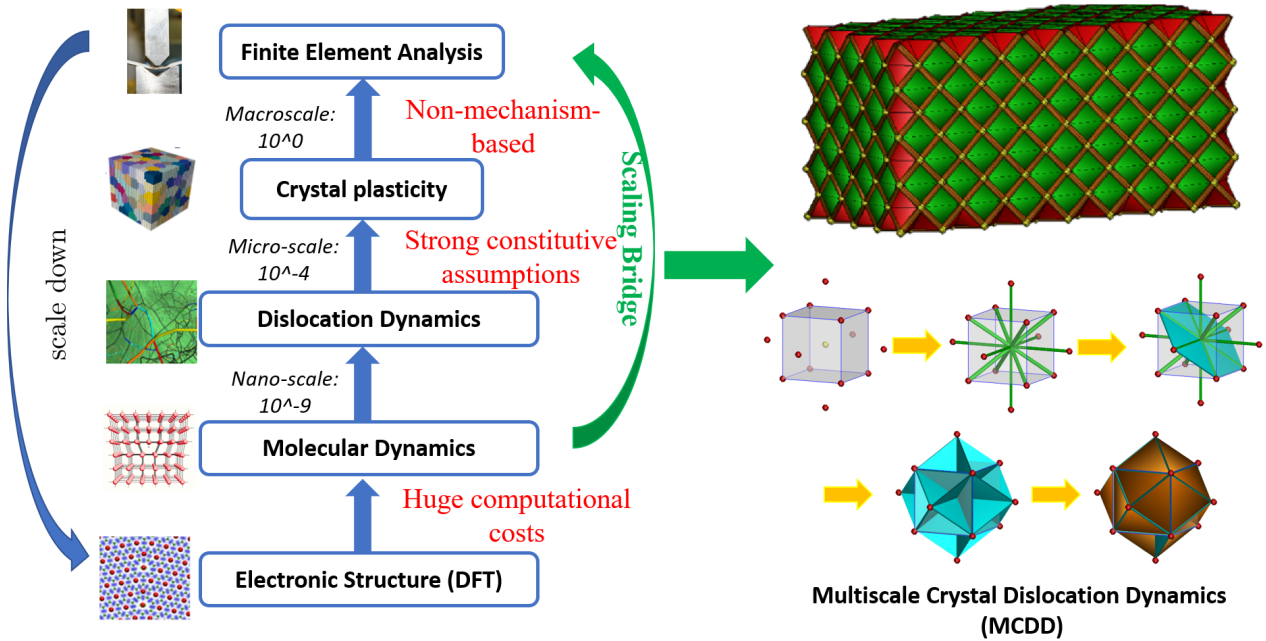
Figure 1.2: Hierarchical scale crystal plasticity modeling methods.

tively, another method, Dislocation Dynamics attempting to characterize behavior of aggregate dislocation ensembles at mesoscale becomes popular. However, Dislocation Dynamics also suffers shortcomings, such as assumption of linear isotropic elasticity and undefined dislocation cut-off radius (see Fig.1.2).

Dislocations in crystalline materials lead to crystal plasticity, nevertheless, the plastic flow in a crystal is not determined by the motion of a single individual dislocation, but by the evolution of aggregated dislocations. Even though the interactions of dislocations are complex statistical and stochastic events, often times, definite dislocation substructures may emerge during plastic deformation, which is also called as the dislocation pattern. It is the interaction of dislocation patterns that determines plastic flow or crystal plasticity e.g. [13, 14].

Dislocation pattern distribution can partition the entire plastically deformed crystal into quasi-periodic dislocation-rich and dislocation-poor regions, and by viewing them from different directions or perspectives, we may see different geometric patterns, such as cells, veins, labyrinth, ladders, which may be viewed as the building block to form complex structured networks of aggregated dislocation distributions. More importantly, it is now a consensus that it is the dislocation substructures or deformation micro-structures and their evolution that determine the plastic hardening parameters and flow stress e.g. [15, 16] rather than a single or a few dislocations. By studying the evolution of dislocation patterns, we will be able to gain deep understanding of important physical processes in crystal plasticity such as

strain hardening, strain localization, and the related material properties at macroscale.
Since 1980s, study of dislocation pattern has been an active field in materials science research.
Most developments before 2010 have been reviewed in [17, 18]. A comprehensive review of
the recent development on dislocation pattern dynamics is presented in [19].
Focusing more on the recent literature, we would like to point out some noteworthy work in
the recent years. An excellent work done by Li et al. [20] has systematically investigated dis-
location patterns in FCC crystals under cyclic loading, in which the authors provided some
experimental evidences for well-defined and lattice-like distribution dislocation microstruc-
ture. Later on, the same authors argued that these lattice-like dislocation patterns are linked
with the original crystal lattice with same standing wave effect and fractal structure [21].
Recently, by various diffraction conditions in the high angular resolution cross-correlation
based electron backscattering diffraction (CC-EBSD), quasi in-situ electron channelling con-
trast imaging has been used by An and Zaefferer [22] to investigate the formation and evolu-
tion of dislocation patterns under low cycle fatigue of a Steel specimen, and they found that
junctions formed by different slip systems interaction help the dislocation dipoles to form
and even lead to dislocation walls formation. It clearly elucidated the formation process of
dislocation patterns from the original crystal lattice structure.
From modeling and simulation perspective, Groma et al. [23] studied dislocation patterns
in a two-dimensional continuum dislocation theory. Hu et al. [24] used discrete dislocation
dynamics (DDD) simulations to investigate dislocation pattern formation in single crystalline
copper pillar and study the related yielding mechanisms. Moreover, Ispanovity et al. [25]
developed a stochastic continuum model for statistically stored and geometrically necessary
dislocation densities. They showed that dislocation pattern characteristics that include the
formation of dipolar dislocation walls; and Zhou et al. [26] developed a machine learning
approach to resolve the local dislocation microstructure.
On the other hand, multiscale crystal plasticity theory is another active research area in com-
putational materials science. Since 1990s, it has been continuously a forward-looking tend in
materials science research to reduce empiricism in modeling and simulation. The atomistic
and multiscale based modeling and simulation in crystal plasticity have been developing and
thriving. Here we list a few multiscale crystal plasticity finite element models (CPFEM): A
hierarchical multiscale modeling method is proposed by Groh et al. [27] and this method can
predict the working hardening of FCC crystals without experiments; A concurrent atomistic
continuum methodology called CAC has been proposed by Xiong et.al [28] who used EAM
force field and an adaptive mesh refinement to simulate dislocation nucleation and migration
of FCC crystal structures; Involving non-Schmid stress dependent slip with strain rate effect
and temperature, an atomistically-informed crystal plasticity finite element model on body-
centered-cubic (BCC) α-Fe has been proposed by Lim et al. [29], and Amodeo et al. [30]
have developed an atomistically-informed multiscale crystal plasticity formulation to model
the pressure-dependent plasticity in MgO.
Instead of coupling with atomistic modeling, some authors coupled discrete dislocation dy-
namics with crystal plasticity finite element formulation. For examples, aiming to damage
and deformation caused by high strain rate in single crystal, a ductile failure framework

based on dislocation viscoplasticity has been proposed by Nguyen et.al [31]; and inspired by the model of integrating 3D dislocation dynamic (DD) simulation with the Finite Element Method (FEM), the Discrete-Continuous Model (DCM) has been proposed by Vattre et.al [32] to simulate flow of material plasticity at the sub-micron scale.

Recently, Li et. al [33] firstly developed a *Multiscale Crystal Defect Dynamics* (MCDD) to systematically study the dynamics of dislocation patterns, in which they model dislocation pattern as the corresponding three types of dual lattice process zones (see Fig.1.2). The proposed *Multiscale Crystal Defect Dynamics* is in fact an atomistically informed higher order strain gradient nonlinear finite element crystal plasticity theory and formulation. To construct an atomistically informed higher order strain gradient theory, a higher order Cauchy-Born model, is developed by using the interatomic potential to model the lattice process zones as locally higher-order hyper-elastic media. When the stress and deformation state inside the crystal, locally or globally, reach to certain level, their relationship becomes irreversible, i.e. developing plastic deformation. Lyu and Li in [34] employed discrete exterior calculus and algebraic topology theory to study the geometric and topological structures of the dislocation patterns, and later they [35] proposed a new notion of *Geometrically Compatible Dislocation Pattern (GCDP)* and demonstrated the similarity between GCDP and the real physical dislocation pattern of crystalline materials observed at the early stage. The so-called geometrically compatible dislocation pattern is defined as the dislocation substructure that mimics the microstructure of the dual lattice based on the original crystal lattice structure. This is because the initial dislocation formation or crystal defect always occurs on a lattice plane as forms of lattice complex (simplicial complex), it is reasonable to postulate that their aggregation will form a dual lattice complex, or CW complex [36, 34]. Such geometric objects have been occasionally mentioned or reported in the literature, e.g [37, 38] without systematical studies. Subsequently, Zhang et al [39] further investigated of *Geometrically Compatible Dislocation Pattern* in body-center-crystal (BCC) structure.

1.2 Temperature-dependent Dislocation Patterns

Individual dislocation tends to form randomly but statistical number of dislocations tend to converge to some specific regions based on different crystal lattice structures at the beginning of material plasticity. Different materials, different experimental conditions usually lead to completely different dislocation patterns but the dislocation-rich regions sandwiched by dislocation-poor regions are the basic observation characteristics of dislocation patterns.

The shapes of dislocation patterns are not only influenced by crystal lattice structures but also by external effects. Temperature is one of the most significant factors. There are many experiments showing that different dislocation patterns at high or low temperature:

Shields et al [2] studied that Ta single crystals with different orientations were stretched or compressed at $77K$ and $4.2K$. It was found that increasing temperature from $4.2K$ to $77K$ eliminated slip occurrence but promoted dislocation twinning (see Fig.1.3(a)). Spitzig et al [3] conducted tension tests of Ta single crystals at $373K$ and compared to [40] entangled

dislocation cells appeared at much higher temperature (see Fig.1.3(b)). Papanikolaou et al [4] provided a comprehensive review on the relation between avalanches and plastic flow in crystal plasticity including experimental observations, theoretical models and computational methods. The defomed Mo alloy containing 0.5% Ti and 0.1% Zr showed rafts of loops at 350^oC (see Fig.1.3(d)) and the deformed single crystal Mo showed dislocation channels at 50^oC (see Fig.1.3(c)).

Marchenko et al [5] proposed a phenomenological strain aging model considering slip systems in HCP crystals to model static crystal plasticity and strain aging. The experimental observations were provided as validation of proposed scenario, in which super kinks appeared in α-Ti at 20^oC (see Fig.1.4(a)) while those kinks were replaced by dislocation dipoles and debris in α-Ti at higher temperature 150^oC (see Fig.1.4(b)). Sawkill et al [6] conducted a shear test on gold single crystal and a tension comparison between gold and aluminium crystals. From the experimental results (see Fig.1.4(c)-(d)), it is found that there are no obvious difference of dislocation patterns in Au single crystals at room temperature and high temperature (575^oC).

From those experimental observations, one is found that compared to Face-centered Cubic (FCC) crystals and Hexagonal-close Pack (HCP) crystals, Body-centered Cubic (BCC) crystals show stronger temperature-dependency, i.e. high\low temperature can obviously change dislocation patterns in BCC crystals and this is the investigation focus of the dissertation.

1.3   Overview of the Dissertation

The present work is aimed to accomplish the following four objectives: (1) *Incorporate temperature dependence into atomistically-informed high order strain gradient crystal plasticity formulation.* Even though, this has been attempted before e.g. [29, 41], they are basically hierarchial multiscale CPFEM approach but they are not con-current multiscale strain gradient approach. (2) *Demonstrate MCDD's capacity to capture distinct dislocation patterns under different temperature conditions.* There is a misconception about MCDD, which some researchers thought that the main technique of MCDD was only the embedment of a particular dislocation pattern into a finite element mesh. Similar to the cohesive zone model (CZM), MCDD embeds almost all kinematic possible dislocation patterns into the FE mesh except restriction on FEM mesh resolution. In this work, we would like to show under different temperature conditions, the same MCDD finite element mesh may capture different dislocation substructures; (3) *Demonstrate MCDD as an anisotropic strain gradient crystal plasticity model that can automatically capture the non-Schmid effects*, and (4) *Demonstrate MCDD's computational efficiency on calculating large scale $(> 1\mu m^3)$ size specimens and hence MCDD's capacity on simulating size effect of crystal plasticity.*

In Chapter 1, we will talk about motivation and current research background of this dissertation, in which the significance of current research and past scientific progress on crystal plasticity are discussed.

Due to the fact that the MCDD method is mesh-dependent, therefore in Chapter 2, we

(a)

(b)

(c)

(d)
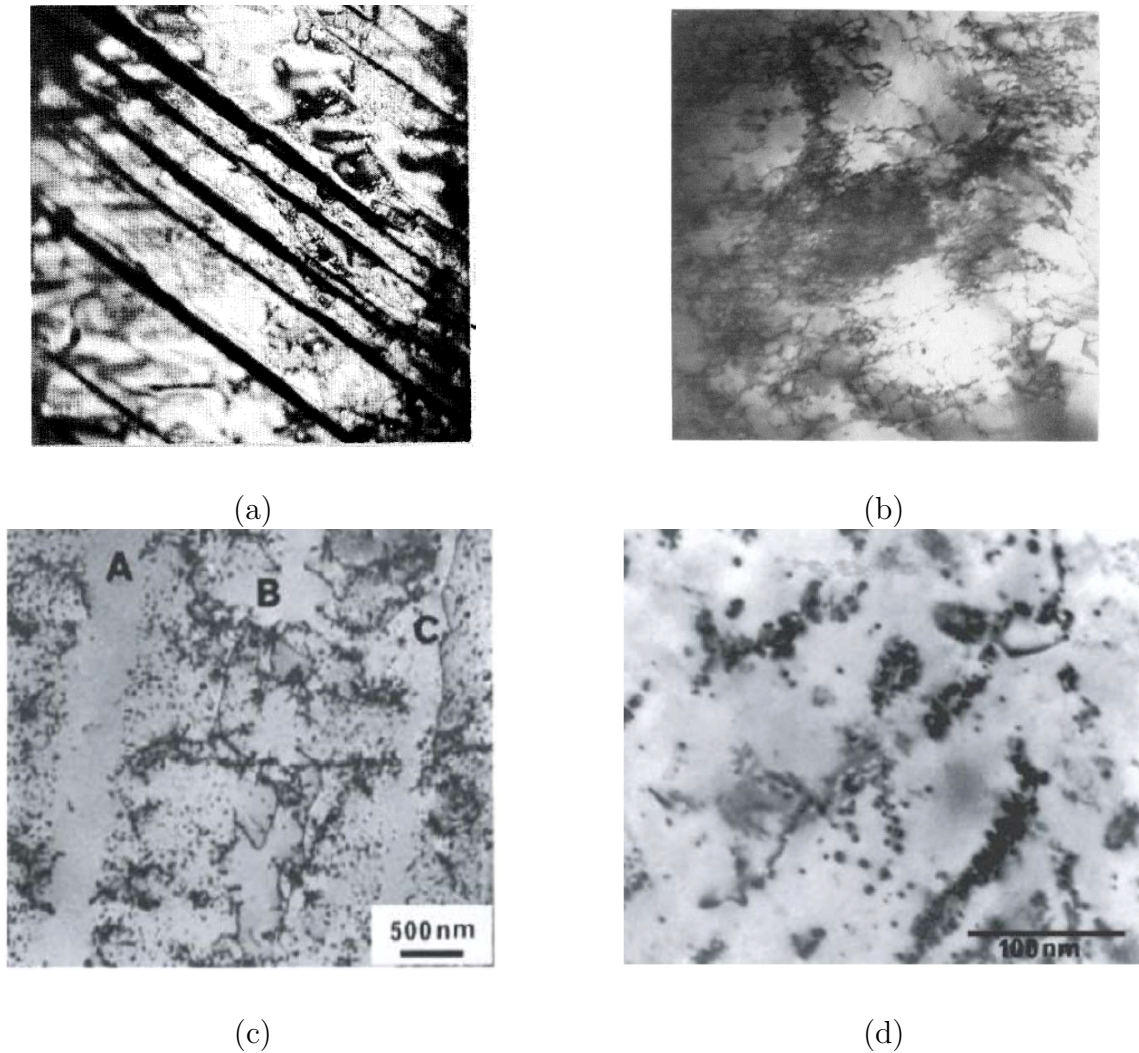
Figure 1.3: BCC crystal dislocation patterns under high\low temperature: (a) dislocation twins in Ta at $4.2K$ [2] (Reuse Permission by Elsevier: License Number 5066160715756); (b) dislocation cells in Ta at $373K$ [3] (Reuse Permission by Elsevier: License Number 5066161033777); (c)-(d) dislocation channels in Mo at 50^oC and dislocation rafts of loops in Mo at 350^oC [4].
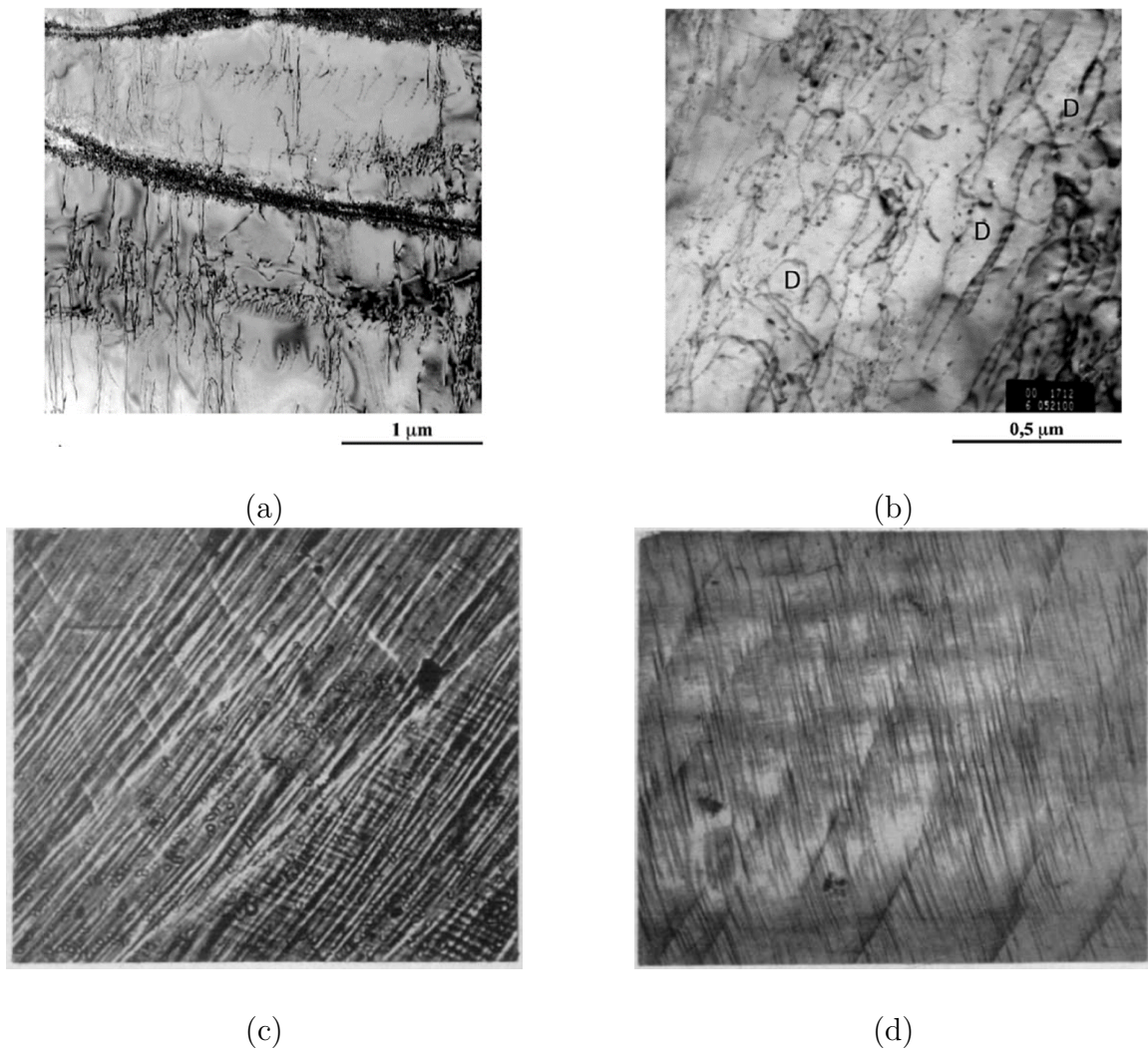
Figure 1.4: HCP and FCC crystal dislocation patterns under high\low temperature: (a)-(b) super-kinks in Ti at 20^oC and dislocation dipoles and debris in Ti at 150^oC [5] (Reuse Permission by Elsevier: License Number 5066170446909); (c)-(d) kink bands in Au at room temperature and at 575^oC [6] (Reuse Permission by Elsevier: License Number 5066170725766).

first give a introduction to mesh-related concepts and methods, including the Dual Lattice Process Zone (DLPZ) model, creating dual lattice tessellation of BCC crystal structures intuitively and basic theory of discrete exterior calculus and algebraic topology applied on creating super dual lattices of BCC crystals quantitatively.

In Chapter 3, the notion of *Geometrically Compatible Dislocation Pattern (GCDP)* is put forth based on lots of experimental observations of crystalline materials. The introduction of notion GCDP gives physical explanation to the observation that under the same loading and boundary conditions similar crystalline materials usually have similar dislocation pattern at the initial plastic deformation. So that it shows that the super dual lattice tessellation of crystalline materials is physics-informed Finite Element mesh method.

In Chapter 4, we discussed a particular finite temperature atomistic-informed multiscale constitutive model for a single crystal. Introducing Helmholtz free energy and employing local quasi-harmonic model can effectively couple thermally-induced energy and mechanically-induced energy in constitutive equation. And to realize hierarchical process zone activation during plasticity, the corresponding temperature-dependent higher-order Cauchy-Born rule in different order process zone elements is discussed.

Based on Finite Element mesh and corresponding constitutive relations in different elements, Chapter 5 mainly focused on the implementation of Finite Element formulation of MCDD method as a continuum method in computer. Besides, five quadratic serendipity element types (including quadratic hexagonal prism element and quadratic truncated octahedron element) are introduced to MCDD model and more obvious nonlinear higher order Cauchy-Born rule effects are displayed in a compression benchmark test.

In Chapter 6, we present some MCDD numerical simulation results, and compare them with the corresponding Molecular Dynamics (MD) simulation results. First, a uniaxial tension and a pure shear are conducted to validate the MCDD model by comparing with the results of Molecule Dynamics. Then to show MCDD is a first-principle based method rather than phenomenological one, predicting the violation of Schmid law, i.e. non-Schmid law, is necessary. Therefore, a benchmark test of the orientation effects of α-Ta crystal at grain scale and a benchmark test of non-Schmid effect are conducted. Thirdly, a preliminary study on size-effect of mesoscale crystal plasticity of MCDD simulation is conducted. Last, it is well-known that Body-centered Cubic (BCC) single crystal shows very strong temperature-dependent effect on crystal plasticity so that the last numerical example is to show very different dislocation substructures appearing under low temperature and high temperature. Finally, we comment the progress of this research, discuss some remaining issues, and conclude the study in Chapter 7.

Chapter 2

Crystal Lattice-informed Finite Element Mesh of MCDD Model

One of characteristics of MCDD method is physically mesh-dependency. "Physically" indicates Finite Element mesh of MCDD model is not only numerically meaningful but also physics-informed. This Chapter will introduce the related concepts and meshing method including the concept of Dual Lattice Process Zone (DLPZ), dual lattice tessellation of Body-centered Cubic (BCC) crystal and discrete exterior calculus and algebraic topology applied on creating super dual lattice of BCC crystals quantitatively.

2.1   Overview of Dual Lattice Process Zone

It is commonly to use lower dimensional objects to describe and model the defects and their evolution in crystalline materials. For example, in [36], the discrete static mechanics of crystal lattice is proposed to model defects in crystalline solids and those geometrical objects are lower dimensional: vertex is usually used to model void(0-cell) which is 0-dimensional; line segment is usually used to model dislocation line(1-cell) which is 1-dimensional and surface(2-cell) is usually used to model slip plane which is 2-dimensional. The similar defects modeling can be found in [42]. On the contrary, there are drawbacks preexisting in the lower dimensional idealization or modeling of defects, because it is just a geometrical simplification rather than the physical reality of defect mechanics. From the physics point of view, we all know that the dislocation has very complex three-dimensional structure, especially for its core structures, e.g.[43] and by using a single point to represent the real three-dimensional defects will lead to structural and physical information loss of defects and cause failure of predicting behaviors of defects. From the mathematical perspective, its existence requires justification. But for the simplification, lower dimension object without scales prevents itself from being related to defects in crystalline solids. To solve the physical and mathematical dilemma and offering a new model that can fully reserve the physical information of defects in crystalline matters and have complete mathematical justification, we proposed a three-

dimensional geometrical model to simulate the defects. And this model is called as dual lattice process zone (DLPZ) model from following series publications [44][45][46][47].

2.2 Concepts and Construction Steps of DLPZ Model

The most natural thought to model the spatial distribution of atoms is to take each atom location as a geometrical vertex and consider the atom bonds connecting atoms as the geometrical edges. Therefore, the corresponding crystal structures will have space rather than vertex, line or surface. For example, the atoms sit at the locations of vertices of lattice structures in Face-centered Cubic (FCC), Body-centered Cubic (BCC) and Hexagonal Close-pack (HCP) lattice. In addition to the method above, there is another description for crystal lattice structures in crystallographic in which the vertex is no longer at the atom site (as shown in Fig.2.1(a)). It is found that the centre position of Voronoi cell happens to be consistent with crystal atoms' positions and therefore the new partition (dual-lattice partition) is termed as Voronoi-Dirichlet tessellation due to the Voronoi cell. The convex Voronoi cell is called as Voronoi-Dirichlet Polyhedron (VDP). The union of all VDPs also partition the whole two-dimensional or three dimensional space.

Fig.2.2 shows the complete steps to have dual lattice process zone tessellation:

(1) Based on crystal lattices of whole atoms in 2D or 3D space, we can have corresponding dual lattice as shown in Fig.2.1(a);

(2) Then we shall scale the VDPs down (i.e. blue hexagon in Fig.2.2), put them at atom positions (i.e. black circle in Fig.2.2) and term it as the highest order process zone element.

(3) It is found that the whole two-dimensional or three-dimensional space cannot be covered by the scaled VDP. Therefore, corresponding different shape of elements are used to fill in the gaps among scaled VDPs, such as green quadrilateral element representing the 1st-order process zone and yellow triangular element representing 0th-order process zone in Fig.2.2.

This process is termed as dual lattice process zone tessellation. After completing the dual lattice process zone tessellation of a unit crystal lattice, we have a corresponding unit cell of dual lattice process zone model as shown in Fig.2.1(b).

Actually, the lattice tessellation is not a new notion. There are huge amounts of literature in the past mathematical study. But here we prefer to use a computational method rather than from mathematical view to describe the geometric topology of lattice tessellation. We will propose our own description method of three-dimensional defects based on the algebraic and differential topology in next section.

2.3 Dual Lattice Tessellation on BCC Crystals

In this section, we are applying the dual lattice process zone tessellation on three-dimensional crystalline solids and prove that the three-dimensional space occupied by Body-centered
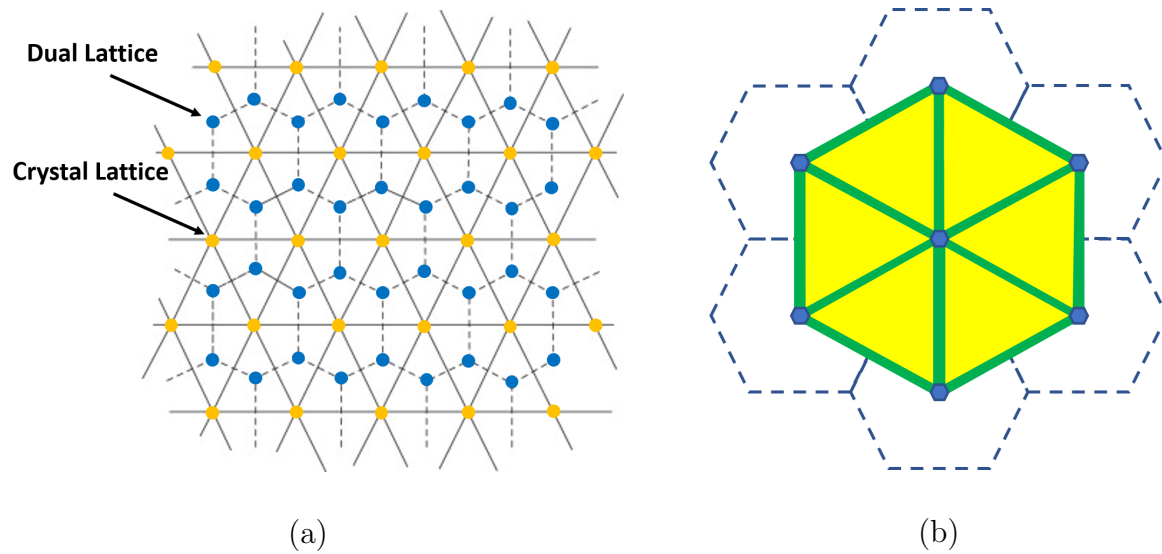
Figure 2.1: (a) Illustrations of crystal lattice and dual lattice; (b) unit cell of dual lattice process zone model.
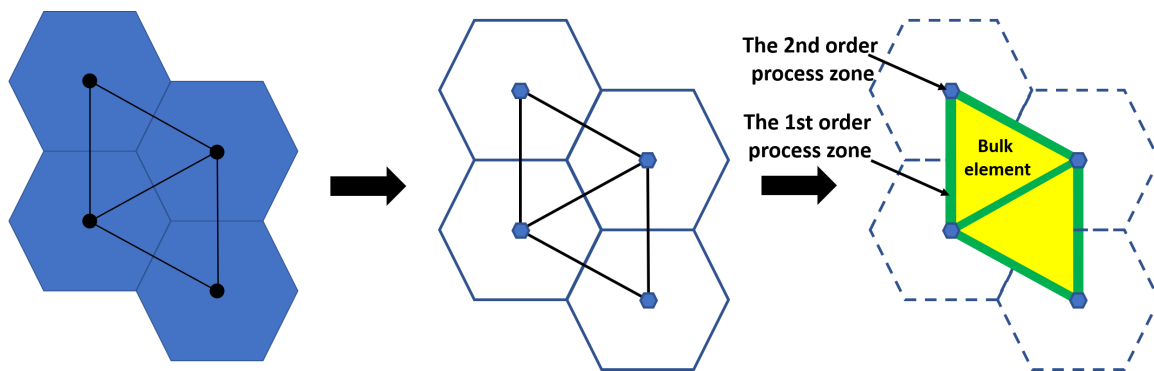
Figure 2.2: The illustrative process zone tessellation: (1) Yellow region: the 0th-order process zone; (2) Green region: the 1st-order process zone, and (3) Blue region: the 2nd-order process zone.

(a) (b) (c)
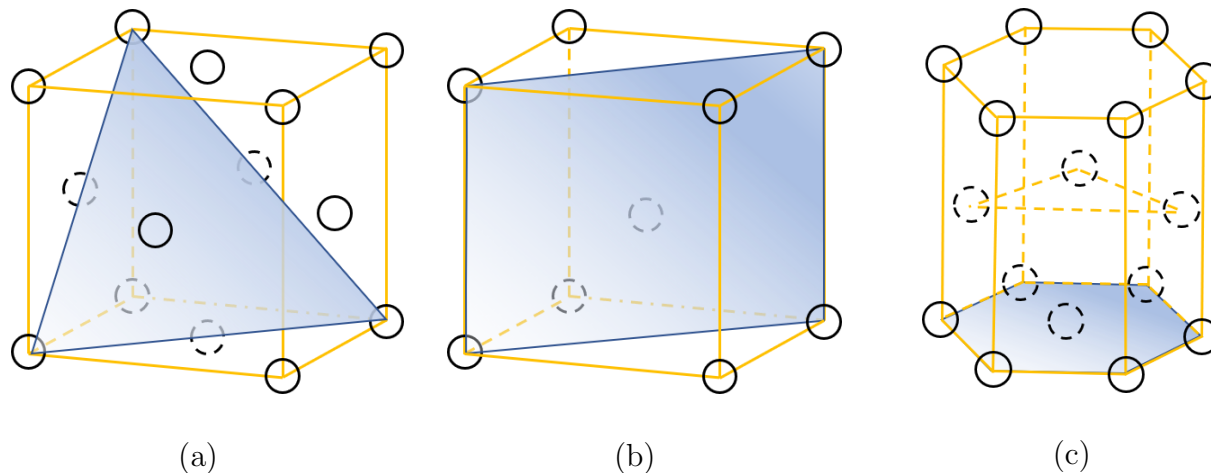
Figure 2.3: Slip planes: (a) {111} slip plane in Face-centered Cubic crystal; (b) {110} slip plane in Body-centered Cubic crystal; (c) {0001} slip plane in Hexagonal Closed-packed crystal.

Cubic (BCC) crystal can be completely partitioned by the method of dual lattice process zone tessellation.

2.3.1 Dual-lattice process zone tessellation on BCC Crystals

Linking two adjacent atoms together and the corresponding line segment will form so that the line segment will be equally divided into two segments through a plane normally placed at the midpoint of the line segment, we can have the corresponding Voronoi-Dirichelt Polyhedron (VDP) for the specific crystal lattice structure. The key point is how to choose the representative atoms in crystal lattice because considering different number of atom shells as representative atoms in crystal lattice will have different VDPs and accordingly to have different dual-lattice process zone tessellation. For BCC crystals, the first two nearest atom shells are chosen as the representative atoms including 8 atoms in the first shell and 6 atoms in the second shell. The reason why first two atom shells are chosen is BCC crystal does NOT have the most close-packed plane. It is different from FCC crystal whose most close-packed plane is {111}. The secondary most-packed plane of BCC crystal is {110} (see Fig.2.3). Therefore, we have the corresponding VDP that is a truncated octahedron, which is referred as the unit cell of dual lattice tessellation in BCC crystal structure as shown in Fig.2.4(b). Different from dual-lattice tessellation, the BCC unit cell in crystal lattice is a rhombic dodecahedron as shown in Fig.2.4(a).

Now we can give detailed illustration on construction of a three-dimensional BCC dual-lattice process zone tessellation. First of all, a special VDP constructed is based on the selective representative atoms. The combination of VDPs and other lower order polyhedra elements will cover the whole crystal lattice space. It is valid for dual-lattice and super dual-lattice
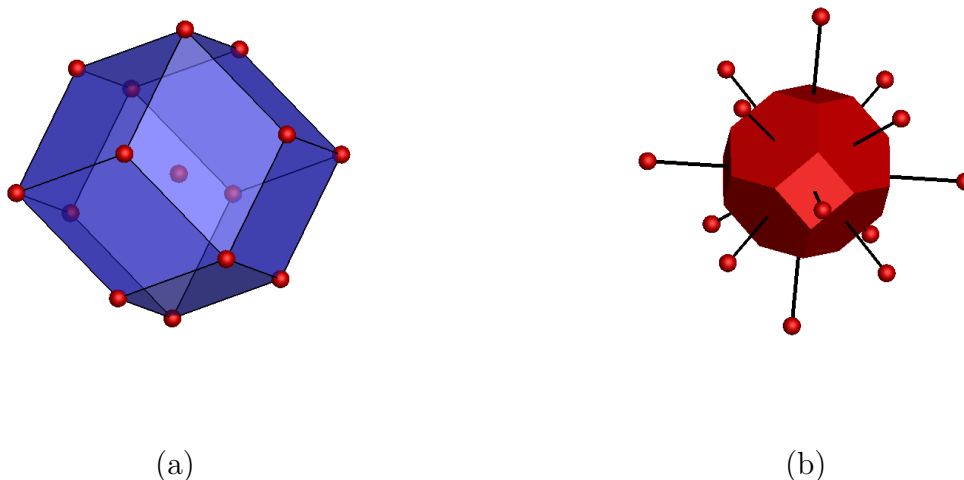
Figure 2.4: (a) unit cell of BCC crystal lattice; (b) unit cell of BCC dual-lattice.

when super VDP is used. And then the VDP is labelled as the highest order process zone element in the rest of the dissertation.

The worthy noting is the difference between Voronoi-Dirichlet partition and the dual-lattice process zone tessellation. The dual-lattice process zone tessellation is the result of scaling the Voronoi-Dirichlet Polyhedron down and connecting the nearby VDPs by using lower order process zone elements like bulk element(0th-order process zone element), wedge element(1st-order process zone element) and prism element(2nd-order process zone element). Therefore, if it is Voronoi-Dirichlet partition, none of lower order process zones exists since they degenerate, in other words, they are not three-dimensional objects any more. To avoid the unexpected degeneration, the gaps among VDPs by scaling them down becomes necessary. Based on the specialties of truncated octahedron as the VDP of BCC crystal structure, 14 facets of the highest order process zone element (truncated octahedron element) denote 14 prism elements needed to fill in the gaps of facet-to-facet of truncated octahedron elements (Fig.2.5) and 36 edges of truncated octahedron element denote 36 wedge elements needed to fill in the gaps of edge-to-edge of truncated octahedron elements (see Fig.2.6(a)-(f)), and 24 vertices of truncated octahedron denote 24 bulk elements needed to fill in the gaps of vertex-to-vertex of truncated octahedron elements (see Fig.2.6(g)-(l)).

Therefore, we can summarize that for a dual lattice tessellation unit cell of Body-centered Cubic crystal, firstly there are 15 truncated octahedron elements (one locates at centre of the dual lattice structure and other 14 represent the nearest two atom shells locations); secondly a truncated octahedron element has totally 14 facets including 8 hexagons and 6 squares therefore corresponding 3D prism elements are needed; thirdly 36 wedge elements (see Fig.2.6(a)-(f)) and 24 bulk elements (see Fig.2.6(g)-(l)) will cover the remained void space.

(a)   (b)
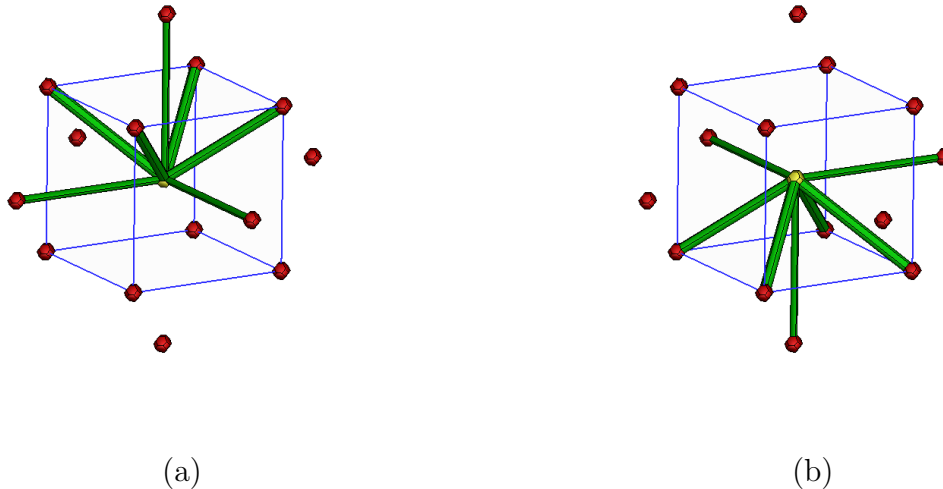
Figure 2.5: (a) upper seven prism elements (second-order process zones); (b) lower seven prism elements.

The vertex-to-vertex between truncated octahedron element and prism element, the edge-to-edge between truncated octahedron element and wedge element, the facet-to-facet between truncated octahedron element and prism element are shown in Fig.2.7.

2.3.2   Discrete exterior calculus on BCC Crystals

2.3.2.1   Polytopal complexes of a crystal lattice

In this work, we adopt the notation and nomenclature of algebraic topology and discrete exterior calculus e.g. [48][49], to describe dual-lattice process zones. It may be noted that Ariza and Ortiz [36] also applied algebraic topology and exterior calculus to describe 3D crystal lattice and to study dislocation statics. They used some elements with simple geometric shapes to describe the structure of crystal lattice, such as atoms and atom bonds. Those objects including points, lines, faces and volumes are respectively represented as simplex p-cells, where p is the dimension of a cell. By using the concept as well as notation of p-cell, one may be able to define geometric objects arising from the mechanics of lattices, i.e. displacement field, dislocation density distribution, etc.

Since the present work is about dislocation patterns dynamics, we cannot use simplicial complex p-cell to describe discrete dislocation pattern units. However, the theory of algebraic topology and exterior differential calculus can still be applied to describe dislocation pattern dynamics in terms of p-cell of CW complexes. Based on [34], we cited following definitions and operators:
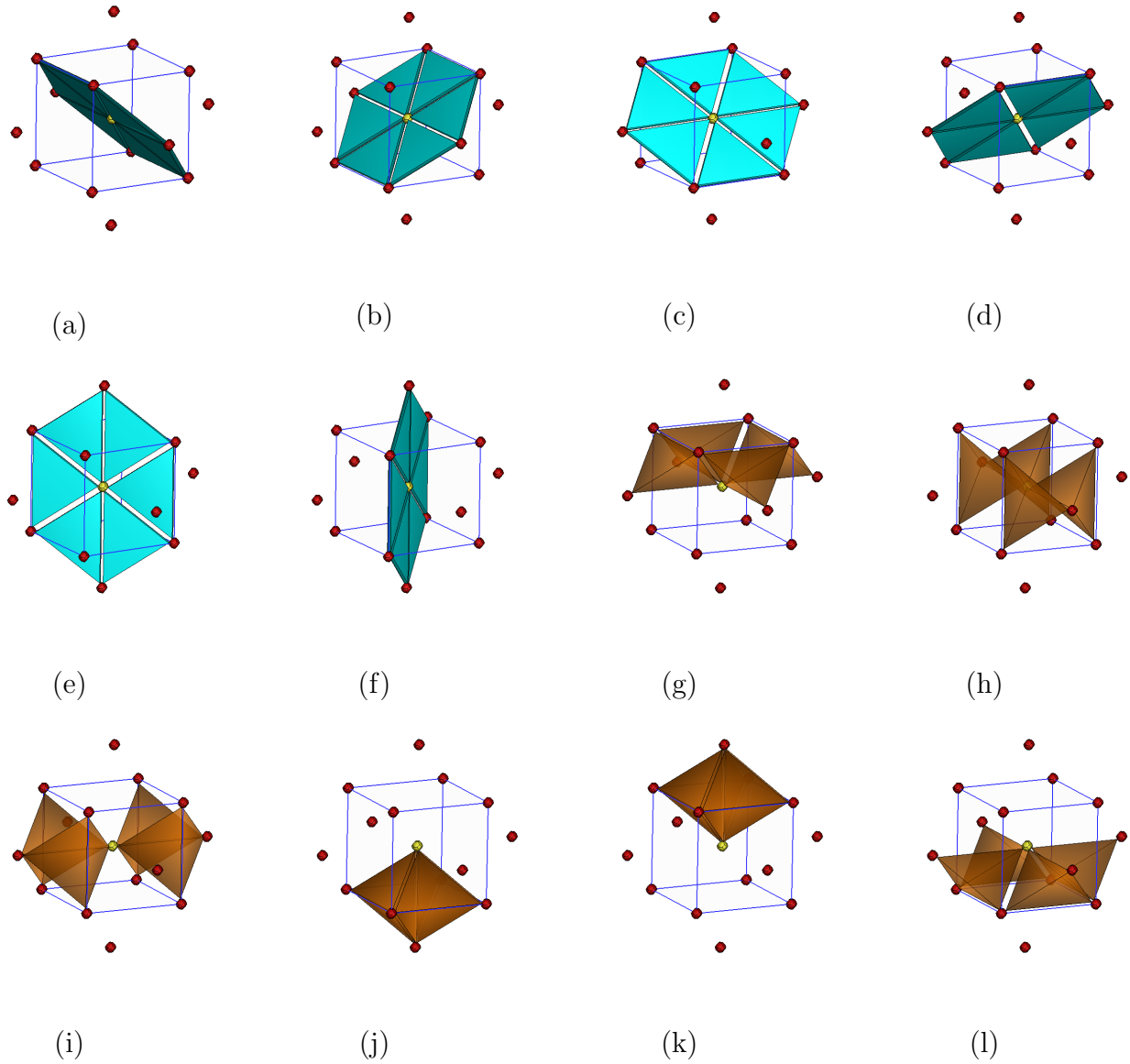
Figure 2.6: Components of BCC dual lattice tessellation unit cell: (a) six wedge element sets and each set has six wedge elements ((a)-(f)); and six bulk element sets and each set has four bulk elements ((g)-(l)).

(a) (b) (c)
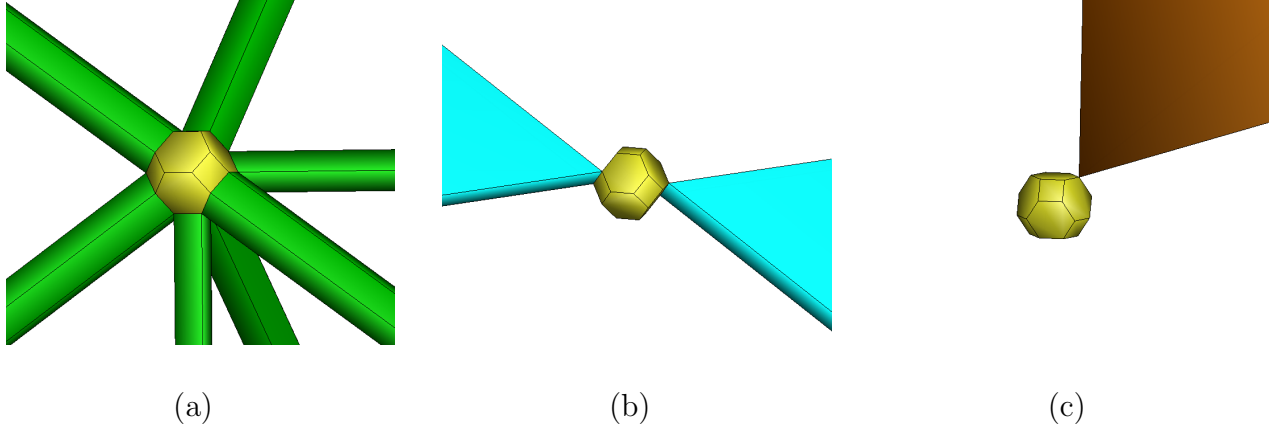
Figure 2.7: Detailed connections of 3rd-order process zone in BCC crystals with: (a) 2nd-order process zone (prism element); (b) 1st-order process zone (wedge element); (c) 0th-order process zone (bulk element).

Definition 2.1. The *k-simplex* is defined as a convex hull of $k+1$ vertices

$$\sigma^k = \left\{ \boldsymbol{x} \in \mathbb{R}^n | \boldsymbol{x} = \sum_{i=0}^{k} \mu^i v_i, \text{ with } \mu^i \geqslant 0 \text{ and } \sum_{i=0}^{k} \mu^i = 1 \right\} \tag{2.1}$$

in which, a set of $k+1$ linearly independent points, $\{v_0, v_1, \cdots, v_k\} \in \mathbb{R}^n, n > k$, are termed as vertices. The face is defined as the sub-element of a simplex σ^k. For example, a tetrahedron consists of four triangle surfaces and it is denoted that a triangle is the sub-element of a tetrahedron. The tetrahedron is a three-dimensional object so that it can be defined as 3-simplex and correspondingly the triangle is defined as 2-simplex. Besides, from the perspective of simplicial complex theory, "facet" and "face" are two different concepts. "facet" denotes as the sub-element that is only one level lower than simplex σ^k, for example, a triangle is a facet of a tetrahedron since a triangle is 2-simplex and a tetrahedron is 3-simplex. "face" denotes as all sub-elements of a simplex σ^k, for example, points, line segments and triangles are all included as faces of a tetrahedron because all those sub-elements are combined to form a tetrahedron. Therefore, it is concluded that "facet" is belong to "face". As shown in Fig.2.8([7]), 0-simplex is a point, 1-simplex is a line segment, 2-simplex is triangle and 3-simplex is tetrahedron. The detailed faces numbers are shown in table.2.1.

In current dissertation, it is very natural to generalize the concept of *Simplicial Complex* to *Polytopal Complex* since any a polytopal complex can be triangulated as several simplicial complex. In other words, the polytopal complex contains the simplicial complex.
In the following, two important topology operators are defined [34].

Figure 2.8: Illustrative example of simplexes([7])

Table 2.1: The number of faces in simplexes

Name	0-faces (vertices)	1-faces (edges)	2-faces (surfaces)	3-faces (volumes)
0-simplex (point)	1	N.A.	N.A.	N.A.
1-simplex (line segment)	2	1	N.A.	N.A.
2-simplex (triangle)	3	3	1	N.A.
3-simplex (volume)	4	6	4	1

Definition 2.2. The boundary operator for k-simplex is defined as:

$$\partial_k \sigma^k = \partial_k([v_0, v_1, \cdots, v_k]) = \sum_{i=0}^{k}(-1)^i [v_0, \cdots, \hat{v}_i, \cdots, v_k] \tag{2.2}$$

in which, $\sigma^k = [v_0, \cdots, v_k]$ is a k-simplex, and $[v_0, \cdots, \hat{v}_i, \cdots, v_k]$ is a corresponding face of σ^k.

Accordingly, such a boundary of the σ^k is

$$\partial_k \sigma^k = \sum_{\sigma^{k-1} \prec \sigma^k} \pm \sigma^{k-1} \tag{2.3}$$

in which the $+$ or $-$ is determined by consistency of orientations of σ^{k-1} and σ^k.

Furthermore, the coboundary of a simplex σ^k is given:

$$\delta^k \sigma^k = \sum_{\sigma^{k+1} \succ \sigma^k} \pm \sigma^{k+1} \tag{2.4}$$

in which the $+$ or $-$ is determined by consistency of orientations of σ^k and σ^{k+1}.

2.3.2.2 Discrete crystal defect model for BCC crystals

Since two main algebraic topology operators are introduced, a new super dual-lattice tessellation mesh for BCC crystals is proposed and it is used in local-to-global nodes numbering mapping of a multiscale process zone model.

A super dual-lattice tessellation for a Body-centered Cubic (BCC) crystal lattice will be discussed in the following. The first step is to introduce lattice basis vectors in BCC crystal lattice as shown in Fig.2.9(a),

$$a_1 = \left(-\frac{a}{2}, \frac{a}{2}, \frac{a}{2}\right), \quad a_2 = \left(\frac{a}{2}, -\frac{a}{2}, \frac{a}{2}\right), \text{ and } a_3 = \left(\frac{a}{2}, \frac{a}{2}, -\frac{a}{2}\right).$$

Secondly, to create a "super" lattice (see Fig.2.9(c)) whose size is proportional to the size of a regular crystal lattice, a coefficient β_1 is introduced to change basis vectors,

$$b_i = \beta_1 a_i, \quad i = 1, 2, 3 \quad \beta_1 > 1$$

Thirdly, the dual lattice of Body-centered Cubic crystal is chosen as a frame of super lattice sites and accordingly the coordinate of each vertex is,

$$\varepsilon_1 = a\left(\frac{1}{2}, 0, 1\right), \quad \varepsilon_2 = a\left(0, \frac{1}{2}, 1\right), \quad \varepsilon_3 = a\left(-\frac{1}{2}, 0, 1\right), \quad \varepsilon_4 = a\left(1, 0, \frac{1}{2}\right), \quad \varepsilon_5 = a\left(0, 1, \frac{1}{2}\right)$$

$$\varepsilon_6 = a\left(-1, 0, \frac{1}{2}\right), \quad \varepsilon_7 = a\left(0, -1, \frac{1}{2}\right), \cdots, \varepsilon_{23} = a\left(-\frac{1}{2}, 0, -1\right), \quad \varepsilon_{24} = a\left(0, -\frac{1}{2}, -1\right)$$

and the scaled Voronoi-Dirichlet Polyhedron (VDP) cell of BCC crystals (see Fig.2.9(b)) is placed at each super lattice site. The scalability of VDP cell is described as $r_i = \beta_2 \varepsilon_i, \quad \beta_2 > 0$. The location of each vertex in the super lattice can be labelled as $l \pm \epsilon_i, i = 1, 2, \cdots, 7$, as shown in Fig.2.9(c) in which

$$\epsilon_1 = (-1, 1, 1), \quad \epsilon_2 = (1, -1, 1), \quad \epsilon_3 = (1, 1, -1), \quad \epsilon_4 = (1, 1, 1)$$
$$\epsilon_5 = (1, 0, 0), \quad \epsilon_6 = (0, 1, 0), \quad \epsilon_7 = (0, 0, 1)$$

Summarily, the coordinate of each vertex in BCC super dual lattice mesh is denoted as

$$x(l) = l^j \boldsymbol{b}, \text{ and } x(l, \epsilon_i) = l^j \boldsymbol{b} + r_i, \qquad i = 1, 2, \cdots, 24$$

in which, l^j denotes $l \pm \epsilon_j$ and $\boldsymbol{b} = (b_1, b_2, b_3)$.

Generally speaking, each scaled VDP cell will locate at each lattice site of Body-centered Cubic crystal super lattice. The gaps or remained spaces among them can be filled by other 3D polytopal complexes without overlapping. The way of combining different polytopal complexes is through surface-to-surface (prism cell and truncated octahedron cell), edge-to-edge (wedge cell and truncated octahedron cell) and vertex-to-vertex (bulk cell and truncated octahedron cell) connection.
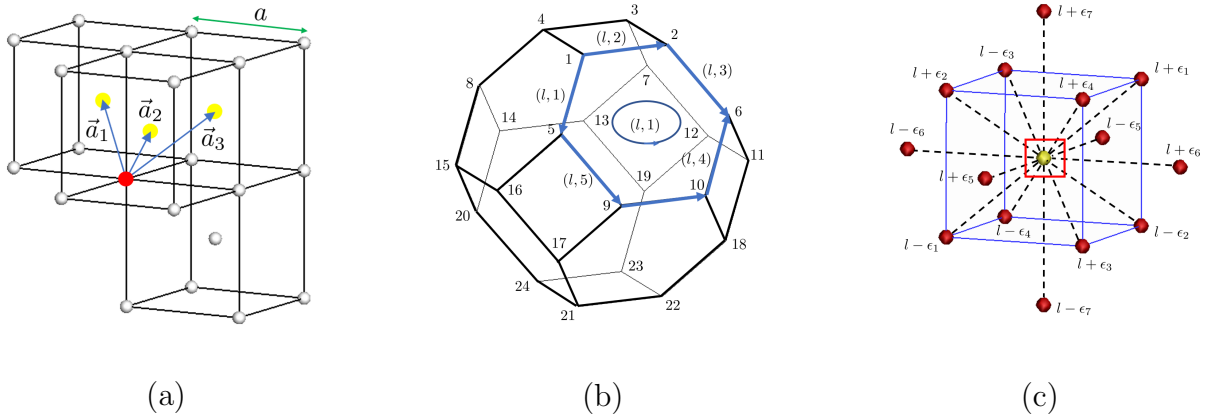
Figure 2.9: Exterior calculus on super dual-lattice complex: (a) Body-centered Cubic crystal lattice basis; (b) the scaled Voronoi-Dirichlet Polyhedral (truncated octahedron) cell at lattice site l; (c) neighboring scaled VDPs position numbering in a super dual-lattice tessellation unit cell.

To make the statements consistent in the dissertation, a unified symbol to describe the relations among different 3D polytopal complexes is necessary. Therefore, the symbol $\tau_j^i(l(\ell), m)$ is introduced. i represents the dimension of the polytopal complex discussed, i.e. $i = 0$ denotes a point, $i = 1$ denotes a line segment, $i = 2$ denotes a surface and $i = 3$ denotes a volume. j represents type ID of polytopal complexes in BCC super lattice tessellation model or order of process zone in Chapter 2, i.e. $j = 0$ indicates bulk cell (0th-order process zone), $j = 1$ indicates wedge cell (1st-order process zone), $j = 2$ indicates prism cell (2nd-order process zone) and $j = 3$ truncated octahedron cell (3rd-order process zone).

l represents the central lattice site of the super dual lattice and other 14 lattice sites in the super dual lattice can be labelled as $l \pm \epsilon_1$, $l \pm \epsilon_2, \cdots l \pm \epsilon_7$. ℓ represents the numbering of the polytopal complex j discussed and in different polytopal complex the range of ℓ is different. For example, for prism cells there are totally 14 prism cells needed in a BCC super dual lattice tessellation unit cell so that $\ell = 1, 2, \cdots, 14$; for wedge cells there are totally 36 wedge cells needed in a BCC super dual lattice tessellation unit cell so that $\ell = 1, 2, \cdots, 36$; etc. m represents numbering of the sub-polytopal complex i discussed and in different sub-polytopal complex the range of m is different. For example, for a truncated octahedron cell, there are 14 surfaces ($i = 2$) so that $m = 1, 2, \cdots, 14$, there are 36 edges ($i = 1$) so that $m = 1, 2, \cdots, 36$ and there are 24 vertices ($i = 0$) so that $m = 1, 2, \cdots, 24$.

In the next we shall take $\tau_2^1(l(5), 1)$ as an example to illustrate the application of those labeling and those operators. As we know that in the label $\tau_j^i(l(\ell), m)$, i represents the dimension of sub-polytopal cell and j represents the which type of polytopal cell. Therefore, we have superscript $i = 1$ representing edge element, subscript j representing prism element, $l(5)$ representing NO.5 prism element and 1 represents the NO.1 edge in NO.5 prism element as shown in Fig. 2.13. This labeling process is important in Finite Element Method (FEM)
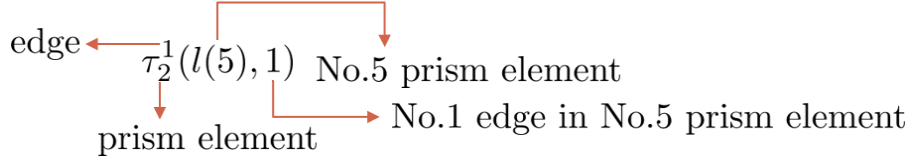
Figure 2.10: Polytopal element labeling convention

formulation and implementation because we need to use the exterior calculus symbol to construct the connectivity array of FEM nodes that maps the local indices into global indices. By using boundary operator of exterior calculus in **Definition 2.2**, we can represent lines and faces. For example, for central scaled truncated octahedron $\tau_3^3(l)$, we have

$$\partial\tau_3^1(l,1) = \tau_3^0(l,5) - \tau_3^0(l,1) \tag{2.5}$$

$$\partial\tau_3^2(l,1) = \tau_3^1(l,1) + \tau_3^1(l,5) + \tau_3^1(l,6) + \tau_3^1(l,4) - \tau_3^1(l,2) - \tau_3^1(l,3) \tag{2.6}$$

and

$$\partial\tau_3^3(l,1) = \tau_3^2(l,1) + \tau_3^2(l,2) + \tau_3^2(l,3) + \tau_3^2(l,4) + \tau_3^2(l,5) + \tau_3^2(l,6)$$
$$+ \tau_3^2(l,7) - \tau_3^2(l,8) - \tau_3^2(l,9) - \tau_3^2(l,10) \tag{2.7}$$
$$- \tau_3^2(l,11) - \tau_3^2(l,12) - \tau_3^2(l,13) - \tau_3^2(l,14)$$

which are shown in Fig.2.11.
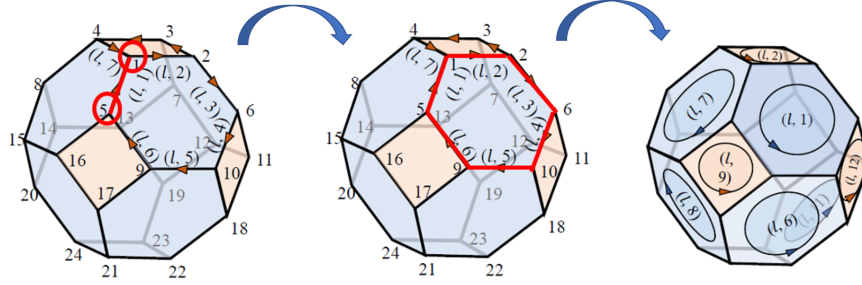
Figure 2.11: Boundary operator illustration:from vertex to edge, from edge to surface, from surface to volume

Similarly, we can use co-boundary operator δ to define the relations among different types of elements. For example, for the central scaled truncated octahedron $\tau_3^3(l)$, we have

$$\delta\tau_3^0(l,1) = \tau_3^1(l,7) - \tau_3^1(l,1) - \tau_3^1(l,2) - \tau_2^1(l(7),1) - \tau_2^1(l(3),2) - \tau_2^1(l(14),3) \tag{2.8}$$

$$\delta\tau_3^1(l,1) = \tau_3^2(l,1) - \tau_3^2(l,7) + \tau_2^2(l(7),1) - \tau_2^2(l(3),2) \tag{2.9}$$

$$\delta\tau_3^2(l,1) = \tau_3^3(l) - \tau_2^3(l,7) \tag{2.10}$$

which established the links from vertex to edge, edge to surface and surface to volumes as shown in Fig.2.12.
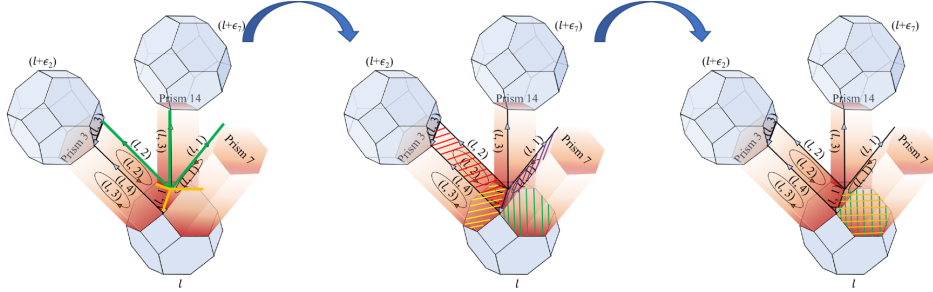
Figure 2.12: Co-boundary operator illustration: from edge to vertex, from surface to edge, from volume to surface

Furthermore, we can also apply the cell complex notation defined above to represent other types of elements. For example, the prism element $\tau_2^3(l, m), m = 1, 2, \cdots, 14$, (Fig.2.13(a)). We write the exterior representation by using boundary operator as shown in Fig.2.13(b),

$$\partial \tau_2^1(l(5), 1) = -\tau_3^0(l - \epsilon_3, 9) + \tau_3^0(l, 4) \tag{2.11}$$
$$\partial \tau_2^1(l(5), 2) = -\tau_3^0(l - \epsilon_3, 10) + \tau_3^0(l, 3) \tag{2.12}$$

in which, $\tau_3^0(l - \epsilon_i, j)$ denotes it is the j-th vertex $j = 1, 2, \cdots, 24$ of on the $l + \epsilon_i, i = 1, 2, \cdots, 7$ polytopal cell. Also we have (shown in Fig.2.13(c)-(d))

$$\partial \tau_2^2(l(5), 1) = \tau_2^1(l(5), 1) - \tau_2^1(l(5), 2) + \tau_3^1(l, 13) - \tau_3^1(l - \epsilon_3, 5) \tag{2.13}$$
$$\partial \tau_2^3(l, 5) = \tau_2^2(l(5), 1) - \tau_2^2(l(5), 2) + \tau_2^2(l(5), 3) + \tau_2^2(l(5), 4) \tag{2.14}$$
$$- \tau_2^2(l(5), 5) - \tau_2^2(l(5), 6) - \tau_3^2(l, 3) - \tau_3^2(l - \epsilon_3, 6)$$

The wedge complex cell (1st-order process zone), $\tau_1^3(l, m), m = 1, 2, \cdots, 36$, (see Fig.2.14(a)) is discussed here. From the perspective of geometric shape, a wedge complex cell with thin thickness is similar to slip plane in crystal plasticity theory. The geometry of the wedge complex cell can be described by topology boundary operator. For example, from vertex to edge (as shown in Fig.2.14(b))

$$\partial \tau_1^1(l(1), 1) = \tau_3^0(l - \epsilon_3, 9) - \tau_3^0(l + \epsilon_2, 12) \tag{2.15}$$
$$\partial \tau_1^1(l(1), 2) = -\tau_3^0(l - \epsilon_3, 17) + \tau_3^0(l + \epsilon_2, 19) \tag{2.16}$$

And from edge to surface, surface to volume (as shown in Fig.2.14(c)-(d))

$$\partial \tau_1^2(l(1), 3) = \tau_1^1(l(1), 1) - \tau_3^1(l - \epsilon_3, 24) + \tau_1^1(l(1), 2) + \tau_3^1(l + \epsilon_2, 22) \tag{2.17}$$
$$\partial \tau_1^3(l, 1) = -\tau_2^2(l(5), 1) - \tau_1^2(l(1), 1) + \tau_2^2(l(3), 1) + \tau_1^2(l(1), 2) + \tau_1^2(l(1), 3) \tag{2.18}$$

(a)

(b)

(c)

(d)
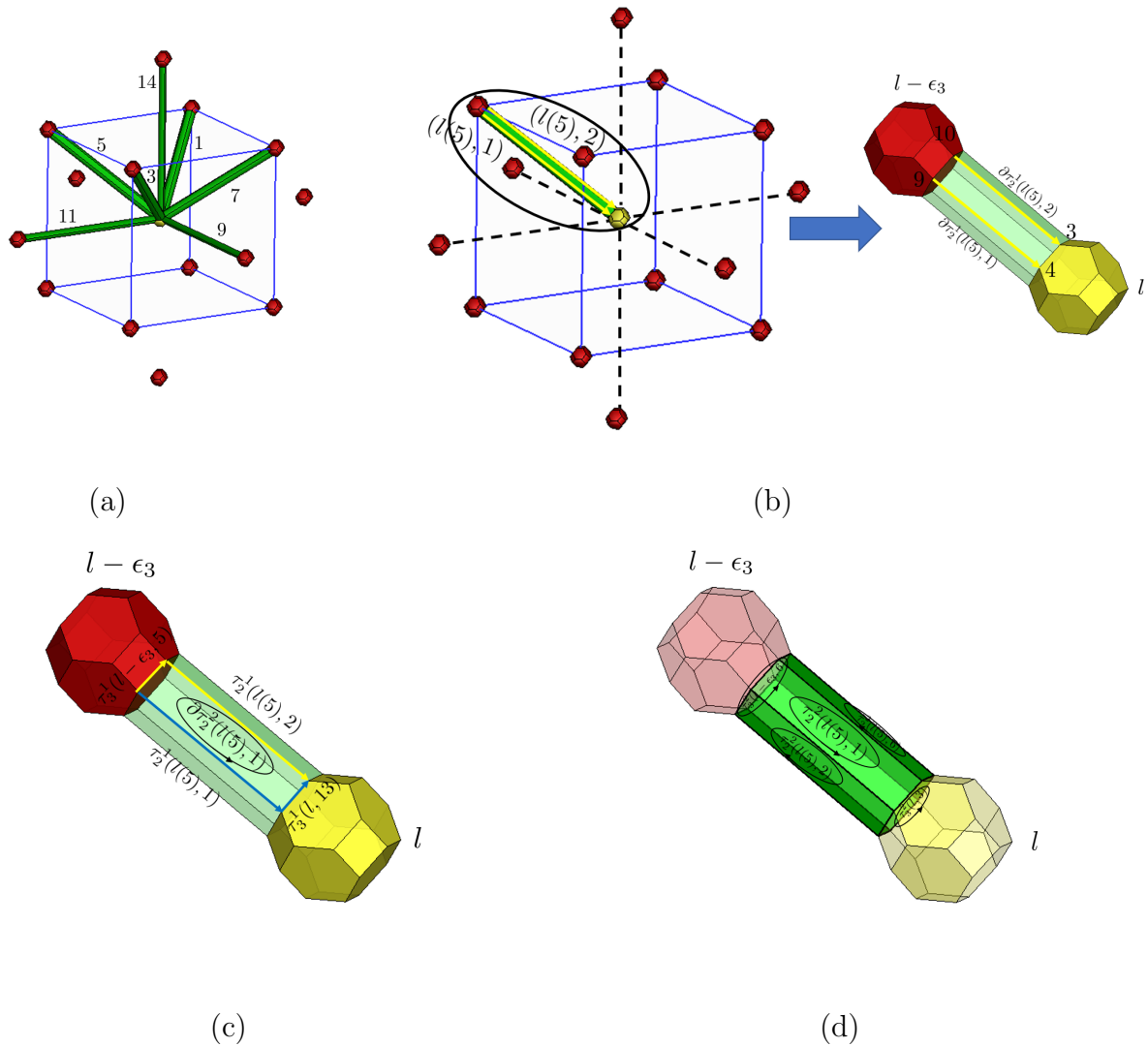
Figure 2.13: Boundary operator on prism element: (a) prism cells (2nd-order process zone);
(b) from vertex to edge; (c) from edge to surface; (d) from surface to volume.

(a)   (b)

(c)   (d)
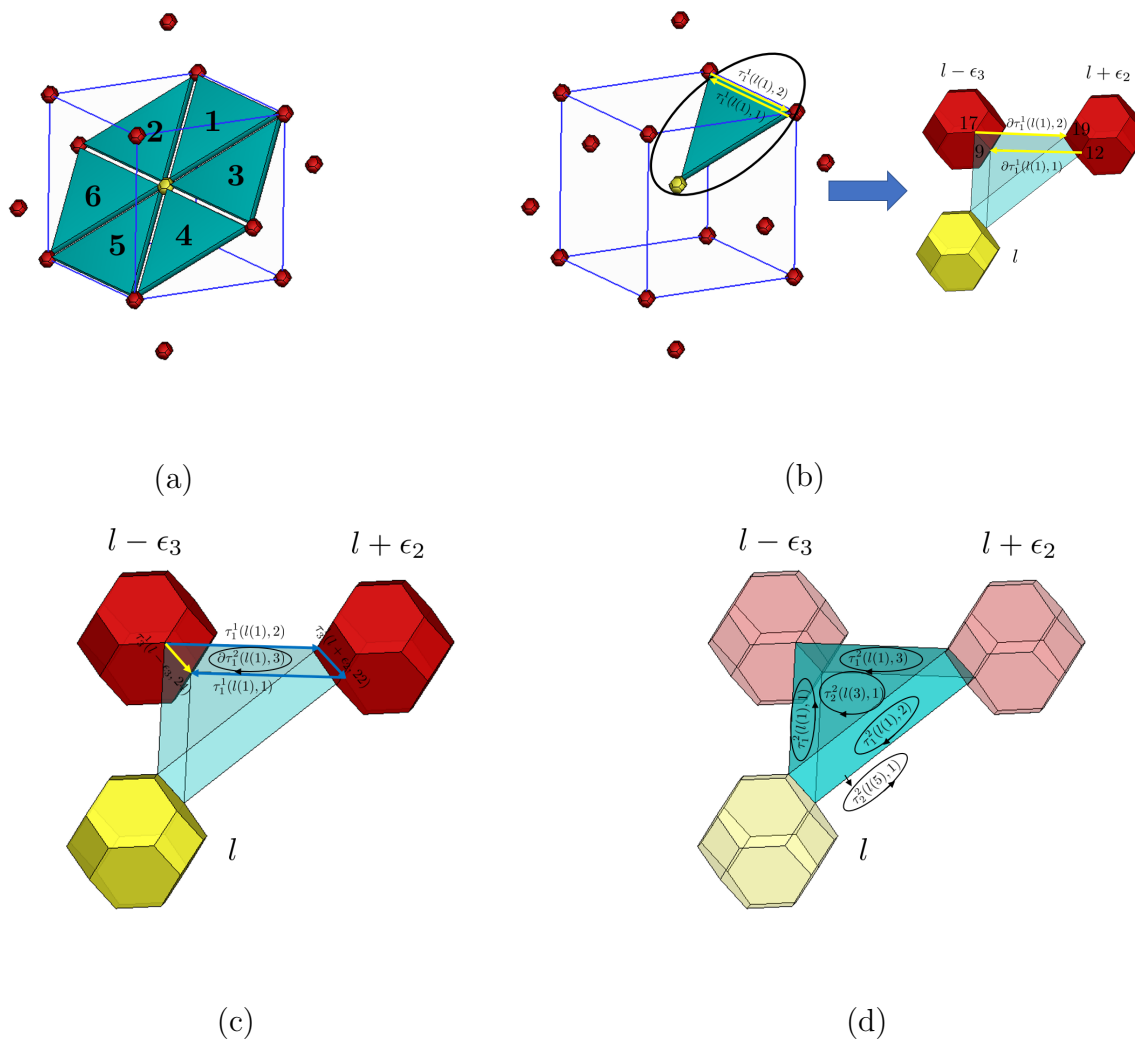
Figure 2.14: Boundary operator on wedge element: (a) 1st-order process zone (wedge) elements; (b) from vertex to edge; (c) from edge to surface; (d) from surface to volume.

The bulk complex cell is discussed. Different from other polytopal complexes, the bulk complex cell is a tetrahedron, which is a simplicial complex. In each truncated octahedron complex cell, 24 vertices correspond to 24 bulk complex cells (0th-order process zone), i.e.$\tau_0^3(l, m), m = 1, 2, \cdots, 24$ (see Fig.2.15(a)). The geometry of a bulk complex cell is described by topology boundary operator. For example, from vertex to edge (as shown in Fig.2.15(b)),

$$\partial \tau_0^1(l(1), 1) = \tau_3^0(l + \epsilon_2, 9) - \tau_3^0(l - \epsilon_6, 10) \tag{2.19}$$

$$\partial \tau_0^1(l(1), 2) = \tau_3^0(l - \epsilon_3, 5) - \tau_3^0(l + \epsilon_2, 9) \tag{2.20}$$

And from edge to surface, from surface to volume (as shown in Fig.2.15(c)-(d)),

$$\partial \tau_0^2(l(1), 1) = \tau_0^1(l(1), 1) + \tau_0^1(l(1), 2) - \tau_0^1(l(1), 3) \tag{2.21}$$

$$\partial \tau_0^3(l, 1) = \tau_0^2(l(1), 1) + \tau_0^2(l(1), 2) - \tau_0^2(l(1), 3) - \tau_0^2(l(1), 4) \tag{2.22}$$

(a)

(b)

(c)

(d)
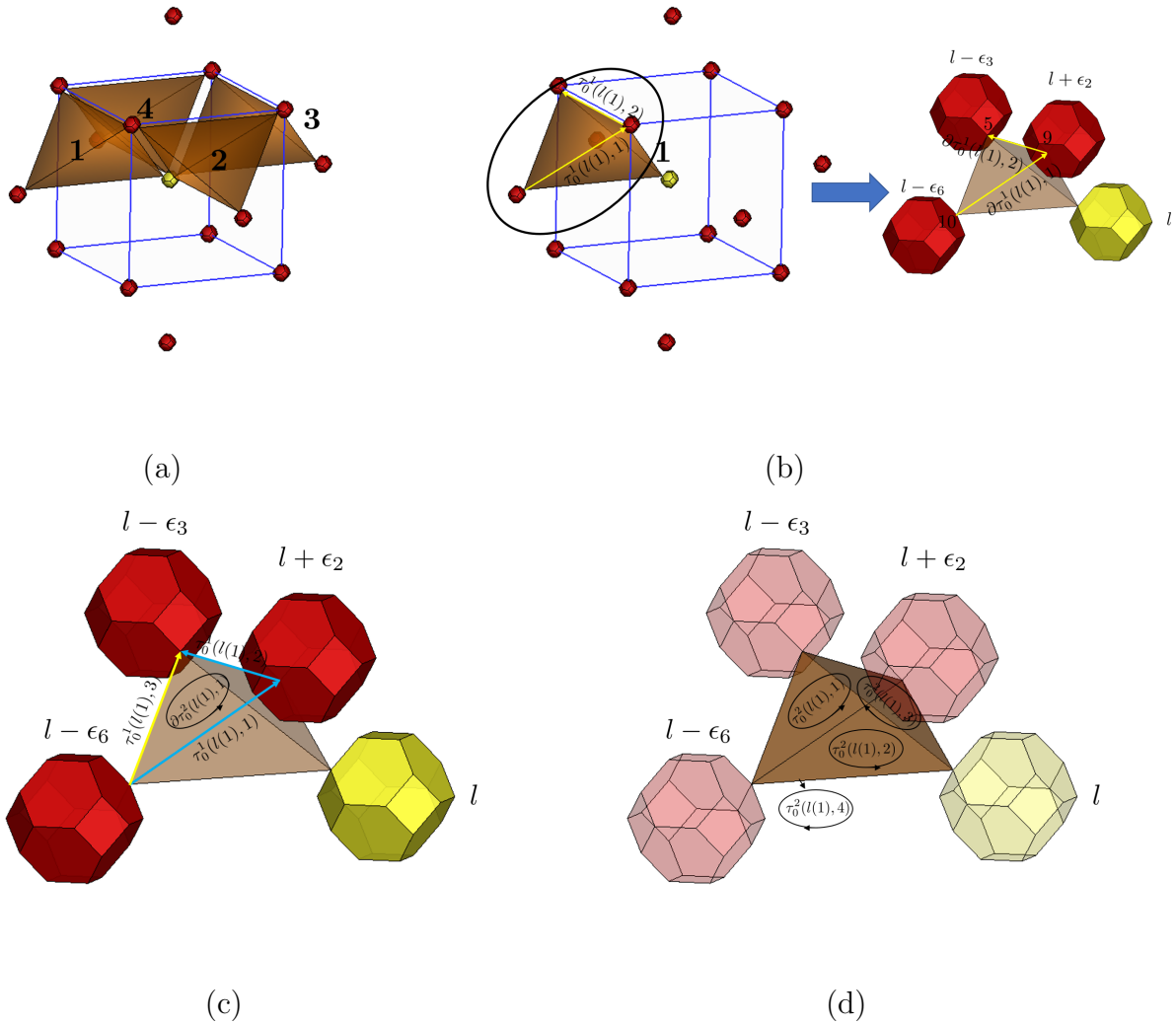
Figure 2.15: Boundary operator on bulk element: (a) 0th-order process zone (bulk) elements;
(b) from vertex to edge; (c) from edge to surface; (d) from surface to volume.

Chapter 3

Physics-based Topological Decomposition of Crystal Dislocation Pattern

When crystalline materials deform, statistical dislocations have the tendency to converge to some specific regions so that some regions are rich in dislocations while other regions are not. These two kinds of regions are sandwiched together. Nowadays, it is commonly believed that those dislocation-rich regions are responsible for almost crystal plasticity characteristics, for example, work hardening, strain location, etc. A new novel of the *Geometrically Compatible Dislocation Pattern (GCDP)* has been proposed [35][39], and in this Chapter it is further illustrated that the dual-lattice process zone tessellation mesh discussed in Chapter 2 has a very solid physics-informed link to original crystal lattice. Therefore, it is concluded that the new notion *GCDP* strongly dependent on original crystal lattice will dominate in plastic deformation of crystals at early stage.

3.1 Experimental Observation and Researches on Aggregated Dislocations

In discrete dislocation dynamics (DD), the smallest unit of dislocation dynamics is the dislocation segment [50]. Different from dislocation dynamics, the smallest unit of dislocation pattern dynamics is discrete dislocation pattern.

It is commonly believed that individual dislocation in deformed crystalline solids can be categorized as two classes: one is Statistically-stored Dislocations (SSD), another is Geometrically-necessary Dislocations (GND). The first quantitative computation method of Geometrically-necessary Dislocations (GND) has been proposed by Nye [51], in which a formulation combining effective plastic strain gradient and burgers vector to compute Geometrically-necessary Dislocation density is proposed. Later on, Ashby successfully introduce notion of GNDs into

flow stress in crystalline solids [52]. Based on these two pioneering's work, many scholars (e.g. [53] and [54]) have made contributions to link the GNDs to plastic strain gradients. For Statically-stored Dislocations (SSD), they evolve from stochastic process and randomly aggregate into a specific field in crystalline solids when plastic deformation proceeds [38][55]. The Statistically-stored Dislocations usually converge into such pattern that rich dislocations regions sandwiched with low dislocation regions. And the boundary between rich/low dislocations regions and corresponding networks play a significant role in dislocation patterns formation. The geometries of those dislocation boundary networks include walls, veins, labyrinth and bands. The related studies on such networks can date back to early 1990s: two clear notions of dislocation boundary networks were given as *geometrically necessary boundaries* and *incidental dislocation boundaries* by Kuhlman-Wilsdorf [37]. Arsenilis[38] found that not only Geometrically-necessary Dislocations existing within the *geometrically necessary dislocation boundary*, but also Statistically-stored Dislocations existing within it. To distinguish it from those dislocation boundaries only having GNDs, *geometrically allowable dislocation* has been proposed.

It is noteworthy that Nye tensor alone cannot accurately quantify dislocations within the dislocation patterns consisting of GNDs and SSDs. Therefore, a dislocation pattern model will be proposed to compensate the incompleteness.

To develop dislocation pattern model, we first need to know how is the dislocation pattern formed initially.[1] Based on the experimental findings (Fig.3.1), e.g. [56], the authors found that,······ *planar slip mode was found to be dominating in this low stacking fault energy (SFE) steel under the small strain amplitudes* ······ *The interaction of different slip systems forms junctions, which assist the formation of dislocation dipoles and later on trigger the formation of dislocation walls. These walls consist of primary faulted dipoles in their interior and pile-ups of dissociated dislocations of opposite signs on their two sides. It was found that the dislocations in the walls belong to two major, collinear slip systems.*

In [57], the same authors observed that *dislocation loops with opposite Burgers vectors are formed on the intersecting slip systems with a collinear relationship.* ······ *When dislocation from the two slip systems simultaneously reach the intersection lines, the screw parts with opposite Burgers vectors will be annihilated.* ······ *These edge dislocation segments on intersecting planes are connected by nodes which are junctions of zero Burgers vector.*

In [58], authors specifically discussed those dislocation dipole junctions: *The formation of persistent slip band (PSB) ladders depends on the width of extended dislocation and trap distance of dipole. When the actual capture distance d_{trap} is less than the critical capture distance $d_{critical}$, a group of relatively stable multiples are obtained from many dipole segments, followed by the formation of the veins and PSB-ladder structure.*

These and other experimental observations indicate that the formation of dislocation pattern has to be geometrically compatible. We believe that the geometric compatibleness of dislocation patterns is a determining factor for the early formation of dislocation microstructure or substructures, or the deformation structures. To illustrate this point, we slightly rephrase

---

[1]In the dissertation, we only consider the initial formation of dislocation patterns.

(a)

(b)

(c)

(d)
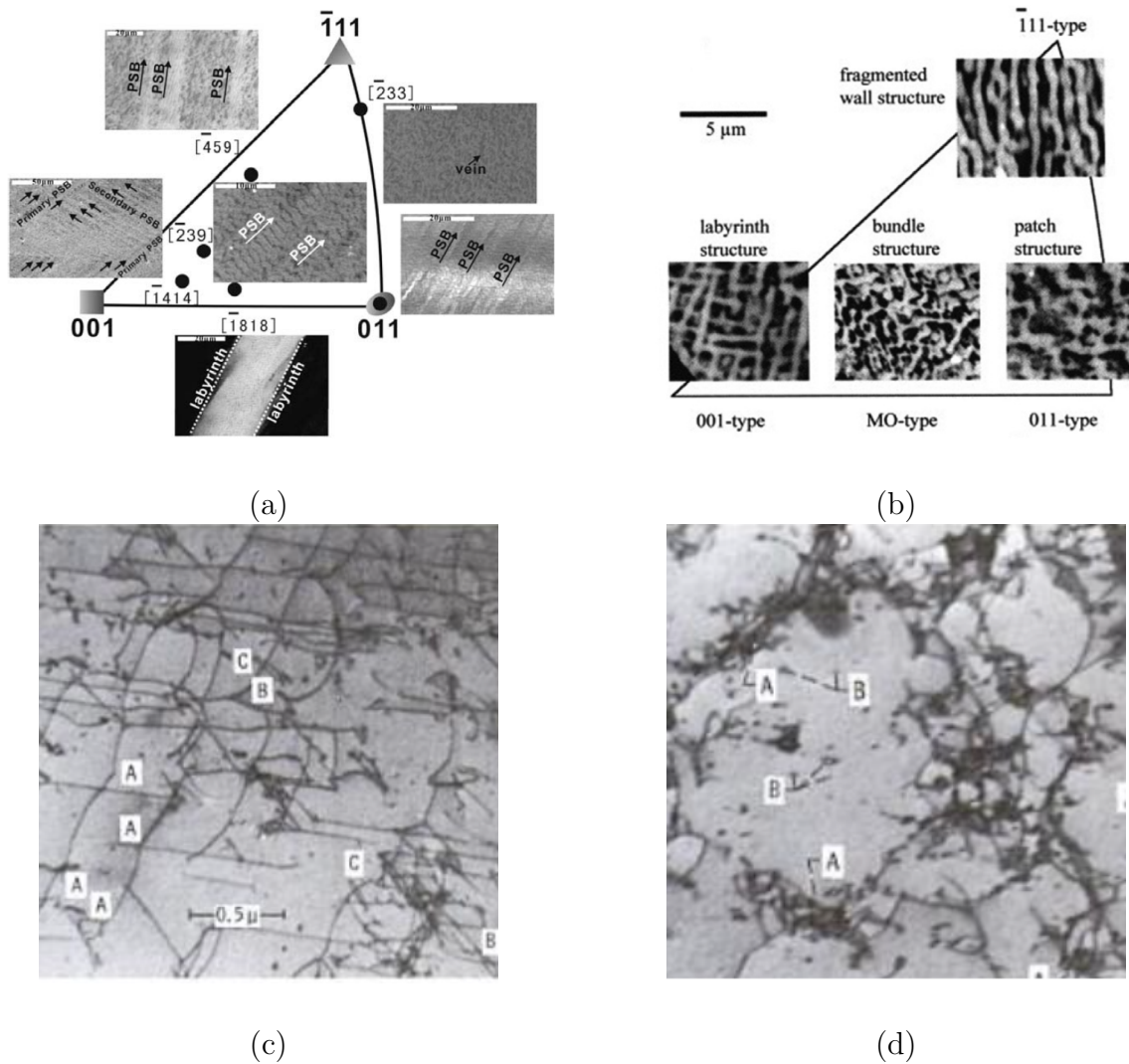
Figure 3.1: Dislocation pattern formation: (a) plasticity in Silver[8] (Reuse permission by
Elsevier: License Number 5063710958535); (b) plasticity in Nickel[9] (Reuse permission by
Elsevier: License Number 5063711405070); (c)-(d) plasticity in Tungsten (9% rhenium) at
1% and 2% strain[10].

the above experimental observations: At the very beginning stage of the dislocation multiplication, a statistical number of parallel slips have pre-existed in different slip systems along different atomic planes, and then a bulk-shaped junction (see Fig.3.2) will form at the intersection of slips. From the energetic perspective, retaining geometric compatibility with the local crystal structure in order to maintain deformation structure integrity is a necessity for a deformed or defected crystal, the so-called dislocation networks are formed. We call such network as *Geometrically Compatible Dislocation Pattern (GCDP)* (see Fig.3.2(c)).
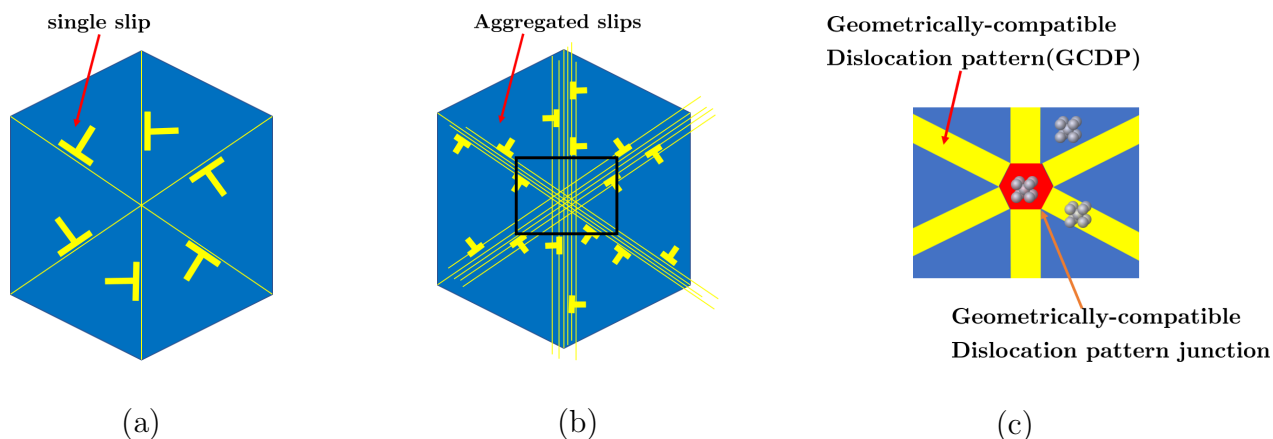
Figure 3.2: The 2D projection of geometrically-compatible dislocation pattern: (a) single dislocation of various slip systems; (b) a bulk-shaped intersection by slips convergence, and (c) a 2D projection of geometrically-compatible dislocation pattern.

3.2 Geometrically Compatible Dislocation Pattern on BCC Crystals

Now we want to extend the above Geometrically Compatible Dislocation Pattern arguments to three-dimensional BCC crystals. Since we know that Body-centered Cubic (BCC) crystal structure is not the close-packed structure, the most likely slip plane should be {110}, which is the secondary most packed plane. Based on the dislocation pattern structure in the {110} plane of BCC crystals as shown in Fig.3.3(a), we can recover its three-dimensional geometric structure as shown in Fig.3.3(b)-(c). It may be noted that Fig.3.3(c) is no longer a BCC lattice, and it is a super dual lattice of BCC crystal, and we may call it as the dual lattice process zone tessellation of BCC structure. We think it contains *all possible* three-dimensional dislocation microstructure and substructures at the early stage. During a actual loading event, for a specific BCC crystal, and under a given temperature, a particular dislocation substructure or deformation structure will appear naturally. Any of those possible dislocation microstructure is called the *Geometrically Compatible Dislocation Pattern*, because they partition the entire crystal space with a compatible mesh without overlaps,

holes and penetration. It should be noted that firstly the super dual lattice or dual lattice
process zone mesh contains all possible kinematically compatible dislocation patterns, and at
an actual load event there is only particular dislocation pattern will appear. This situation
is rather like the Cohesive Zone Model (CZM) Finite Element mesh, and thus why we coin
the name of *Dual Lattice Process Zone* mesh.

The process from 2D to 3D, we can find that 2D hexagonal or honeycomb element is actually
the projection of a polyhedron cell that has exactly the shape of the Wigner-Seitz cell of
BCC crystals, which is the truncated octahedron element as shown in Fig.3.3.

Therefore, to identify the generic dislocation pattern for BCC crystals or construct du-
al lattice process zone mesh, we can firstly start from constructing the Voronoi-Dirichlet
Polyhedron (VDP) cells at given representative atom positions based on the required reso-
lution, and the Voronoi-Dirichlet Polyhedron (VDP) cells that have the shape resemble to
the Wigner-Seitz cell of BCC crystals

(a)   (b)   (c)
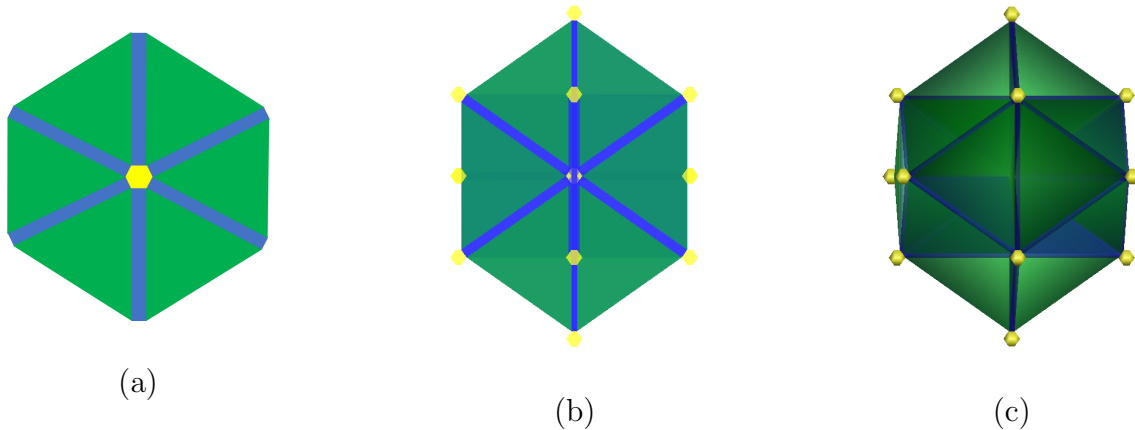
Figure 3.3: How to extend a BCC (110) plane dislocation pattern into a 3D dislocation
pattern network or dual lattice tessellation.

Remark 3.1. *The combination of these four different elements captures all kinematics pos-
sibilities of how a dislocation pattern can be found. As one may see from Fig.2.12 or Fig.2.13
that the prism elements will form dislocation pattern network that resembles dislocation lines
in a perfect BCC crystal. From Fig.2.6(a)-(f), one may find that all the triangle plate shape
elements can form all possible finite thickness slip "plates" that resemble the original slip
planes in BCC crystals. The only reason that the plate is no longer a plane is because that
we are dealing with the aggregated slip plane movement but not a single slip plane or disloca-
tion line. One can clearly see the geometric connection between super dual lattice mesh with
the original crystal structure, but they are not the same. In the original crystal lattice, the
defect can be only one dislocation, and by using the dual lattice process zone mesh, we can
deal with a set of aggregate dislocations, slip planes and dislocation lines. Most importantly,
from Fig.2.11 and Fig.2.12, one can see that the truncated octahedron element serves as the
"junction" for dislocation vein structure, i.e. mutually interconnected bands or plates. This*

has some resemblances to the dislocation junction in dislocation dynamics, but not exactly the same. Because the dislocation pattern junction for a given crystal lattice has specific geometric shape, which reflects how dislocation veins interact with each other. In MCDD dislocation pattern dynamics, we essentially assume that the aggregated dislocation dipole junction has a specific shape that is determined by the original crystal lattice structure. This is a fundamental contribution to dislocation dynamics from the present work.

Chapter 4

A Temperature-dependent Atomistic-informed Strain Gradient Model

The crystal plasticity in Body-centered Cubic (BCC) crystals has two strong peculiarities: (1) the thermally-activated screw dislocation glide, which leads to temperature-induced Peierls-stress and yield stress decreases, and (2) the non-Schmid effect, i.e. a strong deviation from the Schmid law, i.e. the geometric relation between the resolved critical shear stress (RCSS) and the applied stress [59].

In this dissertation, we attempt to model the both effects from a first principle-based multiscale approach without empiricism or with less empiricism. For these purposes, we have developed a finite temperature multiscale higher order strain gradient theory. The basic kinematic assumption of multiscale higher order strain gradient theory, i.e. MCDD model, is: the bulk elements only undergo homogeneous uniform deformation, while nonlinear deformation is confined within higher order process zone elements in a hierarchical way. These so-called higher order process zone elements are distinct units of discrete dislocation patterns. We use an atomistic-informed continuum theory to model these dislocation pattern units, because they are not a single dislocation, but continuum media with dislocation density distribution. In this section, the temperature-related higher order strain gradient constitutive relation of α-phase Tantalum, which is a BCC crystal, is determined by using the Embedded-Atom Method (EAM) and higher-order Cauchy-Born rule approach.

4.1 Embedded-atom Potentials with Finite Temperature for BCC Crystals

The embedded-atom potential is an atomistic potential model for metals in molecular dynamics, which takes into account interactions between atom nucleus as well as electron

density contribution. The EAM method has been extensively used in molecular dynamics
for metallic materials.

Based on general formulation of EAM [60] [61], the EAM potential could be written as:

$$E_{tot} = \frac{1}{2} \sum_{ij} \phi(r_{ij}) + \sum_{i} F(\bar{\rho}_i), i, j = 1, 2, ... n_b \tag{4.1}$$

in which, $\phi(r_{ij})$ is the nucleus pair interaction energy, F is the electron embedding energy,
and $r_{ij} = |\boldsymbol{r}_j - \boldsymbol{r}_i|$ is the distance between atom i and atom j. Since in present work we are
modeling and simulating crystal plasticity in α-phase Tantalum, which is a BCC crystalline
material.

When we calculate the finite-temperature and free energy of atomic structure[62], the Helmholtz
free energy is the one to be considered:

$$\mathcal{F}_H = E_{tot} + k_B T \sum_{i=1}^{N} \sum_{k=1}^{3} \ln \left[2 \sinh \left(\frac{h w_{ik}}{4 \pi k_B T} \right) \right] \tag{4.2}$$

where N is the number of atoms in per unit cell, h is Planck constant, T is temperature,
k_B is the Boltzmann constant and w_{ik} are the three vibrational frequencies of atom i, for
$k = 1, 2, 3$.

In current work, we employed local quasi-harmonic model to compute the Helmholtz free energy, and we assumed the temperature is far below the melting temperature and thus atomic
modes can be decoupled. Therefore, we have following approximation of the Helmholtz free
energy,

$$\mathcal{F}_H = E_{tot} + k_B T \sum_{i=1}^{N} \sum_{k=1}^{3} \ln \left[2 \sinh \left(\frac{\hbar w_{ik}}{2 k_B T} \right) \right] \approx E_{tot} + k_B T \sum_{i=1}^{N} \sum_{k=1}^{3} \ln \left[\frac{\hbar w_{ik}}{k_B T} \right]$$
$$= E_{tot} + k_B T \sum_{i=1}^{N} 3 \ln \left(\frac{\hbar (w_{i1} w_{i2} w_{i3})^{1/3}}{k_B T} \right) = E_{tot} + k_B T \sum_{i=1}^{N} 3 \ln \left(\frac{\hbar \bar{D}_i^{1/6}}{k_B T} \right) \tag{4.3}$$

where $\hbar = h/2\pi$, $\bar{D}_i = (w_{i1} w_{i2} w_{i3})^2$. Due to the fact that we only have one atom in the
centre of unit cell for Bravais lattice, therefore we can have following simplified Helmholtz
free energy as below:

$$\mathcal{F}_H = \frac{1}{2} \sum_{j} \phi(r_j) + F(\bar{\rho}) + k_B T 3 \ln \left(\frac{\hbar \bar{D}^{1/6}}{k_B T} \right), \quad j = 1, 2, ... n_b \tag{4.4}$$

Based on the Helmholtz free energy formulation and stress-work conjugate relation, we can
split the fourth-order elastic tensor into two parts:

$$\boldsymbol{C} = \frac{\partial^2}{\partial \boldsymbol{E} \otimes \partial \boldsymbol{E}} \left(\frac{\mathcal{F}_H}{\Omega_0^u} \right) = \boldsymbol{C}_m + \boldsymbol{C}_t = \frac{\partial^2}{\partial \boldsymbol{E} \otimes \partial \boldsymbol{E}} \left(\frac{E_{tot}}{\Omega_0^u} \right) + \frac{\partial^2}{\partial \boldsymbol{E} \otimes \partial \boldsymbol{E}} \left(\frac{3 k_B T}{\Omega_0^u} \ln \frac{\hbar \bar{D}^{1/6}}{k_B T} \right)$$
$$\tag{4.5}$$

in which, $\boldsymbol{C}_m$ is shown as below:

$$
\begin{aligned}
\boldsymbol{C}_m &= \frac{\partial^2}{\partial \boldsymbol{E} \otimes \partial \boldsymbol{E}}\left(\frac{E_{tot}}{\Omega_0^u}\right)\Big|_{\boldsymbol{E}=\boldsymbol{0}} \\
&= \frac{1}{\Omega_0^u}\Bigg\{\sum_j \left[\frac{1}{2}(\phi'' - \frac{1}{r_j}\phi') + F'(\bar{\rho})(\frac{\partial^2\rho}{\partial r^2} - \frac{1}{r_j}\frac{\partial\rho}{\partial r})\right] \times \frac{\boldsymbol{R}_j \otimes \boldsymbol{R}_j \otimes \boldsymbol{R}_j \otimes \boldsymbol{R}_j}{r_j^2} \\
&+ F''(\bar{\rho})(\sum_j \frac{\partial\rho}{\partial r}\frac{\boldsymbol{R}_j \otimes \boldsymbol{R}_j}{r_j}) \otimes (\sum_j \frac{\partial\rho}{\partial r}\frac{\boldsymbol{R}_j \otimes \boldsymbol{R}_j}{r_j})\Bigg\}.
\end{aligned}
\tag{4.6}
$$

and $\boldsymbol{C}_t$ can be expressed as,

$$
\begin{aligned}
\boldsymbol{C}_t &= \frac{\partial^2}{\partial \boldsymbol{E}_{IJ}\boldsymbol{E}_{KL}}\left(\frac{3k_BT}{\Omega_0^u}\ln\frac{\hbar\bar{D}^{1/6}}{k_BT}\right) \\
&= \boldsymbol{F}_{In}^{-1}\frac{\partial^2}{\partial\boldsymbol{F}_{nJ}\partial\boldsymbol{F}_{mK}}\left(\frac{3k_BT}{\Omega_0^u}\ln\frac{\hbar\bar{D}^{1/6}}{k_BT}\right)\boldsymbol{F}_{Lm}^{-1} \\
&- \boldsymbol{F}_{In}^{-1}\boldsymbol{F}_{Km}^{-1}\frac{\partial}{\partial\boldsymbol{F}_{mJ}}\left(\frac{3k_BT}{\Omega_0^u}\ln\frac{\hbar\bar{D}^{1/6}}{k_BT}\right)\boldsymbol{F}_{Ln}^{-1}
\end{aligned}
\tag{4.7}
$$

In Eq.(4.7),

$$
\begin{aligned}
\boldsymbol{C}_{t1} &= \boldsymbol{F}_{In}^{-1}\frac{\partial^2}{\partial\boldsymbol{F}_{nJ}\otimes\partial\boldsymbol{F}_{mK}}\left(\frac{3k_BT}{\Omega_0^u}\ln\frac{\hbar\bar{D}^{1/6}}{k_BT}\right)\boldsymbol{F}_{Lm}^{-1} \\
&= \boldsymbol{F}_{In}^{-1}\frac{k_BT}{2\Omega_0^u}\left(\frac{1}{\bar{D}}\frac{\partial^2\bar{D}}{\partial\boldsymbol{F}_{nJ}\otimes\partial\boldsymbol{F}_{mK}} - \frac{1}{\bar{D}^2}\frac{\partial\bar{D}}{\partial\boldsymbol{F}_{nJ}}\otimes\frac{\partial\bar{D}}{\partial\boldsymbol{F}_{mK}}\right)\boldsymbol{F}_{Lm}^{-1}
\end{aligned}
\tag{4.8}
$$

$$
\boldsymbol{C}_{t2} = -\boldsymbol{F}_{In}^{-1}\boldsymbol{F}_{Km}^{-1}\frac{\partial}{\partial\boldsymbol{F}_{mJ}}\left(\frac{3k_BT}{\Omega_0^u}\ln\frac{\hbar\bar{D}^{1/6}}{k_BT}\right)\boldsymbol{F}_{Ln}^{-1} = -\boldsymbol{F}_{In}^{-1}\boldsymbol{F}_{Km}^{-1}\frac{k_BT}{2\Omega_0^u}\frac{1}{\bar{D}}\frac{\partial\bar{D}}{\partial\boldsymbol{F}_{mJ}}\boldsymbol{F}_{Ln}^{-1}.
\tag{4.9}
$$

Concentrating on the principle vibration modes, we ignore off-diagonal elements in $\frac{\partial^2 W_c}{\partial\boldsymbol{r}_0\otimes\boldsymbol{r}_0}$ and therefore $\bar{D} = D_{11}D_{22}D_{33}$, D_{kk} is the diagonal element in matrix $\frac{\partial^2 W_c}{\partial\boldsymbol{r}_0\otimes\boldsymbol{r}_0}$, which is shown below:

$$
\begin{aligned}
\frac{\partial^2 W_c}{\partial\boldsymbol{r}_0\otimes\partial\boldsymbol{r}_0} &= \frac{1}{\Omega_0^u}\Bigg\{F''(\bar{\rho})\sum_j\left[\rho'(r_j)\frac{\boldsymbol{r}_0-\boldsymbol{r}_j}{r_j}\right]\otimes\sum_j\left[\rho'(r_j)\frac{\boldsymbol{r}_0-\boldsymbol{r}_j}{r_j}\right] \\
&+ F'\sum_j\left[\left(\rho''(r_j)-\frac{\rho'(r_j)}{r_j}\right)\frac{\boldsymbol{r}_0-\boldsymbol{r}_j}{r_j}\otimes\frac{\boldsymbol{r}_0-\boldsymbol{r}_j}{r_j}+\frac{\rho'(r_j)}{r_j}\mathbb{1}\right] \\
&+ \frac{1}{2}\sum_j\left[\left(\phi''(r_j)-\frac{\phi'(r_j)}{r_j}\right)\frac{\boldsymbol{r}_0-\boldsymbol{r}_j}{r_j}\otimes\frac{\boldsymbol{r}_0-\boldsymbol{r}_j}{r_j}+\frac{\phi'(r_j)}{r_j}\mathbb{1}\right]\Bigg\}
\end{aligned}
$$

$$(4.10)$$

$$(4.11)$$

in which, $\boldsymbol{r}_0$ is central atom coordinate in the unit cell, $\boldsymbol{r}_j$ is neighbor atom coordinate in the unit cell. Therefore, we expand $\frac{\partial \bar{D}}{\partial \boldsymbol{F}}$ as followed,

$$\frac{\partial \bar{D}}{\partial \boldsymbol{F}} = \frac{\partial D_{11}}{\partial \boldsymbol{F}} D_{22} D_{33} + D_{11} \frac{\partial D_{22}}{\partial \boldsymbol{F}} D_{33} + D_{11} D_{22} \frac{\partial D_{33}}{\partial \boldsymbol{F}} \tag{4.12}$$

and $\frac{\partial D_{kk}}{\partial \boldsymbol{F}}$ is shown as below:

$$
\begin{aligned}
\frac{\partial D_{kk}}{\partial \boldsymbol{F}} = {} & \frac{1}{\Omega_0^u} \left\{ \frac{\partial F''(\bar{\rho})}{\partial \boldsymbol{F}} \sum_j \left[\rho'(r_j) \frac{r_{jk}}{r_j} \right] \cdot \sum_j \left[\rho'(r_j) \frac{r_{jk}}{r_j} \right] \right. \\
& + 2F''(\bar{\rho}) \sum_j \left[\frac{\partial}{\partial \boldsymbol{F}} \left(\rho'(r_j) \frac{r_{jk}}{r_j} \right) \right] \cdot \sum_j \left[\rho'(r_j) \frac{r_{jk}}{r_j} \right] \\
& + \frac{\partial F'(\bar{\rho})}{\partial \boldsymbol{F}} \sum_j \left[\left(\rho''(r_j) - \frac{\rho'(r_j)}{r_j} \right) \frac{r_{jk}^2}{r_j^2} + \frac{\rho'(r_j)}{r_j} \right] \\
& + F'(\bar{\rho}) \sum_j \left[\frac{\partial}{\partial \boldsymbol{F}} \left(\rho''(r_j) - \frac{\rho'(r_j)}{r_j} \right) \frac{r_{jk}^2}{r_j^2} \right. \\
& \left. + \left(\rho''(r_j) - \frac{\rho'(r_j)}{r_j} \right) 2 \frac{r_{jk}}{r_j} \frac{\partial}{\partial \boldsymbol{F}} \left(\frac{r_{jk}}{r_j} \right) + \frac{\partial}{\partial \boldsymbol{F}} \left(\frac{\rho'(r_j)}{r_j} \right) \right] \\[2ex]
& + \frac{1}{2} \sum_j \left[\frac{\partial}{\partial \boldsymbol{F}} \left(\phi''(r_j) - \frac{\phi'(r_j)}{r_j} \right) \frac{r_{jk}^2}{r_j^2} \right. \\
& \left. \left. + \left(\phi''(r_j) - \frac{\phi'(r_j)}{r_j} \right) 2 \frac{r_{jk}}{r_j} \frac{\partial}{\partial \boldsymbol{F}} \left(\frac{r_{jk}}{r_j} \right) + \frac{\partial}{\partial \boldsymbol{F}} \left(\frac{\phi'(r_j)}{r_j} \right) \right] \right\}
\end{aligned} \tag{4.13}
$$

The second order gradients of $\bar{D}$ and D_{kk} with respect to the deformation gradient $\boldsymbol{F}$ are

given as follows,

$$
\frac{\partial^2 \bar{D}^2}{\partial \boldsymbol{F} \otimes \partial \boldsymbol{F}} = \frac{\partial^2 D_{11}}{\partial \boldsymbol{F} \otimes \partial \boldsymbol{F}} D_{22} D_{33} + \frac{\partial D_{11}}{\partial \boldsymbol{F}} \otimes \frac{\partial D_{22}}{\partial \boldsymbol{F}} D_{33} + \frac{\partial D_{11}}{\partial \boldsymbol{F}} \otimes \frac{\partial D_{33}}{\partial \boldsymbol{F}} D_{22}
$$

$$
+ \frac{\partial D_{22}}{\partial \boldsymbol{F}} \otimes \frac{\partial D_{11}}{\partial \boldsymbol{F}} D_{33} + D_{11} \frac{\partial^2 D_{22}}{\partial \boldsymbol{F} \otimes \partial \boldsymbol{F}} D_{33} + \frac{\partial D_{22}}{\partial \boldsymbol{F}} \otimes \frac{\partial D_{33}}{\partial \boldsymbol{F}} D_{11}
$$

$$
+ \frac{\partial D_{33}}{\partial \boldsymbol{F}} \otimes \frac{\partial D_{11}}{\partial \boldsymbol{F}} D_{22} + \frac{\partial D_{33}}{\partial \boldsymbol{F}} \otimes \frac{\partial D_{22}}{\partial \boldsymbol{F}} D_{11} + \frac{\partial^2 D_{33}}{\partial \boldsymbol{F} \otimes \partial \boldsymbol{F}} D_{22} D_{11} \quad (4.14)
$$

$$
\frac{\partial^2 D_{kk}}{\partial \boldsymbol{F} \otimes \partial \boldsymbol{F}} = \frac{1}{\Omega_0^u} \left\{ \frac{\partial^2 F''(\bar{\rho})}{\partial \boldsymbol{F} \otimes \partial \boldsymbol{F}} \sum_j \left[\rho'(r_j) \frac{r_{jk}}{r_j} \right] \cdot \sum_j \left[\rho'(r_j) \frac{r_{jk}}{r_j} \right] \right.
$$

$$
+ 2 \frac{\partial F''(\bar{\rho})}{\partial \boldsymbol{F}} \otimes \sum_j \left[\frac{\partial}{\partial \boldsymbol{F}} \left(\rho'(r_j) \frac{r_{jk}}{r_j} \right) \right] \cdot \sum_j \left[\rho'(r_j) \frac{r_{jk}}{r_j} \right]
$$

$$
+ 2 \sum_j \left[\frac{\partial}{\partial \boldsymbol{F}} \left(\rho'(r_j) \frac{r_{jk}}{r_j} \right) \right] \otimes \frac{\partial F''(\bar{\rho})}{\partial \boldsymbol{F}} \cdot \sum_j \left[\rho'(r_j) \frac{r_{jk}}{r_j} \right]
$$

$$
+ 2 F''(\bar{\rho}) \sum_j \left[\frac{\partial^2}{\partial \boldsymbol{F} \otimes \partial \boldsymbol{F}} \left(\rho'(r_j) \frac{r_{jk}}{r_j} \right) \right] \cdot \sum_j \left[\rho'(r_j) \frac{r_{jk}}{r_j} \right]
$$

$$
+ 2 F''(\bar{\rho}) \sum_j \left[\frac{\partial}{\partial \boldsymbol{F}} \left(\rho'(r_j) \frac{r_{jk}}{r_j} \right) \right] \otimes \sum_j \left[\frac{\partial}{\partial \boldsymbol{F}} \left(\rho'(r_j) \frac{r_{jk}}{r_j} \right) \right]
$$

$$
+ \frac{\partial^2 F'(\bar{\rho})}{\partial \boldsymbol{F} \partial \boldsymbol{F}} \sum_j \left[\left(\rho''(r_j) - \frac{\rho'(r_j)}{r_j} \right) \frac{r_{jk}^2}{r_j^2} + \frac{\rho'(r_j)}{r_j} \right]
$$

$$
+ \frac{\partial F'(\bar{\rho})}{\partial \boldsymbol{F}} \otimes \sum_j \left[\frac{\partial}{\partial \boldsymbol{F}} \left(\rho''(r_j) - \frac{\rho'(r_j)}{r_j} \right) \frac{r_{jk}^2}{r_j^2} \right.
$$

$$
+ \left(\rho''(r_j) - \frac{\rho'(r_j)}{r_j} \right) 2 \frac{r_{jk}}{r_j} \frac{\partial}{\partial \boldsymbol{F}} \left(\frac{r_{jk}}{r_j} \right) + \frac{\partial}{\partial \boldsymbol{F}} \left(\frac{\rho'(r_j)}{r_j} \right) \right]
$$

$$
+ \sum_j \left[\left(\rho'''(r_j) - \frac{\rho''(r_j)}{r_j} + \frac{\rho'(r_j)}{r_j^2} \right) \frac{r_{jk}^2}{r_j^2} \frac{\boldsymbol{r}_j \otimes \boldsymbol{R}_j}{r_j} \right.
$$

$$
+ 2 \frac{r_{jk}}{r_j} \left(\rho''(r_j) - \frac{\rho'(r_j)}{r_j} \right) \left(\frac{1}{r_j} \frac{\partial r_{jk}}{\partial \boldsymbol{F}} - r_{jk} \frac{\boldsymbol{r}_j \otimes \boldsymbol{R}_j}{r_j^3} \right)
$$

$$
+ \left(\frac{\rho''(r_j)}{r_j} - \frac{\rho'(r_j)}{r_j^2} \right) \frac{\boldsymbol{r}_j \otimes \boldsymbol{R}_j}{r_j} \right] \otimes \frac{\partial F'(\bar{\rho})}{\partial \boldsymbol{F}}
$$

$$
+ \quad F'(\bar{\rho}) \sum_j \left[\frac{\boldsymbol{r}_j \otimes \boldsymbol{R}_j}{r_j} \otimes \frac{\partial}{\partial \boldsymbol{F}} \Big(\rho'''(r_j) - \frac{\rho''(r_j)}{r_j} + \frac{\rho'(r_j)}{r_j^2} \Big) \frac{r_{jk}^2}{r_j^2} \right.
$$

$$
+ \quad \Big(\rho'''(r_j) - \frac{\rho''(r_j)}{r_j} + \frac{\rho'(r_j)}{r_j^2} \Big) \frac{\partial}{\partial \boldsymbol{F}} \Big(\frac{\boldsymbol{r}_j \otimes \boldsymbol{R}_j}{r_j} \Big) \frac{r_{jk}^2}{r_j^2}
$$

$$
+ \quad \Big(\rho'''(r_j) - \frac{\rho''(r_j)}{r_j} + \frac{\rho'(r_j)}{r_j^2} \Big) \frac{\boldsymbol{r}_j \otimes \boldsymbol{R}_j}{r_j} \otimes \frac{\partial}{\partial \boldsymbol{F}} \Big(\frac{r_{jk}^2}{r_j^2} \Big)
$$

$$
+ \quad 2 \Big(\rho''(r_j) - \frac{\rho'(r_j)}{r_j} \Big) \Big(\frac{1}{r_j} \frac{\partial r_{jk}}{\partial \boldsymbol{F}} - r_{jk} \frac{\boldsymbol{r}_j \otimes \boldsymbol{R}_j}{r_j^3} \Big) \otimes \frac{\partial}{\partial \boldsymbol{F}} \Big(\frac{r_{jk}}{r_j} \Big)
$$

$$
+ \quad 2 \frac{r_{jk}}{r_j} \Big(\frac{1}{r_j} \frac{\partial r_{jk}}{\partial \boldsymbol{F}} - r_{jk} \frac{\boldsymbol{r}_j \otimes \boldsymbol{R}_j}{r_j^3} \Big) \otimes \frac{\partial}{\partial \boldsymbol{F}} \Big(\rho''(r_j) - \frac{\rho'(r_j)}{r_j} \Big)
$$

$$
+ \quad 2 \frac{r_{jk}}{r_j} \Big(\rho''(r_j) - \frac{\rho'(r_j)}{r_j} \Big) \frac{\partial}{\partial \boldsymbol{F}} \Big(\frac{1}{r_j} \frac{\partial r_{jk}}{\partial \boldsymbol{F}} - r_{jk} \frac{\boldsymbol{r}_j \otimes \boldsymbol{R}_j}{r_j^3} \Big)
$$

$$
+ \quad \frac{\boldsymbol{r}_j \otimes \boldsymbol{R}_j}{r_j} \otimes \frac{\partial}{\partial \boldsymbol{F}} \Big(\frac{\rho''(r_j)}{r_j} - \frac{\rho'(r_j)}{r_j^2} \Big) + \Big(\frac{\rho''(r_j)}{r_j} - \frac{\rho'(r_j)}{r_j^2} \Big) \frac{\partial}{\partial \boldsymbol{F}} \Big(\frac{\boldsymbol{r}_j \otimes \boldsymbol{R}_j}{r_j} \Big) \right]
$$

$$
+ \quad \frac{1}{2} \sum_j \left[\frac{\boldsymbol{r}_j \otimes \boldsymbol{R}_j}{r_j} \otimes \frac{\partial}{\partial \boldsymbol{F}} \Big(\phi'''(r_j) - \frac{\phi''}{r_j} + \frac{\phi'(r_j)}{r_j^2} \Big) \frac{r_{jk}^2}{r_j^2} \right.
$$

$$
+ \quad \Big(\phi'''(r_j) - \frac{\phi''(r_j)}{r_j} + \frac{\phi'(r_j)}{r_j^2} \Big) \frac{\partial}{\partial \boldsymbol{F}} \Big(\frac{\boldsymbol{r}_j \otimes \boldsymbol{R}_j}{r_j} \Big) \frac{r_{jk}^2}{r_j^2}
$$

$$
+ \quad \Big(\phi'''(r_j) - \frac{\phi''(r_j)}{r_j} + \frac{\phi'(r_j)}{r_j^2} \Big) \frac{\boldsymbol{r}_j \otimes \boldsymbol{R}_j}{r_j} \otimes \frac{\partial}{\partial \boldsymbol{F}} \Big(\frac{r_{jk}^2}{r_j^2} \Big)
$$

$$
+ \quad 2 \Big(\phi''(r_j) - \frac{\phi'(r_j)}{r_j} \Big) \Big(\frac{1}{r_j} \frac{\partial r_{jk}}{\partial \boldsymbol{F}} - r_{jk} \frac{\boldsymbol{r}_j \otimes \boldsymbol{R}_j}{r_j^3} \Big) \otimes \frac{\partial}{\partial \boldsymbol{F}} \Big(\frac{r_{jk}}{r_j} \Big)
$$

$$
+ \quad 2 \frac{r_{jk}}{r_j} \Big(\frac{1}{r_j} \frac{\partial r_{jk}}{\partial \boldsymbol{F}} - r_{jk} \frac{\boldsymbol{r}_j \otimes \boldsymbol{R}_j}{r_j^3} \Big) \otimes \frac{\partial}{\partial \boldsymbol{F}} \Big(\phi''(r_j) - \frac{\phi'(r_j)}{r_j} \Big)
$$

$$
+ \quad 2 \frac{r_{jk}}{r_j} \Big(\phi''(r_j) - \frac{\phi'(r_j)}{r_j} \Big) \frac{\partial}{\partial \boldsymbol{F}} \Big(\frac{1}{r_j} \frac{\partial r_{jk}}{\partial \boldsymbol{F}} - r_{jk} \frac{\boldsymbol{r}_j \otimes \boldsymbol{R}_j}{r_j^3} \Big)
$$

$$
+ \quad \frac{\boldsymbol{r}_j \otimes \boldsymbol{R}_j}{r_j} \otimes \frac{\partial}{\partial \boldsymbol{F}} \Big(\frac{\phi''(r_j)}{r_j} - \frac{\phi'(r_j)}{r_j^2} \Big) + \Big(\frac{\phi''(r_j)}{r_j} - \frac{\phi'(r_j)}{r_j^2} \Big) \frac{\partial}{\partial \boldsymbol{F}} \Big(\frac{\boldsymbol{r}_j \otimes \boldsymbol{R}_j}{r_j} \Big) \right] \Bigg\}, \quad (4.15)
$$

where the free index $k = 1, 2, 3$.

To validate the above formulations of temperature-dependent fourth-order elastic tensor, we make a comparison with experimental elastic constants under different temperatures as shown below. In this test, we employ 8 α-phase Tantalum BCC atom shells as a unit cell to represent the physical properties. In Fig.4.1, the red lines represent numerical results and the blue lines represent experimental data [63]. The numerical results are basically linearly decreased with increasing temperature which has the same tendency as the experimental
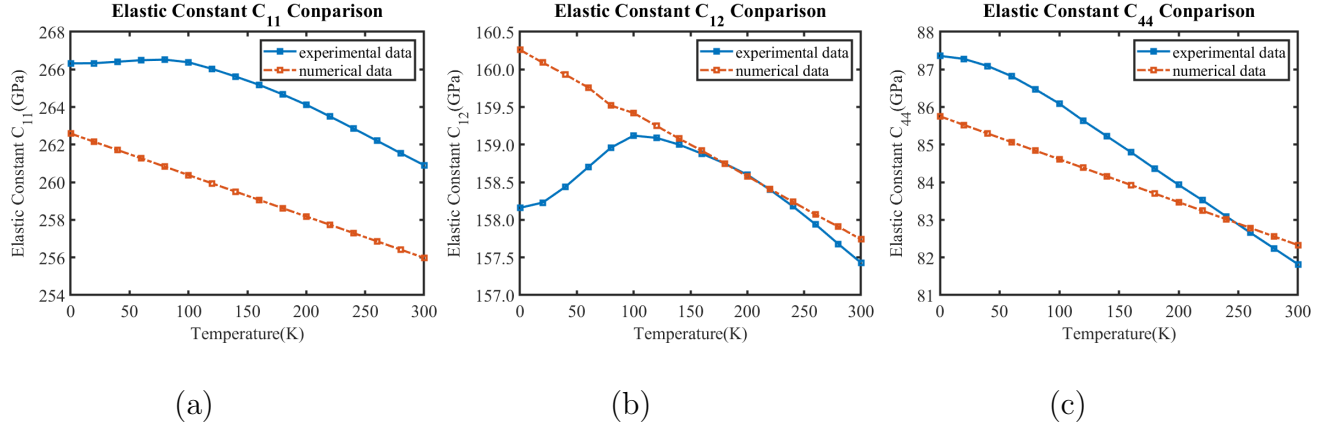
Figure 4.1: Temperature-related elastic constants comparison: (a)C_{11}. (b)C_{12}. (c)C_{44}. at different temperature

data. And the relative error $\frac{C_{exp} - C_{numerical}}{C_{exp}}$ between numerical results and experimental data are: $1.4\% \sim 2.3\%$ for C_{11}, $0.005\% \sim 1.7\%$ for C_{12} and $0.0027\% \sim 5.7\%$ for C_{44}. Therefore, we can consider the above temperature-related elastic tensor formulations valid.

4.2 Temperature-dependent Stress Measures in Higher Order Process Zones

The macroscale constitutive relation is expressed in terms of several important stress measures as follows,

$$
\begin{aligned}
\boldsymbol{P} &= \frac{\partial}{\partial \boldsymbol{F}}\left(\frac{E_{tot}}{\Omega_0^u}\right) + \frac{\partial}{\partial \boldsymbol{F}}\left(\frac{3k_BT}{\Omega_0^u}\ln\frac{\hbar\bar{D}^{1/6}}{k_BT}\right) \\
&= \frac{1}{\Omega_0^u}\sum_{j=1}^{n_b}\left(F'(\bar{\rho})\rho'(r_j) + \frac{1}{2}\phi'(r_j)\right)\frac{\boldsymbol{r}_j \otimes \boldsymbol{R}_j}{r_j} + \frac{k_BT}{2\Omega_0^u}\frac{1}{\bar{D}}\frac{\partial\bar{D}}{\partial\boldsymbol{F}} \quad (4.16)
\end{aligned}
$$

$$
\boldsymbol{S} = \boldsymbol{F}^{-1}\boldsymbol{P} = \frac{1}{\Omega_0^u}\sum_{j=1}^{n_b}\left(F'(\bar{\rho})\rho'(r_j) + \frac{1}{2}\phi'(r_j)\right)\frac{\boldsymbol{R}_j \otimes \boldsymbol{R}_j}{r_j} + \frac{k_BT}{2\Omega_0^u}\frac{\boldsymbol{F}^{-1}}{\bar{D}}\frac{\partial\bar{D}}{\partial\boldsymbol{F}} \quad (4.17)
$$

$$
\boldsymbol{\sigma} = J^{-1}\boldsymbol{P}\boldsymbol{F}^T = \frac{1}{\Omega^u}\sum_{j=1}^{n_b}\left(F'(\bar{\rho})\rho'(r_j) + \frac{1}{2}\phi'(r_j)\right)\frac{\boldsymbol{r}_j \otimes \boldsymbol{r}_j}{r_j} + \frac{k_BT}{2\Omega^u}\frac{\partial\bar{D}}{\partial\boldsymbol{F}}\frac{\boldsymbol{F}^T}{\bar{D}} . \quad (4.18)
$$

Unlike in discrete dislocation dynamics, in the geometrically-compatible dislocation pattern dynamics, the discrete dislocation pattern segment has no core structure; instead, the overall effect of the dislocation core structure manifests itself as a continuum level higher order strain gradient theory [64, 65].

Remark 4.1. *To find initial equilibrium state for many-body potential problem, we use the
general or generic analytical form of EAM potential without consideration of temperature
effect. The* <u>*initial equilibrium condition*</u> *is to be considered which is defined as the stress-free
state in an* <u>*undeformed configuration,*</u>

$$\boldsymbol{S} = \frac{1}{\Omega_0^u} \sum_{j=1}^{n_b} \left(F'(\bar{\rho})\rho'(r_j) + \frac{1}{2}\phi'(r_j) \right) \frac{\boldsymbol{R}_j \otimes \boldsymbol{R}_j}{r_j} = \boldsymbol{0} \tag{4.19}$$

*Based on the equation above, the equilibrium lattice constant a can be computed, which sat-
isfies the initial equilibrium condition. Thus it becomes an optimization problem with one
variable and firstly the derivative of norm of* $\boldsymbol{S}$ *about lattice constant a can be found:*

$$\frac{\partial \|\boldsymbol{S}\|_F}{\partial a} = \frac{\partial \|\boldsymbol{S}\|_F}{\partial \boldsymbol{S}} : \frac{\partial \boldsymbol{S}}{\partial a} = 2\boldsymbol{S} : \frac{\partial \boldsymbol{S}}{\partial a} = 0 \tag{4.20}$$

*To solve this nonlinear equation, the Newton-Raphson method is used to linearize the above
equation,*

$$\frac{\partial \|\boldsymbol{S}\|_F}{\partial a}(a^{i+1}) = \frac{\partial \|\boldsymbol{S}\|_F}{\partial a}(a^i) + \frac{\partial^2 \|\boldsymbol{S}\|_F}{\partial a^2}\Delta a^i = 0 \tag{4.21}$$

Therefore, one is obtained that the ith iteration a^i *as,*

$$\Delta a^i = -\frac{\partial \|\boldsymbol{S}\|_F}{\partial a}(a^i) \Big/ \frac{\partial^2 \|\boldsymbol{S}\|_F}{\partial a^2} \tag{4.22}$$

the iterative solution stops until $\|\Delta a^i\| < tol.$
The analytical form of $\frac{\partial^2 \|\boldsymbol{S}\|_F}{\partial a^2}$ *is given as,*

$$\frac{\partial^2 \|\boldsymbol{S}\|_F}{\partial a^2} = \frac{\partial}{\partial a}\left(2\boldsymbol{S} : \frac{\partial \boldsymbol{S}}{\partial a} \right) = 2\frac{\partial \boldsymbol{S}}{\partial a} : \frac{\partial \boldsymbol{S}}{\partial a} + 2\boldsymbol{S} : \frac{\partial^2 \boldsymbol{S}}{\partial a^2} \tag{4.23}$$

in which,

$$\frac{\partial \boldsymbol{S}}{\partial a} = \sum_j \left\{ a \left[F''(\bar{\rho})(\rho'(r_j))^2 + F'(\bar{\rho})\rho''(r_j) + \frac{1}{2}\phi''(r_j) + \frac{F'(\bar{\rho})\rho'(r_j) + \frac{1}{2}\phi'(r_j)}{r_j} \right] \boldsymbol{R}_j \otimes \boldsymbol{R}_j \right\} \tag{4.24}$$

$$\begin{aligned}
\frac{\partial^2 \boldsymbol{S}}{\partial a^2} = \sum_j \Bigg\{ & F''(\bar{\rho})(\rho'(r_j))^2 + F'(\bar{\rho})\rho''(r_j) + \frac{1}{2}\phi''(r_j) \\
& + r_j \left[F'''(\bar{\rho})(\rho'(r_j))^3 + 2F''(\bar{\rho})\rho'(r_j)\rho''(r_j) \right] + r_j \left[F''(\bar{\rho})\rho'(r_j)\rho''(r_j) + F'(\bar{\rho})\rho'''(r_j) \right] \\
& + \frac{1}{2}r_j\phi'''(r_j) + F''(\bar{\rho})(\rho'(r_j))^2 + F'(\bar{\rho})\rho''(r_j) + \frac{1}{2}\phi''(r_j) \Bigg\} \boldsymbol{R}_j \otimes \boldsymbol{R}_j
\end{aligned} \tag{4.25}$$

To model the dislocation pattern segments with the strain gradient theory, we employ an atomistic-informed higher order strain gradient theory to all the process zone elements (discrete dislocation patterns). Since there are three distinct geometrically-compatible dislocation pattern segments, we use three hierarchical order strain gradients to model them,

$$\mathbf{G} = \frac{\partial^2 \mathbf{x}}{\partial \mathbf{X} \otimes \partial \mathbf{X}}, \ \mathbf{H} = \frac{\partial^3 \mathbf{x}}{\partial \mathbf{X} \otimes \partial \mathbf{X} \otimes \partial \mathbf{X}}, \ \mathbf{K} = \frac{\partial^4 \mathbf{x}}{\partial \mathbf{X} \otimes \partial \mathbf{X} \otimes \partial \mathbf{X} \otimes \partial \mathbf{X}}. \tag{4.26}$$

Then the bond vectors in corresponding dislocation pattern segments may be defined by the higher order Cauchy-Born model as follows,

$$\mathbf{r}_j \ = \ \mathbf{F} \cdot \mathbf{R}_j + \frac{1}{2}\mathbf{G} : (\mathbf{R}_j \otimes \mathbf{R}_j), \tag{4.27}$$

$$\mathbf{r}_j \ = \ \mathbf{F} \cdot \mathbf{R}_j + \frac{1}{2!}\mathbf{G} : (\mathbf{R}_j \otimes \mathbf{R}_j) + \frac{1}{3!}\mathbf{H} \vdots (\mathbf{R}_j \otimes \mathbf{R}_j \otimes \mathbf{R}_j), \tag{4.28}$$

$$\mathbf{r}_j \ = \ \mathbf{F} \cdot \mathbf{R}_j + \frac{1}{2!}\mathbf{G} : (\mathbf{R}_j \otimes \mathbf{R}_j) + \frac{1}{3!}\mathbf{H} \vdots (\mathbf{R}_j \otimes \mathbf{R}_j \otimes \mathbf{R}_j)$$
$$+ \frac{1}{4!}\mathbf{K} :: (\mathbf{R}_j \otimes \mathbf{R}_j \otimes \mathbf{R}_j \otimes \mathbf{R}_j), \tag{4.29}$$

respectively. Subsequently, as a function of deformation gradients, the strain energy W_w, W_p, and W_t of the corresponding dislocation pattern elements are considered, which can be

expressed as follows,

$$
\begin{aligned}
W_w &= \frac{1}{\Omega_0^u}\left[f(\bar{\rho}) + \frac{1}{2}\sum_{i=1}^{n_b}\phi\Big(\Big|\boldsymbol{F}\cdot\boldsymbol{R}_i + \frac{1}{2!}\mathbf{G}:(\mathbf{R}_i\otimes\mathbf{R}_i)\Big|\Big)\right] \\
&+ \frac{3k_BT}{\Omega_0^u}\ln\left(\frac{\hbar\bar{D}^{1/6}\Big(\Big|\boldsymbol{F}\cdot\boldsymbol{R}_i + \frac{1}{2!}\mathbf{G}:(\mathbf{R}_i\otimes\mathbf{R}_i)\Big|\Big)}{k_BT}\right),
\end{aligned}
\tag{4.30}
$$

$$
\begin{aligned}
W_p &= \frac{1}{\Omega_0^u}\left[f(\bar{\rho}) + \frac{1}{2}\sum_{i=1}^{n_b}\phi\Big(\Big|\mathbf{F}\cdot\mathbf{R}_j + \frac{1}{2!}\mathbf{G}:(\mathbf{R}_j\otimes\mathbf{R}_j) + \frac{1}{3!}\mathbf{H}\vdots(\mathbf{R}_j\otimes\mathbf{R}_j\otimes\mathbf{R}_j)\Big|\Big)\right] \\
&+ \frac{3k_BT}{\Omega_0^u}\ln\left(\frac{\hbar\bar{D}^{1/6}\Big(\Big|\mathbf{F}\cdot\mathbf{R}_j + \frac{1}{2!}\mathbf{G}:(\mathbf{R}_j\otimes\mathbf{R}_j) + \frac{1}{3!}\mathbf{H}\vdots(\mathbf{R}_j\otimes\mathbf{R}_j\otimes\mathbf{R}_j)\Big|\Big)}{k_BT}\right),
\end{aligned}
\tag{4.31}
$$

$$
\begin{aligned}
W_t &= \frac{1}{\Omega_0^u}\left[f(\bar{\rho}) + \frac{1}{2}\sum_{i=1}^{n_b}\phi\Big(\Big|\mathbf{F}\cdot\mathbf{R}_j + \frac{1}{2!}\mathbf{G}:(\mathbf{R}_j\otimes\mathbf{R}_j) + \frac{1}{3!}\mathbf{H}\vdots(\mathbf{R}_j\otimes\mathbf{R}_j\otimes\mathbf{R}_j)\right. \\
&\quad + \left.\frac{1}{4!}\mathbf{K}::(\mathbf{R}_j\otimes\mathbf{R}_j\otimes\mathbf{R}_j\otimes\mathbf{R}_j)\Big|\Big)\right] \\
&+ \frac{3k_BT}{\Omega_0^u}\ln\left(\frac{\hbar}{k_BT}\bar{D}^{1/6}\Big(\Big|\mathbf{F}\cdot\mathbf{R}_j + \frac{1}{2!}\mathbf{G}:(\mathbf{R}_j\otimes\mathbf{R}_j) + \frac{1}{3!}\mathbf{H}\vdots(\mathbf{R}_j\otimes\mathbf{R}_j\otimes\mathbf{R}_j)\right.\right. \\
&\quad + \left.\left.\frac{1}{4!}\mathbf{K}::(\mathbf{R}_j\otimes\mathbf{R}_j\otimes\mathbf{R}_j\otimes\mathbf{R}_j)\Big|\Big)\right).
\end{aligned}
\tag{4.32}
$$

4.2.1 Stress Measures in 1st-order Process Zone

The constitutive relations in wedge elements can be further explicated as follows,

$$
\boldsymbol{P} = \frac{\partial W_w(\boldsymbol{F},\boldsymbol{G})}{\partial\boldsymbol{F}}, \boldsymbol{Q} = \frac{\partial W_w(\boldsymbol{F},\boldsymbol{G})}{\partial\boldsymbol{G}};
\tag{4.33}
$$

The higher order stress tensor is expressed in a general form as

$$
\mathbf{Q} = \frac{1}{2\Omega_0^u}\sum_{j=1}^{n_b}\left(\frac{1}{2}\phi'(r_j) + F'(\bar{\rho})\rho'(r_j)\right)\frac{\mathbf{r}_j\otimes\mathbf{R}_j\otimes\mathbf{R}_j}{r_j} + \frac{1}{2\Omega_0^u}\frac{k_BT}{\bar{D}}\frac{\partial\bar{D}}{\partial\boldsymbol{G}}
\tag{4.34}
$$

in which,

$$
\frac{\partial\bar{D}}{\partial\boldsymbol{G}} = \frac{\partial D_{11}}{\partial\boldsymbol{G}}D_{22}D_{33} + D_{11}\frac{\partial D_{22}}{\partial\boldsymbol{G}}D_{33} + D_{11}D_{22}\frac{\partial D_{33}}{\partial\boldsymbol{G}}
\tag{4.35}
$$

and

$$
\begin{aligned}
\frac{\partial D_{kk}}{\partial \boldsymbol{G}} &= \frac{1}{\Omega_0^u}\Bigg\{ F'''(\bar\rho)\sum_j \Big[\rho'(r_j)\frac{\partial r_j}{\partial \boldsymbol{G}}\Big]\cdot\sum_j\Big[\rho'(r_j)\frac{r_{jk}}{r_j}\Big]\cdot\sum_j\Big[\rho'(r_j)\frac{r_{jk}}{r_j}\Big] \\
&+\ 2F''(\bar\rho)\sum_j\Big[\frac{\partial}{\partial \boldsymbol{G}}\big(\rho'(r_j)\frac{r_{jk}}{r_j}\big)\Big]\cdot\Big[\rho'(r_j)\frac{r_{jk}}{r_j}\Big] \\
&+\ F''(\bar\rho)\sum_j\Big[\rho'(r_j)\frac{\partial r_j}{\partial \boldsymbol{G}}\Big]\cdot\sum_j\Big[(\rho''(r_j)-\frac{\rho'(r_j)}{r_j})\frac{r_{jk}^2}{r_j^2}+\frac{\rho'(r_j)}{r_j}\Big] \\
&+\ F'(\bar\rho)\sum_j\Big[\frac{\partial}{\partial \boldsymbol{G}}(\rho'(r_j)-\frac{\rho'(r_j)}{r_j})\frac{r_{jk}^2}{r_j^2}+2(\rho''(r_j)-\frac{\rho'(r_j)}{r_j})\frac{r_{jk}}{r_j}\frac{\partial}{\partial \boldsymbol{G}}(\frac{r_{jk}}{r_j})+\frac{\partial}{\partial \boldsymbol{G}}(\frac{\rho'(r_j)}{r_j})\Big] \\
&+\ \frac{1}{2}\sum_j\Big[\frac{\partial}{\partial \boldsymbol{G}}(\phi'''(r_j)-\frac{\phi'(r_j)}{r_j})\frac{r_{jk}^2}{r_j^2}+2(\phi''(r_j)-\frac{\phi'(r_j)}{r_j})\frac{r_{jk}}{r_j}\frac{\partial}{\partial \boldsymbol{G}}(\frac{r_{jk}}{r_j})+\frac{\partial}{\partial \boldsymbol{G}}(\frac{\phi'(r_j)}{r_j})\Big]\Bigg\}\ .
\end{aligned}
\tag{4.36}
$$

where the free index $k = 1, 2, 3$.

4.2.2 Stress Measures in 2nd-order Process Zone

The constitutive relation in prism element can further explicated as follows,

$$
\boldsymbol{P}=\frac{\partial W_p(\boldsymbol{F},\boldsymbol{G},\boldsymbol{H})}{\partial \boldsymbol{F}}, \boldsymbol{Q}=\frac{\partial W_p(\boldsymbol{F},\boldsymbol{G},\boldsymbol{H})}{\partial \boldsymbol{G}}, \boldsymbol{U}=\frac{\partial W_p(\boldsymbol{F},\boldsymbol{G},\boldsymbol{H})}{\partial \boldsymbol{H}};
\tag{4.37}
$$

The higher order stress tensors are expressed in a general form as

$$
\begin{aligned}
\mathbf{Q} &= \frac{1}{2\Omega_0^u}\sum_{j=1}^{n_b}\left(\frac{1}{2}\phi'(r_j)+F'(\bar\rho)\rho'(r_j)\right)\frac{\mathbf{r}_j\otimes\mathbf{R}_j\otimes\mathbf{R}_j}{r_j}+\frac{1}{2\Omega_0^u}\frac{k_BT}{\bar D}\frac{\partial \bar D}{\partial \boldsymbol{G}}, \\
\mathbf{U} &= \frac{1}{2\Omega_0^u}\sum_{j=1}^{n_b}\left(\frac{1}{2}\phi'(r_j)+F'(\bar\rho)\rho'(r_j)\right)\frac{\mathbf{r}_j\otimes\mathbf{R}_j\otimes\mathbf{R}_j\otimes\mathbf{R}_j}{r_j}+\frac{1}{2\Omega_0^u}\frac{k_BT}{\bar D}\frac{\partial \bar D}{\partial \boldsymbol{H}}\ .
\end{aligned}
\tag{4.38}
$$

in which,

$$
\frac{\partial \bar D}{\partial \boldsymbol{H}}=\frac{\partial D_{11}}{\partial \boldsymbol{H}}D_{22}D_{33}+D_{11}\frac{\partial D_{22}}{\partial \boldsymbol{H}}D_{33}+D_{11}D_{22}\frac{\partial D_{33}}{\partial \boldsymbol{H}}
\tag{4.39}
$$

and

$$
\begin{aligned}
\frac{\partial D_{kk}}{\partial \boldsymbol{H}} = \frac{1}{\Omega_0^u} \Bigg\{ & F'''(\bar{\rho}) \sum_j \left[\rho'(r_j) \frac{\partial r_j}{\partial \boldsymbol{H}} \right] \cdot \sum_j \left[\rho'(r_j) \frac{r_{jk}}{r_j} \right] \cdot \sum_j \left[\rho'(r_j) \frac{r_{jk}}{r_j} \right] \\
& + 2F''(\bar{\rho}) \sum_j \left[\frac{\partial}{\partial \boldsymbol{H}} \left(\rho'(r_j) \frac{r_{jk}}{r_j} \right) \right] \cdot \left[\rho'(r_j) \frac{r_{jk}}{r_j} \right] \\
& + F''(\bar{\rho}) \sum_j \left[\rho'(r_j) \frac{\partial r_j}{\partial \boldsymbol{H}} \right] \cdot \sum_j \left[(\rho''(r_j) - \frac{\rho'(r_j)}{r_j}) \frac{r_{jk}^2}{r_j^2} + \frac{\rho'(r_j)}{r_j} \right] \\
& + F'(\bar{\rho}) \sum_j \left[\frac{\partial}{\partial \boldsymbol{H}} (\rho'(r_j) - \frac{\rho'(r_j)}{r_j}) \frac{r_{jk}^2}{r_j^2} + 2(\rho''(r_j) - \frac{\rho'(r_j)}{r_j}) \frac{r_{jk}}{r_j} \frac{\partial}{\partial \boldsymbol{H}} (\frac{r_{jk}}{r_j}) + \frac{\partial}{\partial \boldsymbol{H}} (\frac{\rho'(r_j)}{r_j}) \right] \\
& + \frac{1}{2} \sum_j \left[\frac{\partial}{\partial \boldsymbol{H}} (\phi'''(r_j) - \frac{\phi'(r_j)}{r_j}) \frac{r_{jk}^2}{r_j^2} + 2(\phi''(r_j) - \frac{\phi'(r_j)}{r_j}) \frac{r_{jk}}{r_j} \frac{\partial}{\partial \boldsymbol{H}} (\frac{r_{jk}}{r_j}) + \frac{\partial}{\partial \boldsymbol{H}} (\frac{\phi'(r_j)}{r_j}) \right] \Bigg\} .
\end{aligned}
\tag{4.40}
$$

where $k = 1, 2, 3$.

4.2.3 Stress Measures in 3rd-order Process Zone

The constitutive relation in truncated octahedron element can further explicated as follows:

$$
\boldsymbol{P} = \frac{\partial W_t(\boldsymbol{F}, \boldsymbol{G}, \boldsymbol{H}, \boldsymbol{K})}{\partial \boldsymbol{F}},
\tag{4.41}
$$

$$
\boldsymbol{Q} = \frac{\partial W_t(\boldsymbol{F}, \boldsymbol{G}, \boldsymbol{H}, \boldsymbol{K})}{\partial \boldsymbol{G}},
\tag{4.42}
$$

$$
\boldsymbol{U} = \frac{\partial W_t(\boldsymbol{F}, \boldsymbol{G}, \boldsymbol{H}, \boldsymbol{K})}{\partial \boldsymbol{H}},
\tag{4.43}
$$

$$
\boldsymbol{V} = \frac{\partial W_t(\boldsymbol{F}, \boldsymbol{G}, \boldsymbol{H}, \boldsymbol{K})}{\partial \boldsymbol{K}}.
\tag{4.44}
$$

The higher order stress tensors are expressed in a general form as

$$
\mathbf{Q} = \frac{1}{2\Omega_0^u} \sum_{j=1}^{n_b} \left(\frac{1}{2} \phi'(r_j) + F'(\bar{\rho}) \rho'(r_j) \right) \frac{\mathbf{r}_j \otimes \mathbf{R}_j \otimes \mathbf{R}_j}{r_j} + \frac{1}{2\Omega_0^u} \frac{k_B T}{\bar{D}} \frac{\partial \bar{D}}{\partial \boldsymbol{G}},
$$

$$
\mathbf{U} = \frac{1}{2\Omega_0^u} \sum_{j=1}^{n_b} \left(\frac{1}{2} \phi'(r_j) + F'(\bar{\rho}) \rho'(r_j) \right) \frac{\mathbf{r}_j \otimes \mathbf{R}_j \otimes \mathbf{R}_j \otimes \mathbf{R}_j}{r_j} + \frac{1}{2\Omega_0^u} \frac{k_B T}{\bar{D}} \frac{\partial \bar{D}}{\partial \boldsymbol{H}},
\tag{4.45}
$$

$$
\mathbf{V} = \frac{1}{2\Omega_0^u} \sum_{j=1}^{n_b} \left(\frac{1}{2} \phi'(r_j) + F'(\bar{\rho}) \rho'(r_j) \right) \frac{\mathbf{r}_j \otimes \mathbf{R}_j \otimes \mathbf{R}_j \otimes \mathbf{R}_j \otimes \mathbf{R}_j}{r_j} + \frac{1}{2\Omega_0^u} \frac{k_B T}{\bar{D}} \frac{\partial \bar{D}}{\partial \boldsymbol{K}} .
$$

in which,

$$
\frac{\partial \bar{D}}{\partial \boldsymbol{K}} = \frac{\partial D_{11}}{\partial \boldsymbol{K}} D_{22} D_{33} + D_{11} \frac{\partial D_{22}}{\partial \boldsymbol{K}} D_{33} + D_{11} D_{22} \frac{\partial D_{33}}{\partial \boldsymbol{K}}
\tag{4.46}
$$

and

$$
\begin{aligned}
\frac{\partial D_{kk}}{\partial \boldsymbol{K}} \;=\;\; & \frac{1}{\Omega_0^u}\Bigg\{ F'''(\bar{\rho}) \sum_j \left[\rho'(r_j)\frac{\partial r_j}{\partial \boldsymbol{K}} \right] \cdot \sum_j \left[\rho'(r_j)\frac{r_{jk}}{r_j} \right] \cdot \sum_j \left[\rho'(r_j)\frac{r_{jk}}{r_j} \right] \\[2mm]
& + \; 2F''(\bar{\rho}) \sum_j \left[\frac{\partial}{\partial \boldsymbol{K}}\left(\rho'(r_j)\frac{r_{jk}}{r_j} \right) \right] \cdot \left[\rho'(r_j)\frac{r_{jk}}{r_j} \right] \\[2mm]
& + \; F''(\bar{\rho}) \sum_j \left[\rho'(r_j)\frac{\partial r_j}{\partial \boldsymbol{K}} \right] \cdot \sum_j \left[(\rho''(r_j) - \frac{\rho'(r_j)}{r_j})\frac{r_{jk}^2}{r_j^2} + \frac{\rho'(r_j)}{r_j} \right] \\[2mm]
& + \; F'(\bar{\rho}) \sum_j \left[\frac{\partial}{\partial \boldsymbol{K}}(\rho'(r_j) - \frac{\rho'(r_j)}{r_j})\frac{r_{jk}^2}{r_j^2} + 2(\rho''(r_j) - \frac{\rho'(r_j)}{r_j})\frac{r_{jk}}{r_j}\frac{\partial}{\partial \boldsymbol{K}}(\frac{r_{jk}}{r_j}) + \frac{\partial}{\partial \boldsymbol{K}}(\frac{\rho'(r_j)}{r_j}) \right] \\[2mm]
& + \; \frac{1}{2}\sum_j \left[\frac{\partial}{\partial \boldsymbol{K}}(\phi'''(r_j) - \frac{\phi'(r_j)}{r_j})\frac{r_{jk}^2}{r_j^2} + 2(\phi''(r_j) - \frac{\phi'(r_j)}{r_j})\frac{r_{jk}}{r_j}\frac{\partial}{\partial \boldsymbol{H}}(\frac{r_{jk}}{r_j}) + \frac{\partial}{\partial \boldsymbol{K}}(\frac{\phi'(r_j)}{r_j}) \right] \Bigg\}, \\[2mm]
& k = 1,2,3 \quad .
\end{aligned}
\tag{4.47}
$$

Chapter 5

Finite Element Formulation

5.1 MCDD FEM Implementation

Taking displacement variation, the Hamilton principle can be written as,

$$\delta \int_{t_0}^{t_1} (\mathcal{T} - \mathcal{W}_{int})dt + \int_{t_0}^{t_1} \delta \mathcal{W}_{ext} dt = 0 \tag{5.1}$$

in which, $\mathcal{W}_{int} = \int_V W(\boldsymbol{F}, \boldsymbol{G}, \boldsymbol{H}, \boldsymbol{K})dV$ is the strain and higher order stain gradient energy density, $\mathcal{T} = \int_V \frac{1}{2}\rho \dot{\boldsymbol{u}} \cdot \dot{\boldsymbol{u}}dV$ is the kinetic energy of the crystalline solid, $\mathcal{W}_{ext}$ is the external potential energy.

The variational form of kinetic energy:

$$\delta \mathcal{T} = \int_V \rho \dot{\boldsymbol{u}} \cdot \delta \dot{\boldsymbol{u}}dV$$

The variational form of internal energy:

$$\delta \mathcal{W}_{int} = \int_V \left\{ \frac{\partial W}{\partial \boldsymbol{W}} : \delta \boldsymbol{F} + \frac{\partial W}{\partial \boldsymbol{G}} \vdots \delta \boldsymbol{G} + \frac{\partial W}{\partial \boldsymbol{H}} :: \delta \boldsymbol{H} + \frac{\partial W}{\partial \boldsymbol{K}} : \vdots \delta \boldsymbol{K} \right\} dV$$

The variational form of external energy:

$$\delta \mathcal{W}_{ext} = \int_V \boldsymbol{b} \cdot \delta \boldsymbol{u}dV + \int_{\partial V_t} \bar{\boldsymbol{T}} \cdot \delta \boldsymbol{u}dS$$

Substituting those formulations above into the formulation of the Hamilton principle, we can have Galerkin weak form of Multiscale Crystal Defects Dynamics of continuum crystalline solid as follows,

$$\int_\Omega \left[\rho \ddot{\boldsymbol{u}} \cdot \delta \boldsymbol{u} + \boldsymbol{P} : \delta \boldsymbol{F} + \boldsymbol{Q} \vdots \delta \boldsymbol{G} + \boldsymbol{U} :: \delta \boldsymbol{H} + \boldsymbol{V} : \vdots \delta \boldsymbol{K} \right] dV = \int_\Omega \boldsymbol{b} \cdot \delta \boldsymbol{u}dV + \int_{\partial \Omega_t} \bar{\boldsymbol{T}} \cdot \delta \boldsymbol{u}dS \tag{5.2}$$

Specifically, we can rewrite the form of considering different types of elements as:

$$\sum_{e=1}^{n_{elem}^{p0}} \left\{ \int_{\Omega_{p0}^e} \rho_0 \ddot{\boldsymbol{u}}^h \cdot \delta\boldsymbol{u}^h dV + \int_{\Omega_{p0}^e} \boldsymbol{P} : \delta\boldsymbol{F}^h dV \right\}$$

$$+ \sum_{e=1}^{n_{elem}^{p1}} \left\{ \int_{\Omega_{p1}^e} \rho_0 \ddot{\boldsymbol{u}}^h \cdot \delta\boldsymbol{u}^h dV + \int_{\Omega_{p1}^e} (\boldsymbol{P} : \delta\boldsymbol{F}^h dV + \boldsymbol{Q} \vdots \delta\boldsymbol{G}^h) dV \right\}$$

$$+ \sum_{e=1}^{n_{elem}^{p2}} \left\{ \int_{\Omega_{p2}^e} \rho_0 \ddot{\boldsymbol{u}}^h \cdot \delta\boldsymbol{u}^h dV + \int_{\Omega_{p2}^e} (\boldsymbol{P} : \delta\boldsymbol{F}^h dV + \boldsymbol{Q} \vdots \delta\boldsymbol{G}^h + \boldsymbol{U} :: \delta\boldsymbol{H}^h) dV \right\}$$

$$+ \sum_{e=1}^{n_{elem}^{p3}} \left\{ \int_{\Omega_{p3}^e} \rho_0 \ddot{\boldsymbol{u}}^h \cdot \delta\boldsymbol{u}^h dV + \int_{\Omega_{p3}^e} (\boldsymbol{P} : \delta\boldsymbol{F}^h dV + \boldsymbol{Q} \vdots \delta\boldsymbol{G}^h + \boldsymbol{U} :: \delta\boldsymbol{H}^h + \boldsymbol{V} : \vdots \delta\boldsymbol{K}^h) dV \right\}$$

$$= \sum_{i=0}^{3} \sum_{e_i=1}^{n_{elem}^{p_i}} \left\{ \int_{\Omega_{p_i}^{e_i}} \rho_0 \boldsymbol{b} \cdot \delta\boldsymbol{u}^h dV \right\} + \sum_{e_0=1}^{n_{elem}^{p0}} \int_{\partial_t \Omega_{p0}^{e0}} \bar{\boldsymbol{T}} \cdot \delta\boldsymbol{u}^h dS$$

$$(5.3)$$

where $\boldsymbol{b}$ is the body force, the subscript e_i is element ID in the range of $e_i = 1, 2, 3, 4$, the superscript p is the order of process zone in the range of $p = 0, 1, 2, 3$, Ω represents the volume and $\partial_t \Omega$ represents traction boundary of the specific volume Ω.

A superscript "h" is used to denote that the displacement fields with "h" are interpolated displacement fields rather than true displacement fields. Therefore, the discretized displacement field is,

$$\boldsymbol{u}^h(\boldsymbol{X}, t) = \sum_{I_i}^{n_{d_i}} N_{I_i}(\xi) \boldsymbol{d}_{I_i}(t), \qquad i = 0, 1, 2, 3$$

in which, n_{d_i} is the number of total nodes in the element, and $i = 0, 1, 2, 3$ denotes the order of the process zone.

Accordingly, the discretized matrix-form Finite Element dynamic motion equation [66] is shown as,

$$\sum_{i=0}^{3} \sum_{e_i=1}^{n_{e_i}} \sum_{I_i=1}^{n_{d_i}} \int_{V_{e_i}} \left(\boldsymbol{P} \cdot \boldsymbol{B}_{e_i}(\boldsymbol{X}) + \boldsymbol{Q} : \boldsymbol{C}_{e_i}(\boldsymbol{X}) + \boldsymbol{U} \vdots \boldsymbol{D}_{e_i}(\boldsymbol{X}) + \boldsymbol{V} :: \boldsymbol{E}_{e_i}(\boldsymbol{X}) \right) dV \cdot \boldsymbol{d}$$

$$- \sum_{i=0}^{3} \sum_{e_i=1}^{n_{e_i}} \sum_{I_i=1}^{n_{d_i}} \int_{V_{e_i}} \boldsymbol{b} N_{I_i}(\boldsymbol{X}) dV \cdot \boldsymbol{d} - \sum_{e_0=1}^{n_{e_0}} \sum_{I_0=1}^{n_{d_0}} \int_{\partial V_{e_0}} \bar{\boldsymbol{T}} N_{I_0}(\boldsymbol{X}) dS \cdot \boldsymbol{d} \qquad (5.4)$$

$$+ \sum_{i=0}^{3} \sum_{e_i=1}^{n_{e_i}} \sum_{I_i, J_i=1}^{n_{d_i}} \int_{V_{e_i}} \rho_0 N_{I_i}(\boldsymbol{X}) N_{J_i}(\boldsymbol{X}) dV \cdot \ddot{\boldsymbol{d}} = 0$$

in which,

$$\boldsymbol{B}_{e_i}(\boldsymbol{X}) \;\; := \;\; \frac{\partial N_{I_i}}{\partial \boldsymbol{X}}, \qquad \boldsymbol{X} \in \Omega_{e_i} \tag{5.5}$$

$$\boldsymbol{C}_{e_i}(\boldsymbol{X}) \;\; := \;\; \frac{\partial^2 N_{I_i}}{\partial \boldsymbol{X} \otimes \partial \boldsymbol{X}}, \qquad \boldsymbol{X} \in \Omega_{e_i} \tag{5.6}$$

$$\boldsymbol{D}_{e_i}(\boldsymbol{X}) \;\; := \;\; \frac{\partial^3 N_{I_i}}{\partial \boldsymbol{X} \otimes \boldsymbol{X} \otimes \boldsymbol{X}}, \qquad \boldsymbol{X} \in \Omega_{e_i} \tag{5.7}$$

$$\boldsymbol{E}_{e_i}(\boldsymbol{X}) \;\; := \;\; \frac{\partial^4 N_{I_i}}{\partial \boldsymbol{X} \otimes \boldsymbol{X} \otimes \boldsymbol{X} \otimes \boldsymbol{X}}, \qquad \boldsymbol{X} \in \Omega_{e_i} \tag{5.8}$$

and

$$\boldsymbol{d} = \left\{ \boldsymbol{d}_1, \cdots, \boldsymbol{d}_{n_{d_i}} \right\}^T$$

The discretization procedure above is all about space discretization. Dynamics motion problem is involved with temporal discretization and integration in which the Newmark-β algorithm [67] is applied,

$$\boldsymbol{d}_{n+1} = \boldsymbol{d}_n + \boldsymbol{v}_n \Delta t + \frac{1}{2} \boldsymbol{a}_n \Delta t^2 \tag{5.9}$$

$$\boldsymbol{a}_{n+1} = \boldsymbol{M}^{-1}(\boldsymbol{f}_{n+1}^{ext} - \boldsymbol{f}_{n+1}^{int}) \tag{5.10}$$

$$\boldsymbol{v}_{n+1} = \boldsymbol{v}_n + \frac{1}{2}(\boldsymbol{a}_n + \boldsymbol{a}_{n+1})\Delta t \tag{5.11}$$

where the subscript n and $n+1$ indicate to variables at time t_n and t_{n+1}. $\boldsymbol{d}$ is the displacement field, $\boldsymbol{v}$ is the velocity field, and $\boldsymbol{a}$ is the acceleration field and Δt is time increment.

5.2 Quadratic Shape Functions of 2D Hexagon

In [68], the way to construct shape functions of polygon element has been proposed. This section discussed how to construct the quadratic shape functions of 2D hexagon as shown in Fig.5.1.
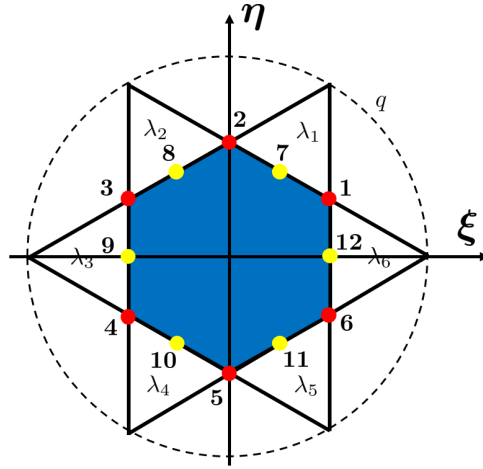
Figure 5.1: Quadratic hexagonal element.

The coordinates of points $1 \sim 12$ are:

$$n_1 = (\frac{\sqrt{3}}{2}, \frac{1}{2}), \quad n_2 = (0, 1)$$

$$n_3 = (-\frac{\sqrt{3}}{2}, \frac{1}{2}), \quad n_4 = (-\frac{\sqrt{3}}{2}, -\frac{1}{2})$$

$$n_5 = (0, 1), \quad n_6 = (\frac{\sqrt{3}}{2}, -\frac{1}{2})$$

$$n_7 = (\frac{\sqrt{3}}{4}, \frac{3}{4}), \quad n_8 = (-\frac{\sqrt{3}}{4}, \frac{3}{4})$$

$$n_9 = (-\frac{\sqrt{3}}{2}, 0), \quad n_{10} = (-\frac{\sqrt{3}}{4}, -\frac{3}{4})$$

$$n_{11} = (\frac{\sqrt{3}}{4}, -\frac{3}{4}), \quad n_{12} = (\frac{\sqrt{3}}{2}, 0)$$

The lines $\lambda_1 \sim \lambda_6$ through nodes are:

$$\lambda_1 : \frac{\xi}{\sqrt{3}} + \eta - 1 = 0, \quad \lambda_2 : \frac{\xi}{\sqrt{3}} - \eta + 1 = 0$$
$$\lambda_3 : \xi + \frac{\sqrt{3}}{2} = 0, \quad \lambda_4 : \frac{\xi}{\sqrt{3}} + \eta + 1 = 0 \tag{5.12}$$
$$\lambda_5 : \frac{\xi}{\sqrt{3}} - \eta - 1 = 0, \quad \lambda_6 : \xi - \frac{\sqrt{3}}{2} = 0$$

The dashed circle q is defined as:

$$\xi^2 + \eta^2 = 3 \tag{5.13}$$

The basis functions $w_1 \sim w_6$ are defined:

$$
\begin{aligned}
w_1 &= \frac{q}{\lambda_2\lambda_3\lambda_4\lambda_5}\Big|_{(\xi=\frac{\sqrt{3}}{2},\eta=\frac{1}{2})}\frac{\lambda_2\lambda_3\lambda_4\lambda_5}{q} \\
&= \frac{1}{\sqrt{3}}\frac{(\frac{\xi}{\sqrt{3}}-\eta+1)(\xi+\frac{\sqrt{3}}{2})(\frac{\xi}{\sqrt{3}}+\eta+1)(\frac{\xi}{\sqrt{3}}-\eta-1)}{\xi^2+\eta^2-3} & (5.14)
\end{aligned}
$$

$$
\begin{aligned}
w_2 &= \frac{q}{\lambda_3\lambda_4\lambda_5\lambda_6}\Big|_{(\xi=0,\eta=1)}\frac{\lambda_3\lambda_4\lambda_5\lambda_6}{q} \\
&= \frac{2}{3}\frac{(\xi+\frac{\sqrt{3}}{2})(-\frac{\xi}{\sqrt{3}}-\eta-1)(\frac{\xi}{\sqrt{3}}-\eta-1)(\xi-\frac{\sqrt{3}}{2})}{\xi^2+\eta^2-3} & (5.15)
\end{aligned}
$$

$$
\begin{aligned}
w_3 &= \frac{q}{\lambda_4\lambda_5\lambda_6\lambda_1}\Big|_{(\xi=-\frac{\sqrt{3}}{2},\eta=\frac{1}{2})}\frac{\lambda_4\lambda_5\lambda_6\lambda_1}{q} \\
&= \frac{1}{\sqrt{3}}\frac{(-\frac{\xi}{\sqrt{3}}-\eta-1)(\frac{\xi}{\sqrt{3}}-\eta-1)(\xi-\frac{\sqrt{3}}{2})(-\frac{\xi}{\sqrt{3}}-\eta+1)}{\xi^2+\eta^2-3} & (5.16)
\end{aligned}
$$

$$
\begin{aligned}
w_4 &= \frac{q}{\lambda_5\lambda_6\lambda_1\lambda_2}\Big|_{(\xi=-\frac{\sqrt{3}}{2},\eta=-\frac{1}{2})}\frac{\lambda_5\lambda_6\lambda_1\lambda_2}{q} \\
&= -\frac{1}{\sqrt{3}}\frac{(\frac{\xi}{\sqrt{3}}-\eta-1)(\xi-\frac{\sqrt{3}}{2})(-\frac{\xi}{\sqrt{3}}-\eta+1)(\frac{\xi}{\sqrt{3}}-\eta+1)}{\xi^2+\eta^2-3} & (5.17)
\end{aligned}
$$

$$
\begin{aligned}
w_5 &= \frac{q}{\lambda_6\lambda_1\lambda_2\lambda_3}\Big|_{(\xi=0,\eta=-1)}\frac{\lambda_6\lambda_1\lambda_2\lambda_3}{q} \\
&= \frac{2}{3}\frac{(\xi-\frac{\sqrt{3}}{2})(-\frac{\xi}{\sqrt{3}}-\eta+1)(\frac{\xi}{\sqrt{3}}-\eta+1)(\xi+\frac{\sqrt{3}}{2})}{\xi^2+\eta^2-3} & (5.18)
\end{aligned}
$$

$$
\begin{aligned}
w_6 &= \frac{q}{\lambda_1\lambda_2\lambda_3\lambda_4}\Big|_{(\xi=\frac{\sqrt{3}}{2},\eta=-\frac{1}{2})}\frac{\lambda_1\lambda_2\lambda_3\lambda_4}{q} \\
&= \frac{1}{\sqrt{3}}\frac{(-\frac{\xi}{\sqrt{3}}-\eta+1)(\frac{\xi}{\sqrt{3}}-\eta+1)(\xi+\frac{\sqrt{3}}{2})(-\frac{\xi}{\sqrt{3}}-\eta-1)}{\xi^2+\eta^2-3} & (5.19)
\end{aligned}
$$

The displacement field $u(\xi,\eta)$ is defined as:

$$
u(\xi,\eta) = \sum_{i=1}^{6}(o_i w_i + d_i w_i w_{i+1}) \tag{5.20}
$$

in which, o_i and d_i are the coefficients of linear and quadratic deformation modes.

The displacement $u(\xi, \eta)$ to be evaluated at 12 nodes in the 2D hexagon as:

$$u_1 = o_1, \quad u_2 = o_2, \quad u_3 = o_3, \quad u_4 = o_4, \quad u_5 = o_5, \quad u_6 = o_6$$

$$u_7 = (w_1)_7 o_1 + (w_2)_7 o_2 + (w_1 w_2)_7 d_1 \Rightarrow d_1 = \frac{u_7 - (w_1)_7 u_1 - (w_2)_7 u_2}{(w_1 w_2)_7}$$

$$u_8 = (w_2)_8 o_2 + (w_3)_8 o_3 + (w_2 w_3)_8 d_2 \Rightarrow d_2 = \frac{u_8 - (w_2)_8 u_2 - (w_3)_8 u_3}{(w_2 w_3)_8}$$

$$u_9 = (w_3)_9 o_3 + (w_4)_9 o_4 + (w_3 w_4)_9 d_3 \Rightarrow d_3 = \frac{u_9 - (w_3)_9 u_3 - (w_4)_9 u_4}{(w_3 w_4)_9}$$

$$u_{10} = (w_4)_{10} o_4 + (w_5)_{10} o_5 + (w_4 w_5)_{10} d_4 \Rightarrow d_4 = \frac{u_{10} - (w_4)_{10} u_4 - (w_5)_{10} u_5}{(w_4 w_5)_{10}}$$

$$u_{11} = (w_5)_{11} o_5 + (w_6)_{11} o_6 + (w_5 w_6)_{11} d_5 \Rightarrow d_5 = \frac{u_{11} - (w_5)_{11} u_5 - (w_6)_{11} u_6}{(w_5 w_6)_{11}}$$

$$u_{12} = (w_1)_{12} o_1 + (w_6)_{12} o_6 + (w_1 w_6)_{12} d_6 \Rightarrow d_6 = \frac{u_{12} - (w_6)_{12} u_6 - (w_1)_{12} u_1}{(w_1 w_6)_{12}}$$

$o_1 \sim o_6$ and $d_1 \sim d_6$ are substituted back Eq.(5.20) and assemble common terms to have:

$$
\begin{aligned}
u(\xi, \eta) = {} & w_1 \left(1 - \frac{w_2}{(w_2)_7} - \frac{w_6}{(w_6)_{12}}\right) u_1 + w_2 \left(1 - \frac{w_1}{(w_1)_7} - \frac{w_3}{(w_3)_8}\right) u_2 \\
& + w_3 \left(1 - \frac{w_2}{(w_2)_8} - \frac{w_4}{(w_4)_9}\right) u_3 + w_4 \left(1 - \frac{w_3}{(w_3)_9} - \frac{w_5}{(w_5)_{10}}\right) u_4 \\
& + w_5 \left(1 - \frac{w_4}{(w_4)_{10}} - \frac{w_6}{(w_6)_{11}}\right) u_5 + w_6 \left(1 - \frac{w_5}{(w_5)_{11}} - \frac{w_1}{(w_1)_{12}}\right) u_6 \\
& + \frac{w_1 w_2}{(w_1 w_2)_7} u_7 + \frac{w_2 w_3}{(w_2 w_3)_8} u_8 + \frac{w_3 w_4}{(w_3 w_4)_9} u_9 \\
& + \frac{w_4 w_5}{(w_4 w_5)_{10}} u_{10} + \frac{w_5 w_6}{(w_5 w_6)_{11}} u_{11} + \frac{w_6 w_1}{(w_6 w_1)_{12}} u_{12}
\end{aligned}
\tag{5.21}
$$

So that the shape functions of 2D quadratic hexagon element are:

$$
\begin{aligned}
& N_1(\xi, \eta) = w_1(1 - 2w_2 - 2w_6); \quad && N_2(\xi, \eta) = w_2(1 - 2w_1 - 2w_3) \\
& N_3(\xi, \eta) = w_3(1 - 2w_2 - 2w_4); \quad && N_4(\xi, \eta) = w_4(1 - 2w_3 - 2w_5) \\
& N_5(\xi, \eta) = w_5(1 - 2w_4 - 2w_6); \quad && N_6(\xi, \eta) = w_6(1 - 2w_5 - 2w_1) \\
& N_7(\xi, \eta) = 4w_1 w_2; \quad N_8(\xi, \eta) = 4w_2 w_3; \quad N_9(\xi, \eta) = 4w_3 w_4; \\
& N_{10}(\xi, \eta) = 4w_4 w_5; \quad N_{11}(\xi, \eta) = 4w_5 w_6; \quad N_{12}(\xi, \eta) = 4w_6 w_1 \ .
\end{aligned}
\tag{5.22}
$$

5.3 Quadratic Elements in MCDD Model

To decrease the yielding stress of MCDD model, the improvement from linear elements to quadratic elements has been made. In the original linear MCDD model, there are five different element types including tetrahedron element, wedge element, square prism element, hexagonal prism element, as shown in Fig.5.2.

Linear element type is short of taking higher order Cauchy-Born rule effects into consideration. It is because that trilinear shape functions of linear elements will become trivial in
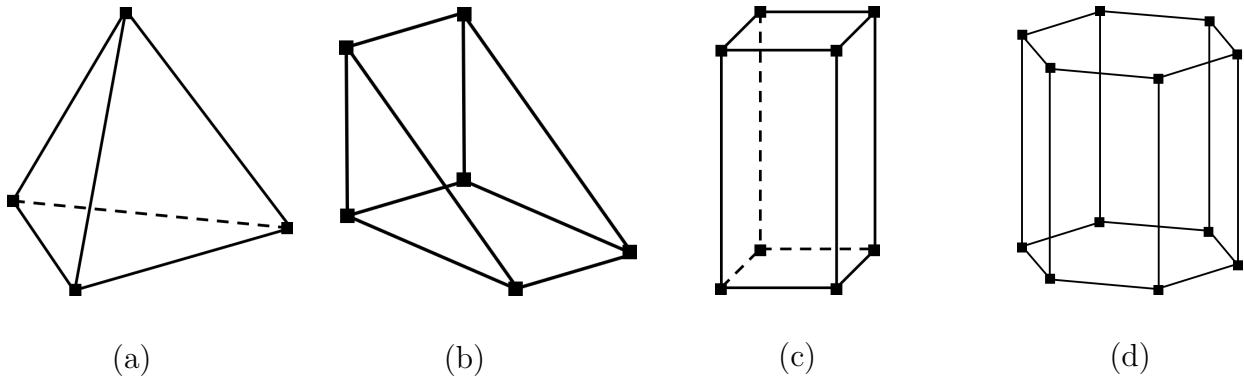
Figure 5.2: Linear elements: (a) tetrahedron element; (b) wedge element; (c) square prism element; (d) hexagonal prism element.
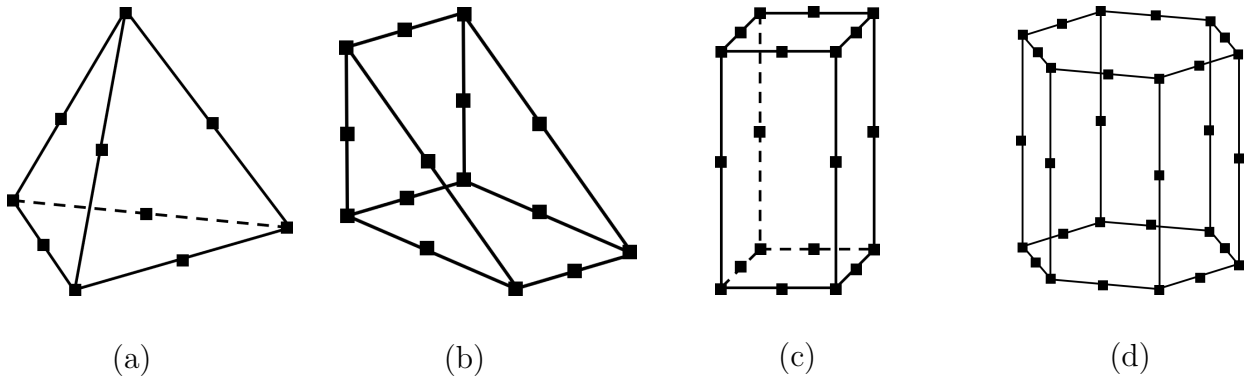
Figure 5.3: Quadratic elements: (a) tetrahedron element; (b) wedge element; (c) square prism element; (d) hexagonal prism element.

higher order derivatives. Therefore, to completely capture higher order Cauchy-Born rule effects quadratic element types are included in present dissertation, as shown in Fig.5.3.

The shape functions of quadratic tetrahedron element, quadratic wedge element and quadratic square prism element have been studied thoroughly in past literature. The shape functions of quadratic hexagonal prism element are based on quadratic 2D hexagonal element discussed in previous section. The detailed shape functions of 3D hexagonal prism element and its first-order derivatives are shown in Appendix.A.

In the following, the quadratic serendipity truncated octahedron element (Fig.5.4(a)) has been studied thoroughly. Floater and Lai [69] proposed a way to use Bernstein polynomial-like functions to form the piecewise defined functions with order d over a polygon with arbitrary number of sides. The corresponding quadratic serendipity element shape functions have Wachspress coordinates ϕ_i and local tetrahedra coordinates $\lambda_{i,j}$. A. Sinu et al has extended the two-dimensional case to three-dimensional case in [70]. In present dissertation, the method of constructing quadratic serendipity element shape functions is applied on 3rd-

order process zone element, i.e. truncated octahedron element.

The first step is to construct Wachspress function ϕ_i. $P \in \mathcal{R}^3$ is defined as the convex truncated octahedron with facets set F and vertices set V as shown in Fig.5.4(a). $h_f(\boldsymbol{x})$ is defined as the perpendicular distance of $\boldsymbol{x}$ to f,

$$h_f(\boldsymbol{x}) = (\boldsymbol{v} - \boldsymbol{x}) \cdot \boldsymbol{n}_f \tag{5.23}$$

in which, $f \in F$ is one facet of the truncated octahedron, $\boldsymbol{n}_f$ is the unit outward normal vector, $\boldsymbol{x}$ is an arbitrary point within P and $\boldsymbol{v}$ is one vertex of the truncated octahedron. Based on coboundary operator of cell complexes in Chapter 2, the three facets sharing one vertex $\boldsymbol{v}$ can be defined as f_1, f_2, f_3. Therefore, the shape function $\phi_{\boldsymbol{v}}(\boldsymbol{x})$ is given as,

$$\phi_{\boldsymbol{v}}(\boldsymbol{x}) = \frac{w_{\boldsymbol{v}}(\boldsymbol{x})}{\sum_{\boldsymbol{u} \in V} w_{\boldsymbol{u}}(\boldsymbol{x})} \tag{5.24}$$

in which,

$$w_{\boldsymbol{v}}(\boldsymbol{x}) = \begin{vmatrix} \boldsymbol{p}_{f_1,1} & \boldsymbol{p}_{f_1,2} & \boldsymbol{p}_{f_1,3} \\ \boldsymbol{p}_{f_2,1} & \boldsymbol{p}_{f_2,2} & \boldsymbol{p}_{f_2,3} \\ \boldsymbol{p}_{f_3,1} & \boldsymbol{p}_{f_3,2} & \boldsymbol{p}_{f_3,3} \end{vmatrix} \tag{5.25}$$

and $\boldsymbol{p}_f := \boldsymbol{n}_f / h_f(\boldsymbol{x})$ as shown in Fig.5.4(b).

The second step is to have tetrahedra coordinates as shown in Fig.5.4(c)-(d). Fig.5.4(c) shows $\lambda_{i,1}$ and Fig.5.4(d) shows $\lambda_{i+1,1}$. The tetrahedra coordinate $\lambda_{i,j}$ is denoted as:

$$\lambda_{i,j}(\boldsymbol{x}) = \frac{d_{i,j}(\boldsymbol{x})}{\Delta_i}, \qquad j \in (1, 2, 3, 4), \tag{5.26}$$

in which

$$d_{i,j}(\boldsymbol{x}) = \begin{vmatrix} 1 & x & y & z \\ 1 & x_k & y_k & z_k \\ 1 & x_l & y_l & z_l \\ 1 & x_m & y_m & z_m \end{vmatrix}, \qquad (j, k, l, m) \in (1, 2, 3, 4), \tag{5.27}$$

$$\Delta_i = \begin{vmatrix} 1 & x_i & y_i & z_i \\ 1 & x_{i+1} & y_{i+1} & z_{i+1} \\ 1 & x_{i+2} & y_{i+2} & z_{i+2} \\ 1 & x_{i+3} & y_{i_3} & z_{i+3} \end{vmatrix} \tag{5.28}$$

Therefore, the shape functions of quadratic serendipity element associated with the vertex node, i and the midside node $(i, 1)$ (between i and $i + 1$) are given as,

$$\psi_i = F_i - \frac{1}{2} \sum_{j=1}^{3} F^j \tag{5.29}$$

$$\psi_{i,1} = 2F_{i,1} \tag{5.30}$$

(a)

(b)

(c)

(d)

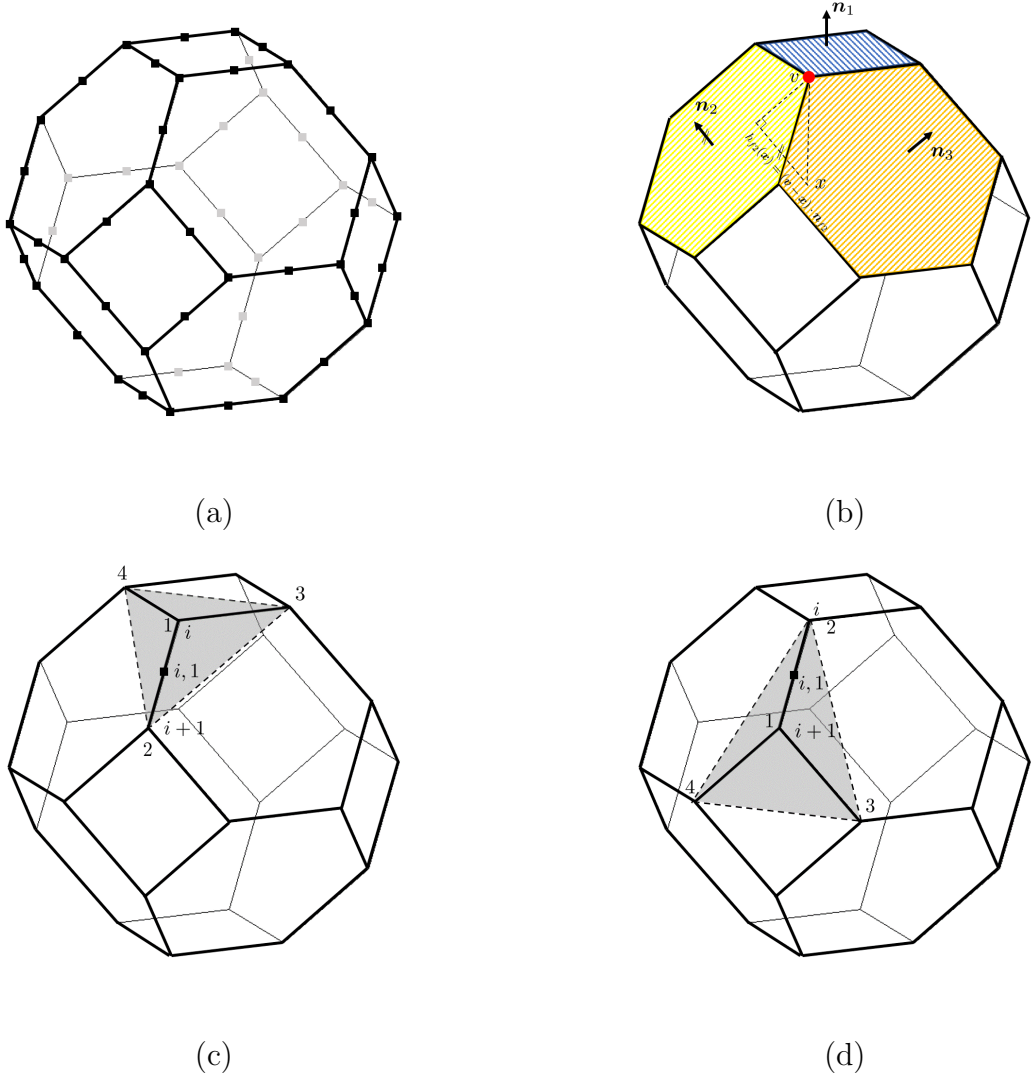Figure 5.4: Serendipity shape function: (a) quadratic truncated octahedron element; (b) wachspress interpolants; (c) 3D local tetrahedron coordinate $\lambda_{i,1}$: tetrahedron coordinate of the point for vertex 1 corresponding to vertex i of the convex polyhedral; (d) 3D local tetrahedron coordinate $\lambda_{i+1,1}$: tetrahedron coordinate of the point for vertex 1 corresponding to vertex $i+1$ of the convex polyhedral.

in which, ψ_i and $\psi_{i,1}$ are the shape functions of the vertex i and the middle node $(i,1)$. F^j denotes the $F_{i,1}$ of three edges incident to vertex i.
F_i and $F_{i,1}$ are defined as

$$F_i = \phi_i \lambda_{i,1} \tag{5.31}$$
$$F_{i,1} = \phi_i \lambda_{i,2} + \phi_{i+1} \lambda_{i+1,2} \tag{5.32}$$

where ϕ_i is the Wachspress coordinate of vertex i; $\lambda_{i,1}$ and $\lambda_{i,2}$ are the tetrahedra volume coordinates corresponding to vertex 1 and 2 associated with the vertex i. It is found that the shape functions of quadratic serendipity truncated octahedron element satisfies following constant, linear and quadratic patch tests:

$$\sum_{i=1}^{n_v} \psi_i + \sum_{i=1}^{n_m} \psi_{i,1} = 1, \tag{5.33}$$

$$\sum_{i=1}^{n_v} \psi_i \boldsymbol{x}_i + \sum_{i=1}^{n_m} \psi_{i,1} \boldsymbol{x}_{i,1} = \boldsymbol{x}, \tag{5.34}$$

$$\sum_{i=1}^{n_v} \psi_i \boldsymbol{x}_i \otimes \boldsymbol{x}_i + \sum_{i=1}^{n_m} \psi_{i,1} \boldsymbol{x}_{i,1} \otimes \boldsymbol{x}_{i,1} = \boldsymbol{x} \otimes \boldsymbol{x} . \tag{5.35}$$

in which, numbers of vertices and middle nodes along edges of elements are denoted by n_v and n_m; the space coordinate of vertex node i is denoted as $\boldsymbol{x}_i$ and the space coordinate of middle node $(i,1)$ is denoted as $\boldsymbol{x}_{i,1}$; the space coordinate of arbitrary position where the shape functions are evaluated is denoted as $\boldsymbol{x}$.
In the next, a simple compression test is conducted to show the effectiveness of higher order shape functions considered in MCDD model. The MCDD model is shown as Fig.5.5(a). The initial aspect ratio is 1:2:4, with dimension $420\mathring{A} \times 840\mathring{A} \times 1680\mathring{A}$. The upper 10% portion of model is velocity-prescribed corresponding to three different strain rate: $1.1 \times 10^7 s^{-1}$, $5.55 \times 10^7 s^{-1}$ and $2.77 \times 10^8 s^{-1}$. The MCDD results are compared with Molecular Dynamics simulation results as Fig.5.5(b).
Fig.5.5(b) has totally 4 sets of curves, including perfect crystal MD simulation, preexisted voids crystal MD simulation, preexisted dislocations crystal MD simulation and MCDD simulation. Each set will have three different loading velocities: $1.11 \times 10^7 s^{-1}$, $5.55 \times 10^7 s^{-1}$ and $2.77 \times 10^8 s^{-1}$. The corresponding curves are marked by different line types: solid line, dash line and dotted line. The labels "∗1" denotes velocity is $1.1 \times 10^7 s^{-1} \times 1$, "∗5" denotes velocity is $1.1 \times 10^7 s^{-1} \times 5$ and "∗25" denotes velocity is $1.1 \times 10^7 s^{-1} \times 25$.
From stress-strian curves comparison in Fig.5.5(b), it is found that applying quadratic element MCDD model can so greatly decrease the yielding stress that the MCDD model with perfect dual lattice mesh can have equivalent yielding stress as crystal MD model with pre-existed voids. It denotes that higher order process zones with higher order Cauchy-Born rule and higher order shape functions represent preexisted crystal defects such as cracks, voids, dislocation and etc. The conclusion is consistent with previous comments on Geometrically Compatible Dislocation Pattern in Chapter 3.
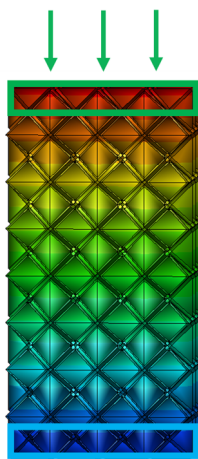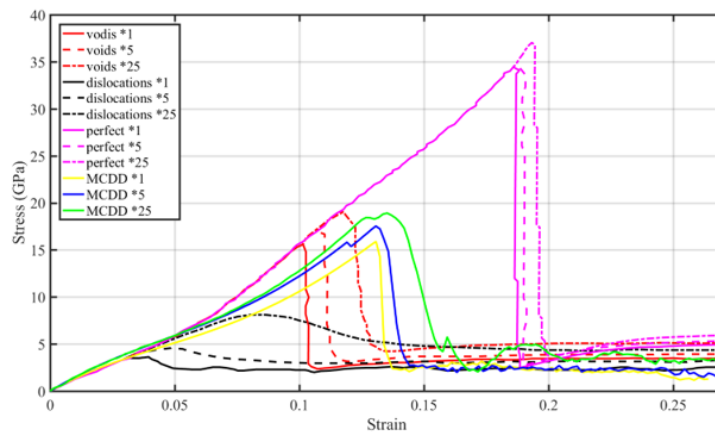
(a) (b)

Figure 5.5: Benchmark test of quadratic element MCDD model: (a) MCDD model; (b) stress-strain curves comparison with Molecular Dynamics simulation.

Chapter 6

Numerical Simulations
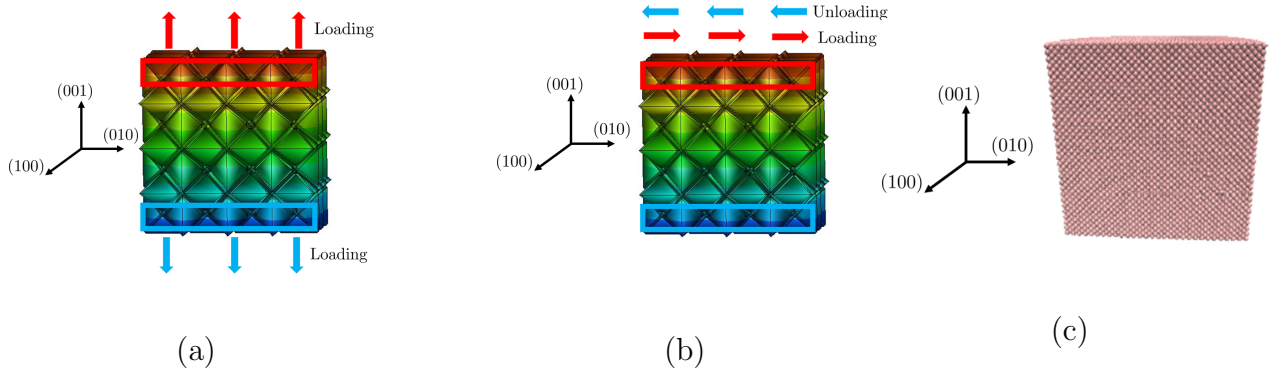
Figure 6.1: MCDD modeling of a BCC crystal under: (a) uniaxial tension loading, (b) pure shear loading and unloading and (c) MD model

6.1 Uniaxial Tension and Pure Shear

In this section, we first present MCDD numerical results in uniaxial tension test and pure shear test to show the validity of temperature-related MCDD method in stress-strain relation calculation. To model and simulate crystal plasticity in α-phase tantalum crystal, we adopt the higher order Cauchy-Born rule that utilizes the Embedded-Atom method potential discussed in [61].

The total Helmholtz free energy $\mathcal{F}_H$ of the crystal solid can be written as,

$$\mathcal{F}_H = \frac{1}{2}\sum_{i\neq j}\phi(r_{ij}) + \sum_i F_i(\bar{\rho}_i) + k_B T \sum_i \sum_k \ln\left[2\sinh\frac{\hbar w_{ik}}{2k_B T}\right],\qquad(6.1)$$

where $\phi(r_{ij})$ represents the pair energy between atoms i and j separated by a distance r_{ij}, and F_i is the embedding energy associated with embedding an atom i into a local site with

an electron density $\bar{\rho}_i$, which is defined as,

$$\bar{\rho}_i = \sum_{i \neq j} \rho_j(r_{ij}) \tag{6.2}$$

with $\rho_j(r_{ij})$ as the electron density at the site of atom i arising from atom j at a distance r_{ij} away.

(a)   (b)
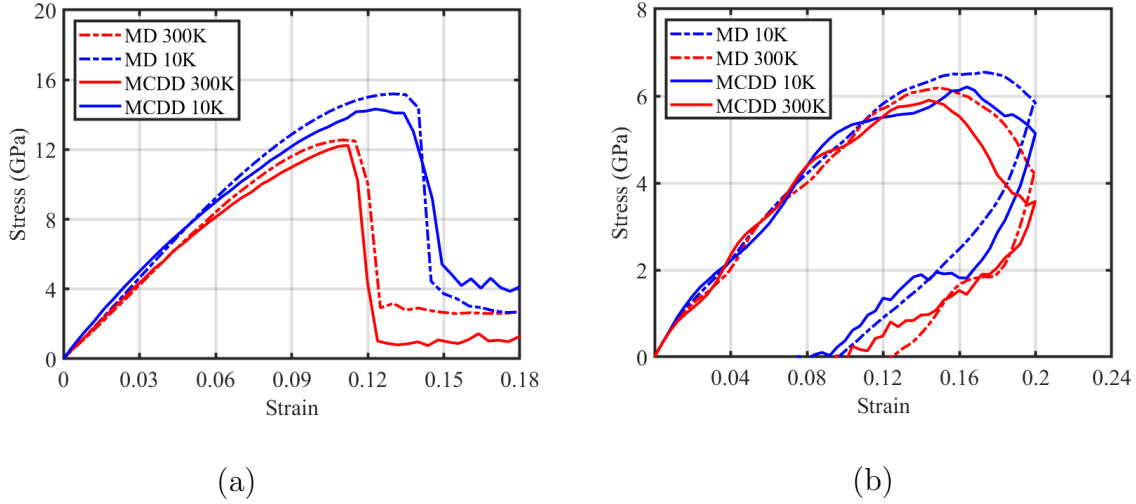
Figure 6.2: The stress-strain curves comparison between MD and MCDD at low and high temperature: (a) uniaxial tension loading and (b) pure shear loading and unloading

We use the following pair potential $\phi(r)$ for α-Ta,

$$\phi(r) = \frac{A \exp\left[-\alpha(\frac{r}{r_e} - 1)\right]}{1 + (\frac{r}{r_e} - \kappa)^{20}} - \frac{B \exp\left[-\beta(\frac{r}{r_e} - 1)\right]}{1 + (\frac{r}{r_e} - \lambda)^{20}}, \tag{6.3}$$

where r_e is the equilibrium spacing between nearest neighbors, A,B,α and β are four adjustable parameters, and κ and λ are two additional parameters for the cutoff. The electron density $\rho(r)$ is defined as,

$$\rho(r) = \frac{f_e \exp\left[-\beta(\frac{r}{r_e} - 1)\right]}{1 + (\frac{r}{r_e} - \lambda)^{20}} . \tag{6.4}$$

The embedding energy function is expressed as follows,

$$F(\rho) = \sum_{i=0}^{3} F_{ni}\left(\frac{\rho}{\rho_n} - 1\right)^i, \quad \rho < \rho_n, \quad \rho_n = 0.85\rho_e$$

$$F(\rho) = \sum_{i=0}^{3} F_i\left(\frac{\rho}{\rho_e} - 1\right)^i, \quad \rho_n \leq \rho < \rho_0, \quad \rho_0 = 1.15\rho_e \qquad (6.5)$$

$$F(\rho) = F_e\left[1 - \ln\left(\frac{\rho}{\rho_s}\right)^\eta\right]\left(\frac{\rho}{\rho_s}\right)^\eta, \quad \rho_0 \leq \rho$$

The value of parameters used for α-phase Tantalum are taken from [61] and are shown in Table.6.1. Based on the EAM formulation i.e. Eq.(4.5), we can calculate elastic tensor of Tantalum under different temperature as shown in Fig.4.1.

Table 6.1: Parameters in the formulations of EAM potential for α-Ta

Parameter	Value	Parameter	Value
$r_e[\overset{\circ}{A}]$	2.860082	$F_{n1}[eV]$	-0.405524
f_e	3.086341	$F_{n2}[eV]$	1.112997
ρ_e	33.787168	$F_{n3}[eV]$	-3.585325
ρ_s	33.787168	$F_0[eV]$	-5.14
α	8.489528	$F_1[eV]$	0
$A[eV]$	0.611679	$F_2[eV]$	1.640098
$B[eV]$	1.032101	$F_3[eV]$	0.221375
κ	0.176977	η	0.848843
λ	0.353954	$F_e[eV]$	-5.141526
$F_{n0}[eV]$	-5.103845	β	4.527748

The MCDD model with the size of $100\overset{\circ}{A} \times 100\overset{\circ}{A} \times 100\overset{\circ}{A}$ is shown as in Fig.6.1(a). In this example, there are 576 tetrahedron elements, 1008 wedge elements, 154 prism elements (including 88 hexagonal prism elements and 66 square prism elements) and 15 truncated octahedron elements. We firstly apply the prescribed displacement/velocity loading condition on MCDD specimen under prescribed loading strain rate with $0.25\ ps^{-1}$. The boundary conditions for MCDD simulations are as follows: The upper and lower 10% portion of the specimen are applied with the prescribed displacement/velocity with opposite direction. The rest of the boundaries are traction and higher order traction free (see [39]).

Meanwhile, the molecular dynamics simulation is conducted by using the molecular dynamics simulation software package LAMMPS, and the MD model or specimen has 59582 atoms,

which is shown as Fig.6.1(c). The atomic pair potential for α-Ta is based on the reference [61]. The same strain rate used in MCDD calculations is applied in MD simulations.

By calculating uniaxial temperature-related stress-strain curves mentioned above, we have obtained the corresponding constitutive relations in MCDD simulations at low/high temperature. The obtained stress-strain curves are compared with those of MD simulations as shown in Fig.6.2(a), respectively. From Fig.6.2(a), one may find that in different temperature-related cases the stress-strain relations obtained from MCDD simulations and from MD simulations are consistent, which indicates the MCDD method is valid in simulating nanoscale crystal plasticity for single α-Ta crystal at different temperature.

By considering higher order Cauchy-Born rule based higher order strain gradient formulations on wedge shaped dislocation patterns, prism shaped dislocation patterns, and truncated octahedron dislocation patterns, the MCDD method shows its ability to capture inelastic behavior and the path-dependent constitutive relation of α-phase tantalum in single crystal plasticity simulation. Moreover, the above MCDD simulation has much higher computational efficiency in comparison with the MD model or specimen with the same size and boundary and loading conditions.

Similar to the pure tension case, we also conducted a pure shear test on an α-Ta specimen of $100\overset{\circ}{A} \times 100\overset{\circ}{A} \times 100\overset{\circ}{A}$. The setup of the MCDD simulation and α-phase tantalum model are shown as Fig.6.1(b). The displacement/velocity boundary conditions under prescribed pure shear deformation are slightly different from the uniaxial loading one: for the uniaxial loading the upper and lower portion are prescribed with velocity while for the pure shear loading the upper portion is velocity-prescribed but the lower portion is fix. For the MD simulation, the boundary condition on x,y and z directions are respectively p,s and s in which p represents periodic and s represents non-periodic, shrink-wrapped.

Based on the results presented above, we may conclude that under pure shear loading MCDD method also offers consistent results with that obtained from MD simulations.

6.2   Orientation Effects of Tantalum Crystal at Grain Scale

Based on classical crystal plasticity theory, the critical resolved shear stress (CRSS) is the key to govern the dislocation sliding in single crystal. Therefore, scholars established the Schmid law to relate the critical resolved shear stress (CRSS) to the crystal lattice orientation. However, the Schmid law is a phenomenological equation based on empirical theory and NOT valid when it is concerned with BCC crystal lattice structure. We call the violation of Schmid law in BCC crystal structure as the non-Schmid law.

To prove that the MCDD dislocation pattern dynamics is able to predict crystal orientation effects at nanoscale, the 28 crystallographic (loading) orientations are applied on Tantalum crystal under tension and compression (see:Fig.6.3). The way we rotate crystal lattice is shown in Appendix B. The prescribed displacement/velocity boundary condition is: a con-
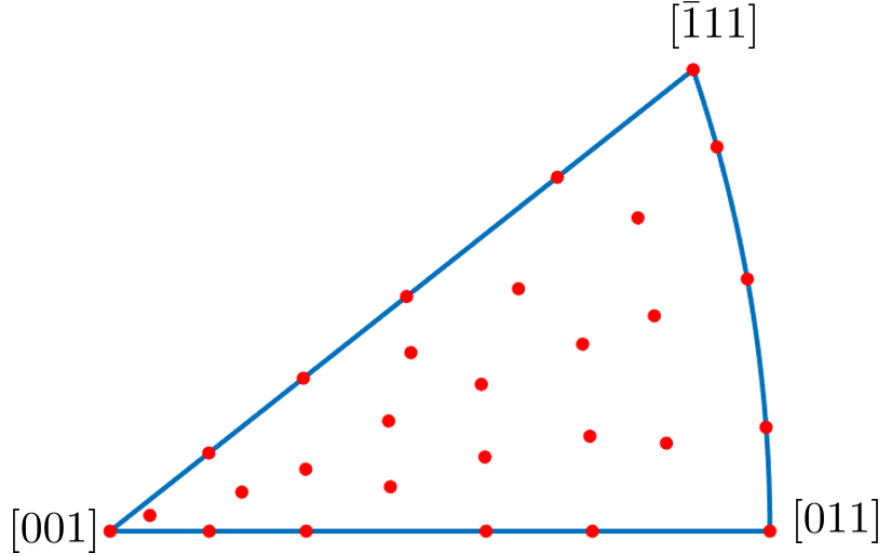
Figure 6.3: Stereographic triangle has red nodes indicating 28 different crystallographic orientations in which the uniaxial loading is applied on the single crystal deformation simulation

stant strain rate of 10^9/s is applied on the upper and lower 10% portion of MCDD models in each loading direction. The specimen size is $16nm \times 16nm \times 16nm$. To prove validity of the MCDD method, we also construct MD model with the same conditions including sample size, loading boundary condition as comparison.

The molecular dynamics (MD) results at $300K^o$ are shown in Figure 6.4(a). From the figure, we can find that asymmetry of tension/compression yielding stress contour with different crystal lattice orientation in the stereographic triangle at $300K^o$. Fig.6.4(b) displays results of the MCDD simulation of different crystal lattice orientation at $300K^o$. By comparing these two figures, we can conclude that the MCDD method, as an atomistic-informed crystal plasticity model, can reproduce basically the same results obtained by using molecular dynamics method.

6.3   Non-Schmid Effect in α-Ta

The Schmid Law establishes the relation among the critically resolved shear stress, slip plane and slip direction, and applied stress. The threshold of a critically resolved shear stress is the shear strength of the crystalline material on a given slip plane and along a given glide direction. The formulation that describes Schmid's law is expressed as,

$$\tau = \sigma cos(\lambda)cos(\phi) \tag{6.6}$$

where τ is the critical resolved shear stress or the yield stress on a given slip plane. λ represents the angle between loading direction and slip direction and ϕ represents the angle
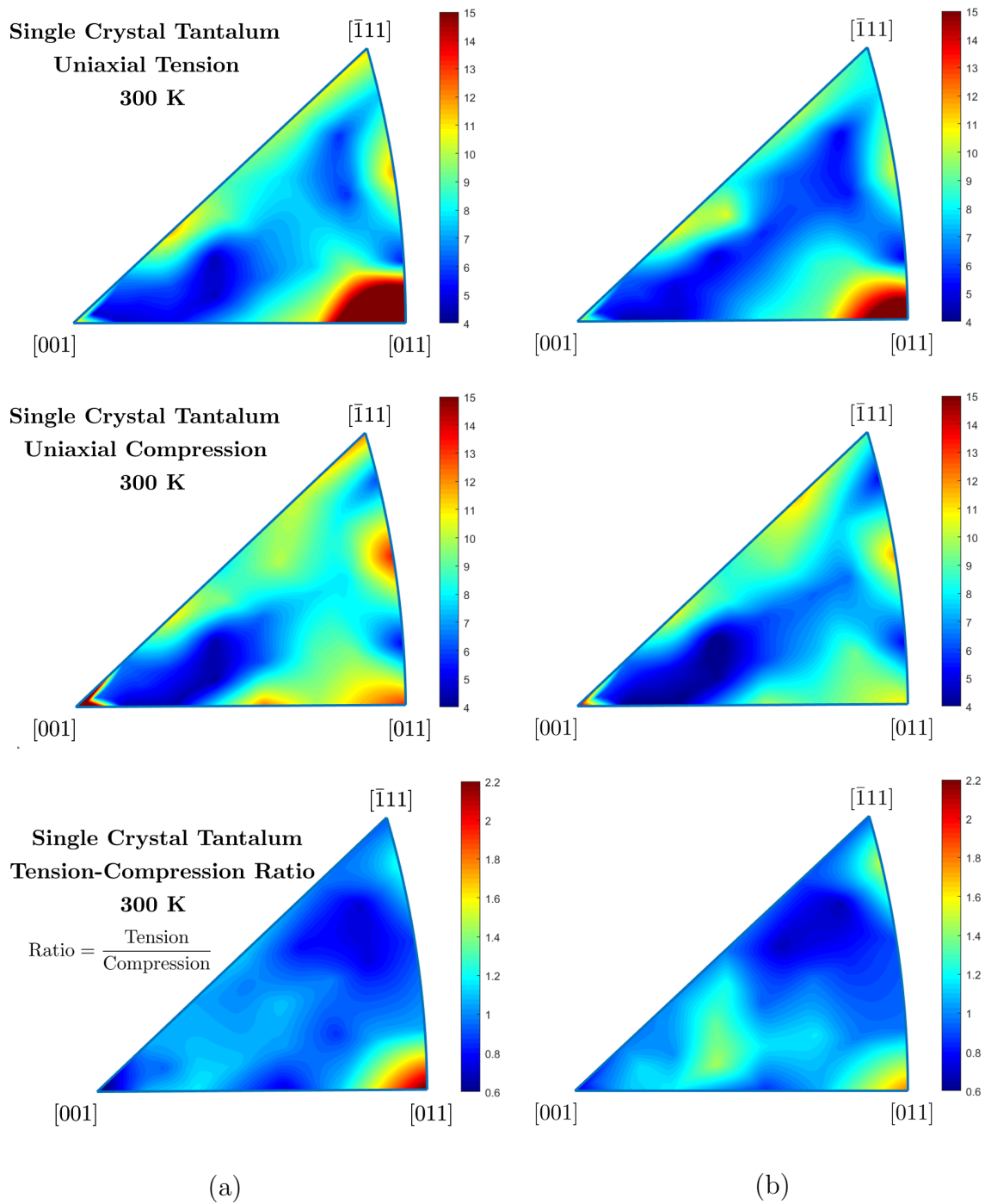
Figure 6.4: Stress and stress ratio contour figures: (a) MD results at 300K; (b) MCDD results at 300K

between loading direction and normal direction of slip plane, as illustrated in Fig. 6.5(a).

(a)

(b)
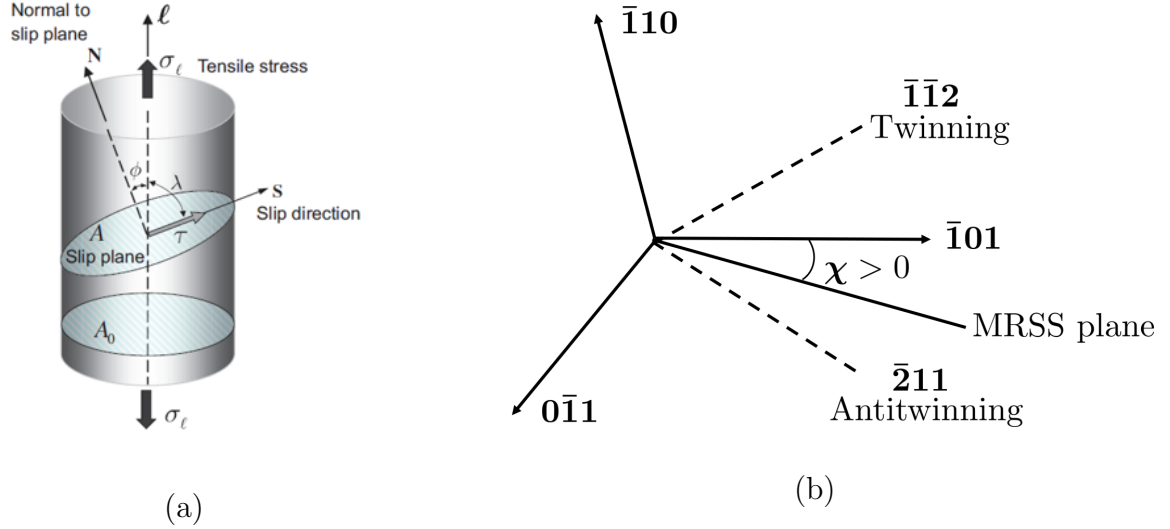
Figure 6.5: (a) Illustration of Schmid Law[11] and (b) Definition of χ describing the orientation of the MRSSP relative to the ($\bar{1}01$) plane[12].

The Schmid law allows phenomenological crystal plasticity to obtain mechanical characteristics of crystal plastic deformation especially for closed-packed crystal structures, e.g. FCC crystal. However, for those crystals that are not closed-packed crystal structure, violation of Schmid law is due to spreading of dislocation to non-parallel planes and we have dependence of shear stress on orientation of Maximum Resolved Shear Stress Plane(MRSSP)[12].
Vitek and his co-workers have employed molecular dynamics to simulate the Non-Schmid effect of Tantalum [12]. In molecular dynamics modeling, Moriarty et al. [71] measured the angle χ with respect to the ($\bar{1}01$) plane as shown in Fig. 6.5(b). The sign of χ is also shown and the range of it is between $-30^o \leq \chi \leq 30^o$ considering the crystal symmetry. And the twinning-antitwinning asymmetry of shear can be reflected on {112} plane because the shear in [111] direction is equivalent to the shear in the [$\bar{1}\bar{1}\bar{1}$] direction for the orientation $-\chi$ but shears are not equivalent along [111] and [$\bar{1}\bar{1}\bar{1}$].
In this numerical example, we construct a $20nm \times 20nm \times 20nm$ MCDD model with 576 tetrahedron elements(0th-order), 1008 wedge elements(1st-order), 154 prism elements(2nd-order), 15 truncated octahedron elements(3rd-order), as illustrated in Fig 6.6(a). The lower 10% portion is fixed while the upper 10% portion is applied with prescribed displacement.
The regular orientation is: (100) along x-axis, (010) along y-axis and (001) along z-axis. The way we rotate the regular orientation to the new orientation: ($\bar{1}01$) along x-axis, ($1\bar{2}1$) along y-axis and (111) along z-axis is based on Appendix. B.
For α-Ta, we used the EAM potential developed by Zhou et al in [61] to construct multiscale constitutive relation.

(a)

(b)
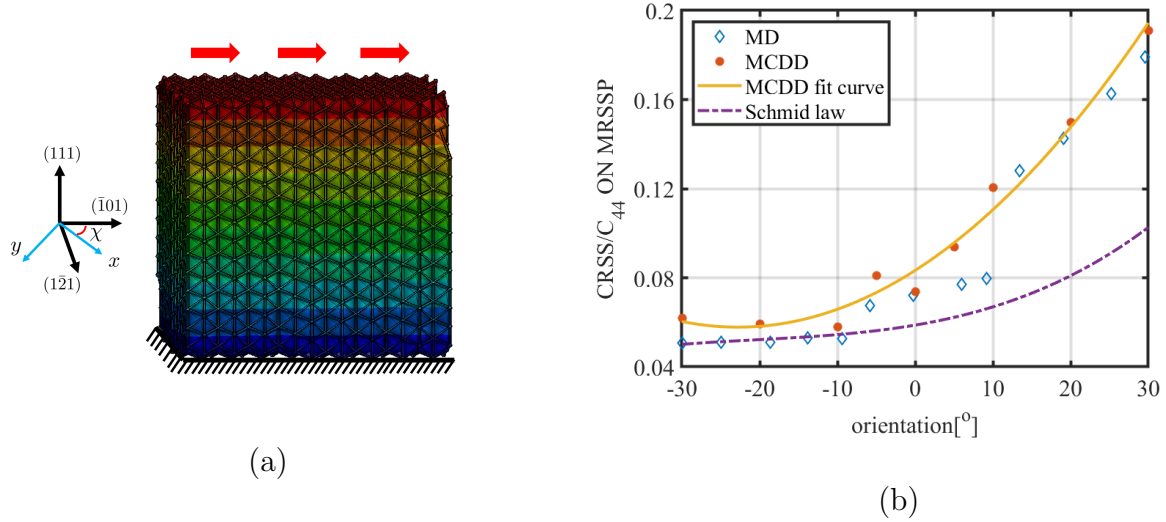
Figure 6.6: (a) MCDD model with $\chi = 0^o$ and (b) Non-Schmid curve in α-Ta.

In this case, we regard the shear yield stress as the maximum resolved shear stress. From the Fig.6.6(b), one may find that with increasing angle χ the critical resolved shear stress increases. We compare MCDD results with MD simulation in [12] as illustrated in Fig 6.6(b). From this figure, we can find that MCDD results have a very good consistency with MD model but less computational costs. Therefore, we conclude that MCDD simulation can predict the non-Schmid effect in Tantalum single crystal, and it thus provides a validation for the method.

6.4 Size Effect of Crystal Plasticity in Micron-scale α-Ta Pillar

At nanos- and sub-micron scale, a very strong size effect of crystal plasticity has been reported in experiments, e.g.[72]. In the following, we report a preliminary study on size-effect of mesoscale crystal plasticity observed in MCDD simulations of an uniaxial test of α-Ta single crystal.

We conduct the uniaxial tension on micron-scale size α-Ta pillars that have following dimensions: $1.0\mu m \times 1.0\mu m \times 1.0\mu m$, $1.25\mu m \times 1.25\mu m \times 1.25\mu m$, $1.5\mu m \times 1.5\mu m \times 1.5\mu m$, $1.75\mu m \times 1.75\mu m \times 1.75\mu m$ and $2.5\mu m \times 2.5\mu m \times 2.5\mu m$ (see Fig.6.7). The upper and lower 10% portion are prescribed with displacement/velocity boundary conditions with opposite directions. The loading strain rate is kept as $2 \times 10^7 s^{-1}$. The strain-strain relations with specimens of different sizes are shown in Fig.6.8.

From the Fig.6.8, we can clearly see that the increase of numerical specimen size will lead to a decrease in yielding stress in significant manner. Furthermore, the flow stress of different
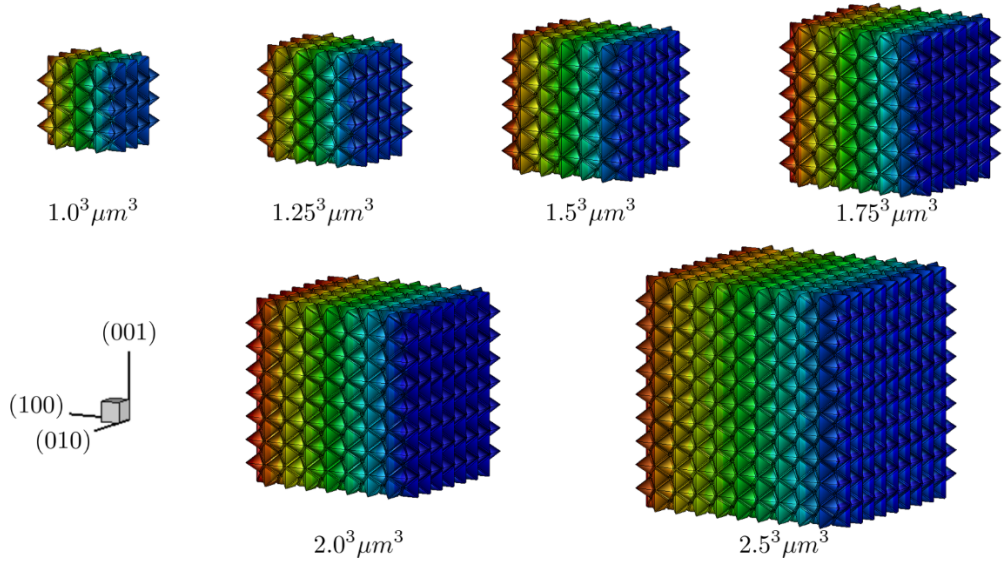
Figure 6.7: MCDD finite element models with different sizes: (a) $1.00\mu m^3$; (b) $1.25\mu m^3$; (c) $1.50\mu m^3$; (d) $1.75\mu m^3$; (e) $2.0\mu m^3$ and (d) $2.50\mu m^3$.
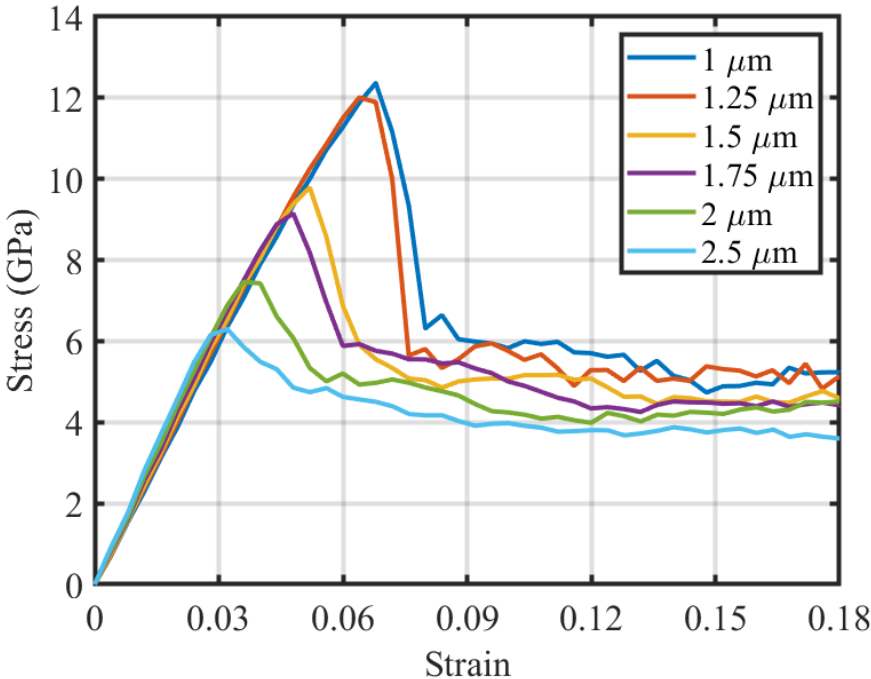
Figure 6.8: Stress-strain curves comparison of micron-scale size MCDD models.

size models are also decreasing corresponding to the increase of the size of the specimen. Therefore, we can conclude that the MCDD crystal plasticity modeling method is able to simulate and predict the size effect of crystal plasticity at micron scale. Even though, the yield stress of $2.50\mu m^3$ α-Ta pillar is still very higher, but it is significantly lower than all the molecular dynamics predictions reported in literature, which is usually $> 10GP_a$, and hence this is the closest yield stress prediction to the experimental result. With the further reduce of loading strain rate and increase of the size of specimen, we expect to fill the gap between the modeling prediction and experimental observation in near future. To author's knowledge, it is the first time that anyone captures the size effect of crystal plasticity in the micon-scale, where the molecular dynamics may require hundreds or even thousands times of computation cost than that of the MCDD crystal plasticity method.
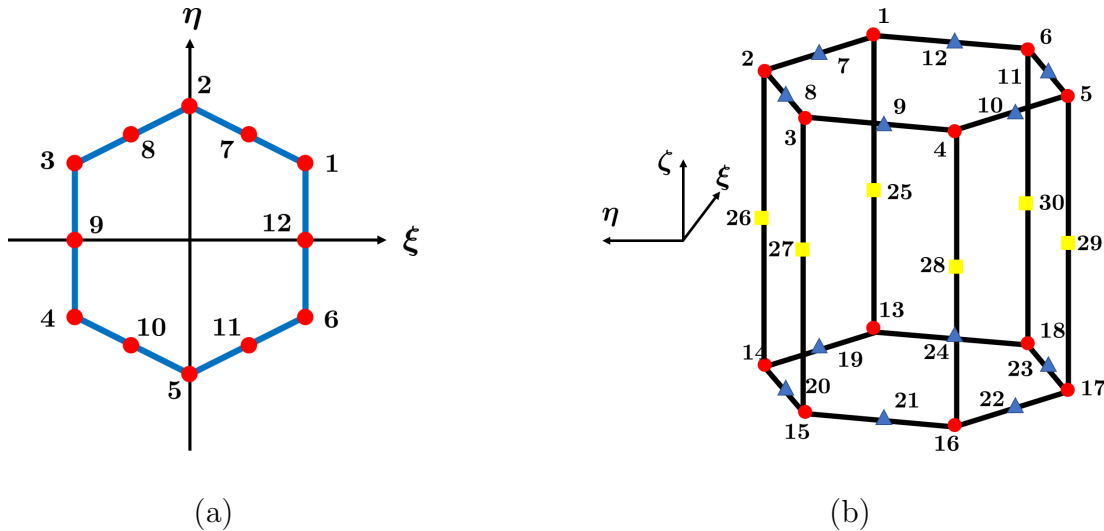
Figure 6.9: Isoparameteric quadratic element illustration: (a) 2D quadratic hexagonal element and (b) 3D quadratic hexagonal prism element

6.5   Dislocation Substructures under Different Temperatures

The BCC α-Ta metal is well-known to exhibit strong temperature effect on crystal plasticity. In particular, it has very different dislocation substructures under low temperature $< 70K^o$ and under high temperature $> 450k^o$ e.g. [3, 40]. Under the low temperature, one finds long screw dislocations in approximately homogeneous distribution, whereas at high temperatures, one may find cellular dislocation patterns.

In this example, we applied the proposed finite temperature atomistically informed crystal plasticity to exam how temperature may affect the dislocation substructure morphology or dislocation pattern.

In this example, the super dual lattice structure specimens are created in two different dimensions: $L_x \times L_y \times L_z = 84nm \times 84nm \times 168nm$, $168nm \times 168nm \times 336nm$ as shown in Fig.6.10. Aiming for a qualitative study, we conducted the numerical simulation at both low temperature $(20K^o)$ and high temperature $(500K^o)$ to see if different dislocation patterns will be activated at different temperatures. In the MCDD specimen used, it has 11008
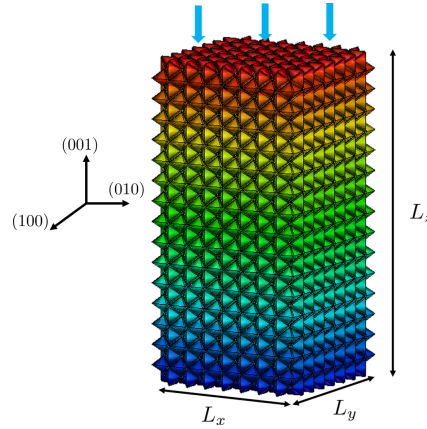
Figure 6.10: Cross-slip simulation in super dual lattice model

tetrahedron elements (bulk crystal elements), 20864 wedge elements(1st order process zone or wedge dislocation pattern elements), 1776 prism elements(2nd order process zone or prism dislocation pattern elements), and 209 truncated octahedron elements (the 3rd process zone or truncated octahedron dislocation pattern elements). We conducted uniaxial compression tests with prescribed dispacement/velocity boundary condition with loading strain rate: $6 \times 10^{-5}ps^{-1}$.

To capture the slip plane formation during crystal pillar deformation, we employ quadratic Lagrangian element-wise shape function to model the slip plane deformation. The wedge base functions are applied to construct quadratic hexagonal prism element as shown in Fig.6.9.

Figure 6.9(a) displays the plane quadratic hexagonal element. The corresponding shape functions are constructed based on the Wedge Base Function method [68]. The first derivative of 3D hexagonal prism element shape functions are documented in Appendix A.

To analyze the results of the low temperature uniaxial compression test, we display all the triangle plate elements with large plastic strain in Fig.6.11(a) in a deformation loading sequence. One may find that at small deformation, a clear primary slip plane (011) (or slip plate) appears first, which suggests that there exist long screw dislocation groups on a localized primary slip plane, which may come from one side of the specimen surface to other facets of the specimen surface. As the deformation load increase, from Fig.6.11(a) one may find the dislocation cross-slip from the primary (011) plane or plate to the secondary ($\bar{1}01$) slip plane or plate.

Figure 6.11 and Figure 6.12 display the dislocation pattern formation sequence corresponding to different loading deformation phases. From Fig.6.11(a), we can find that with crystal
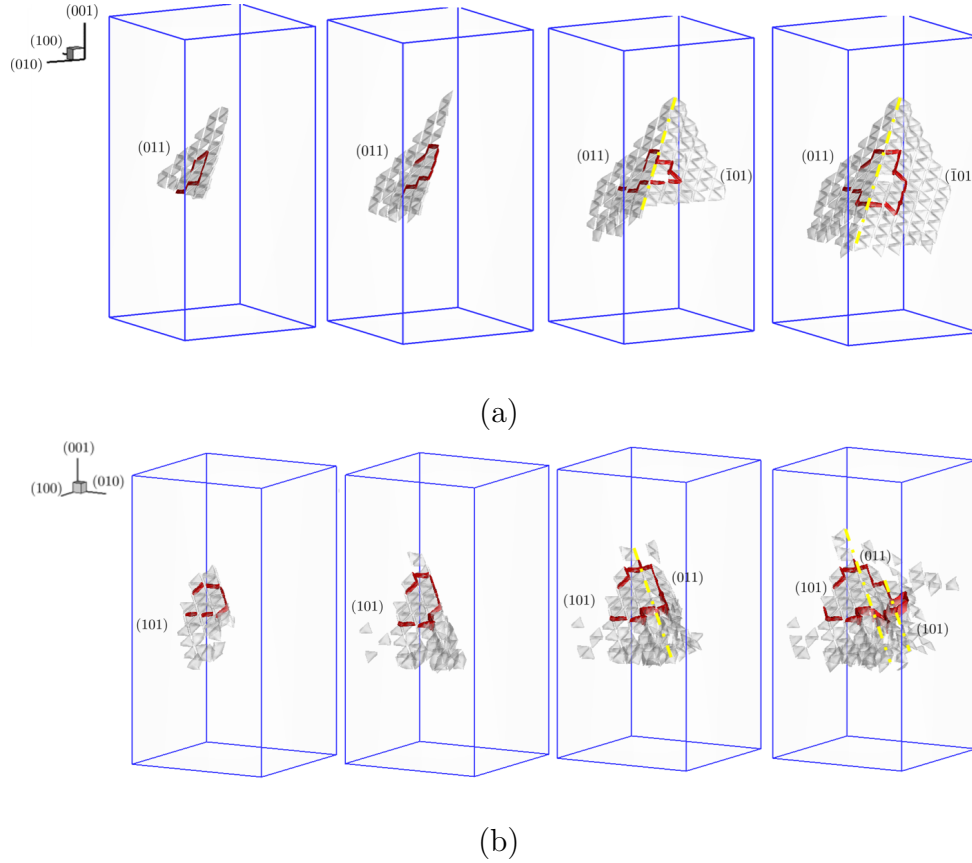
Figure 6.11: (a): $84nm \times 84nm \times 168nm$ model size at temperature $20K$; (b): $168nm \times 168nm \times 336nm$ model size at temperature $20K$. The grey planes(slip planes) are formed by wedge process zone elements, the red lines are formed by prism process zone elements, the yellow dash lines represent shared common edges by primary slip plane and the secondary slip planes.

deformation the primary slip plane (011) in $84nm \times 84nm \times 168nm$ size model will appear first, then increasing element strain will activate the secondary slip plane ($\bar{1}01$) at $20K$. Besides the accumulated dislocations will activate prism elements and even allow prism elements "jump" from primary slip plane to the secondary slip plane. One of the mechanisms of the cross-slip in α-Ta is that the screw dislocations with the Burgers vectors $[111](\bar{1}01)$ and $[1\bar{1}\bar{1}](101)$ move downwards, and the screw dislocations with the Burgers vectors $[\bar{1}\bar{1}\bar{1}](\bar{1}01)$ and $[\bar{1}11](101)$ move upwards, respectively [73]. Due to their interaction, junction dislocations are formed according to

$$\frac{a}{2}[111] + \frac{a}{2}[1\bar{1}\bar{1}] \rightarrow a[100]$$

and

$$\frac{a}{2}[\bar{1}\bar{1}\bar{1}] + \frac{a}{2}[\bar{1}11] \rightarrow a[\bar{1}00]$$

(a)

(b)
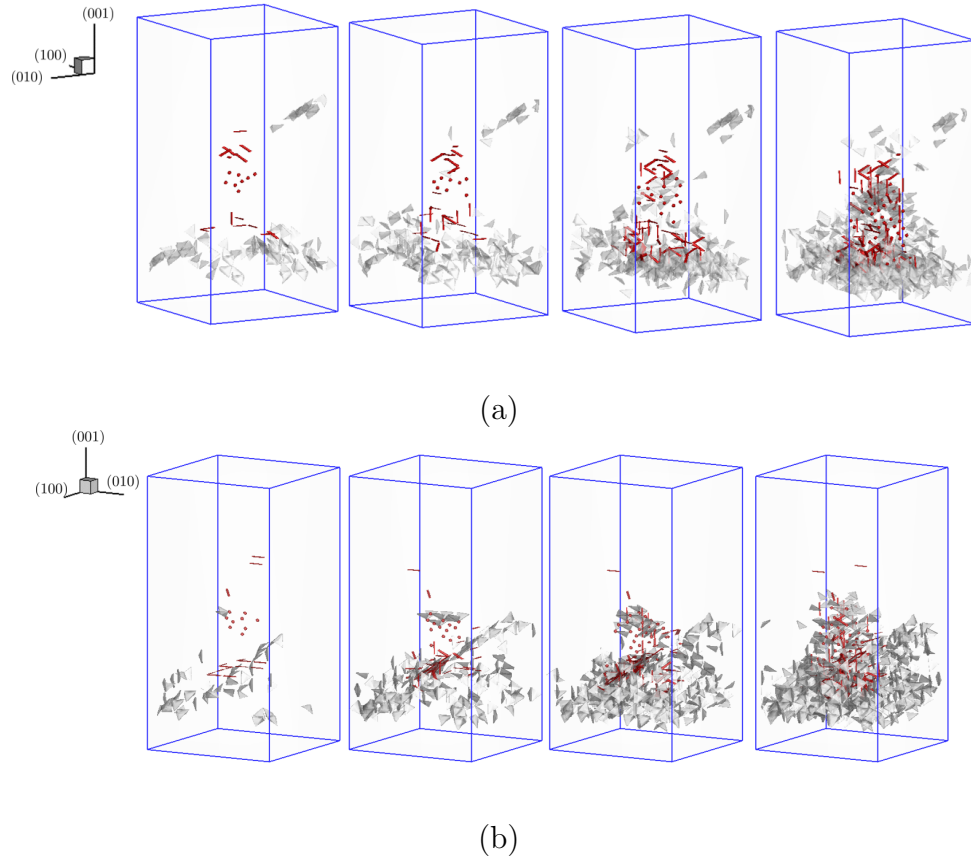
Figure 6.12: (a): $84nm \times 84nm \times 168nm$ model size at temperature $500K$; (b): $168nm \times 168nm \times 336nm$ model size at temperature $500K$. The grey planes(slip planes) are formed by wedge process zone elements, the red lines and dots are formed by prism process zone elements and truncated octahedron elements.

where a is the length of the Burgers vector.

From Fig.6.11(b), one may find that for the larger size specimen i.e. $168nm \times 168nm \times 336nm$ at $20K^o$, similar process happens but the primary slip plane becomes (101), then the secondary slip plane (011) will be activated and finally a third slip plane (101) forms at the last stage, which is in parallel with the first slip plane (101), but not the same slip plane. Therefore, the dislocation in $168nm \times 168nm \times 336nm$ will have double cross slips (two times "jump"). This example implies that the dislocation substructure might be also dependent on the size of a crystal specimen.

The slip plane configurations shown in Fig. 6.11 (a) and (b) indicate that at the low temperature there are approximately uniform distribution of screw dislocations in the middle section of the uniaxial compression specimen. At the very beginning when the critical resolved shear stress is reached, the screw dislocation glides easily on the slip plane, so that dislocation piles up and internal stress accumulates. As accumulated internal stress reached

a critical point, the secondary slip plane is activated. Therefore, the primary slip plane and the secondary slip plane interact each other so that stress is needed to produce additional plastic deformation. As internal stress is high enough for large scale cross-slip to set in, the dislocation in one slip plane is able to move to another slip plane. Experimental evidence showed that during this process, the primary dislocation can be regenerated, and a new dislocation is produced [74]. Thus, the cross slip is regarded as a dislocation multiplication mechanisms and hence plasticity hardening [75].

In Fig.6.12 , we show the results of dislocation pattern in the uniaxial compression bar $(84nm \times 84nm \times 168nm)$ and $(168nm \times 168nm \times 336nm)$ under the high temperature $(500k^o)$. From Fig.6.12, we can find that when temperature increases the dislocation pattern has changed: the distinct slip plane configuration under low temperature is replaced by many small dislocation cells, which also include many dipole elements, i.e. truncated octahedron elements and aggregated dislocation line elements, i.e. prism elements. This is because that high temperature will cause atoms have higher free energy to vibrate around their lattice positions, and hence it will lower the dislocation activation energy or the Peierls-Nabarro barrier potential to activate many other slip systems rather than the only one (the most packed plane) under the lower temperature. The consequence of many interacted activated slip planes and slip systems will be an aggregated dislocation cells, i.e. the cellular dislocation pattern as shown in Fig.6.12.

Chapter 7

Conclusions and Discussions

In this dissertation, we have further developed the recently proposed multiscale dislocation pattern dynamics by considering Temperature-related Higher-order Cauchy-Born(THCB) rule in different order process zone elements so that we can employ such temperature-related constitutive relation to calculate material responses of BCC crystal α-Ta at different temperatures.

It is shown that by using the proposed finite temperature multiscale dislocation pattern dynamics we are able to capture cross-slip in α-Ta under the low temperature, while we are able to simulate the cellular dislocation pattern in α-Ta at high temperature. Therefore we can conclude that the proposed finite temperature MCDD crystal plasticity formulation is able to capture different dislocation patterns of early stage based on first-principle constitutive relation and the super-dual lattice tessellation of finite element mesh.

Based on the numerical simulation results presented above, we have found that MCDD simulation has almost the same accuracy in terms of modeling stress-strain relation with that of molecular dynamics, but higher computation efficiency. This allows us to study mesoscale crystal plasticity at micron scale i.e. $1.0\mu m^3$ above, which is not reachable for MD simulations under current computer technology. Moreover, we have demonstrated that as a dislocation pattern dynamics, MCDD method can accurately predict the effect of crystal orientation on the yielding stress (asymmetry yielding contour with respect to stereographic triangle) by directly simulating the non-Schmid effect of BCC single crystals as well as capture the size effect of crystal plasticity in micron-scale.

This dissertation is highlighted by following advances: (1) The finite temperature MCDD model is able to capture accurate inelastic stress-strain relation comparable to MD results at both low and high temperatures, and we can even capture dislocation nucleation and growth process with obvious crystal plasticity. There is a significant development in computational efficiency, which allows us to take further steps in simulation of crystal plasticity model at millimeter scale that can be directly compared with experiment results; (2) MCDD model can capture the non-Schmid effect of BCC single crystal α-Ta that is consistent with the MD results; (3) MCDD model demonstrates that it can successfully capture size effect of up to $2.5\mu m^3$ micro-pillar specimen, which validates MCDD method in modeling and simulation

of crystal plasticity; (5) MCDD method can capture cross-slip at lower temperature and cellular dislocation pattern at high temperature in single crystal uniaxial compression test, and (6) MCDD simulation results suggested that the dislocation pattern distribution may be size-dependent as well.

We would like to emphasize the main and distinct advantages of the multiscale dislocation pattern dynamics, which are: (1) the multiscale crystal defect dynamics is an atomistically informed strain gradient crystal plasticity theory. It replies on the atomistic potential of crystal material to derive stress-strain relation without or with less empiricism, and it uses the material inherent and atomistically informed *hyperelastic* relation to naturally model crystal plasticity if the underline finite element mesh is a super dual lattice tessellation of the original crystal lattice; (2) being a multiscale strain gradient continuum theory, it does not need to model dislocation core but still mathematically well-posed and regulated, and (3) the super dual lattice tessellation finite element mesh consists of kinematic possible dislocation patterns at the early deformation stage, so that this is an inclusive approach, but not an ad hoc approach.

However, the method still has some unresolved issues. For example, in the current formulation, the higher-order traction forces are negligible. However, since the temperature effects has been included in the constitutive response, the temperature-related higher-order traction boundary condition may have significant effect on crystal plasticity as well. Moreover for macro-scale dislocation pattern dynamics simulations, it will need massive MPI parallel computation in order to resolve and accommodate the spatial and temporal scale of a particular dislocation pattern, which may range from 10 nm to 100 μm. For the above issues and more, we hope to deal with them in the subsequent work.

Bibliography

[1] Wikimedia Commons. File:2016 9-11 museum broken steel.jpg — wikimedia commons, the free media repository, 2021. [Online; accessed 7-May-2021].

[2] JA Shields, SH Goods, R Gibala, and TE Mitchell. Deformation of high purity tantalum single crystals at 4.2 k. *Materials Science and Engineering*, 20:71–81, 1975.

[3] W.A. Spitzig and T.E. Mitchell. Dislocation arrangements in tantalum single crystals deformed in tension at 373 k. *Acta metallurgica*, 14(10):1311–1323, 1966.

[4] Stefanos Papanikolaou, Yinan Cui, and Nasr Ghoniem. Avalanches and plastic flow in crystal plasticity: an overview. *Modelling and Simulation in Materials Science and Engineering*, 26(1):013001, 2017.

[5] Arina Marchenko, Matthieu Maziere, Samuel Forest, and Jean-Loup Strudel. Crystal plasticity simulation of strain aging phenomena in α-titanium at room temperature. *International Journal of Plasticity*, 85:1–33, 2016.

[6] J Sawkill and RWK Honeycombe. Strain hardening in face-centred cubic metal crystals. *Acta Metallurgica*, 2(6):854–864, 1954.

[7] Wikipedia contributors. Simplex — Wikipedia, the free encyclopedia, 2021. [Online; accessed 26-April-2021].

[8] P Li, ZF Zhang, XW Li, SX Li, and ZG Wang. Effect of orientation on the cyclic deformation behavior of silver single crystals: Comparison with the behavior of copper and nickel single crystals. *Acta materialia*, 57(16):4845–4854, 2009.

[9] C Buque, J Bretschneider, A Schwab, and C Holste. Effect of grain size and deformation temperature on the dislocation structure in cyclically deformed polycrystalline nickel. *Materials Science and Engineering: A*, 319:631–636, 2001.

[10] Joseph R Stephens. *Dislocation Structures in Slightly Strained Tungsten and Tungsten-rhenium and Tungsten-tantalum Alloys*. National Aeronautics and Space Administration, 1967.

[11] S. Li and G. Wang. *Introduction to micromechanics and nanomechanics*. World Scientific Publishing Company, 2008.

[12] K Ito and V Vitek. Atomistic study of non-schmid effects in the plastic yielding of bcc metals. *Philosophical Magazine A*, 81(5):1387–1407, 2001.

[13] R. Madec, B. Devincre, and L.P. Kubin. Simulation of dislocation patterns in multislip. *Scripta materialia*, 47(10):689–695, 2002.

[14] D. Gmez-Garca, B. Devincre, and L.P. Kubin. Dislocation patterns and the similitude principle: 2.5 d mesoscale simulations. *Physical review letters*, 96(12):125503, 2006.

[15] D.A. Hughes. Microstructure evolution, slip patterns and flow stress. *Materials Science and Engineering: A*, 319:46–54, 2001.

[16] N. Hansen, X. Huang, and G. Winther. Grain orientation, deformation microstructure and flow stress. *Materials Science and Engineering: A*, 494(1-2):61–67, 2008.

[17] G. Ananthakrishna. Current theoretical approaches to collective behavior of dislocations. *Physics Reports*, 440(4-6):113–259, 2007.

[18] Sauzay M. and Kubin L.P. Scaling laws for dislocation microstructures in monotonic and cyclic deformation of fcc metals. *Progress in Materials Science*, 56(6):725–84, 2011.

[19] D. Lyu and S. Li. Recent developments in dislocation pattern dynamics: Current opinions and perspectives. *Journal of Micromechanics and Molecular Physics*, 3:1840002, 2018.

[20] P. Li, S.X. Li, Z.G. Wang, and Z.F. Zhang. Unified factor controlling the dislocation evolution of fatigued face-centered cubic crystals. *Acta Materialia*, 129:98–111, 2017.

[21] P. Li and Z.F. Zhang. Standing wave effect and fractal structure in dislocation evolution. *Scientific Reports*, 7(1):1–6, 2017.

[22] D. An and S. Zaefferer. Formation mechanism of dislocation patterns under low cycle fatigue of a high-manganese austenitic trip steel with dominating planar slip mode. *International Journal of Plasticity*, 121:244–260, 2019.

[23] I. Groma, M. Zaiser, and P.D. Ispnovity. Dislocation patterning in a two-dimensional continuum theory of dislocations. *Physical Review B*, 93(21):214110, 2016.

[24] J. Hu, H. Song, Z. Liu, Z. Zhuang, X. Liu, and S. Sandfeld. Predicting the flow stress and dominant yielding mechanisms: analytical models based on discrete dislocation plasticity. *Scientific Reports*, 9(1):1–12, 2019.

[25] P.D. Ispnovity, S. Papanikolaou, and I. Groma. Emergence and role of dipolar dislocation patterns in discrete and continuum formulations of plasticity. *Physical Review B*, 101(2):024105, 2020.

[26] Z. Zhou, Y. Zhu, J. Luo, X. Yang, and X. Guo. Characterisation of dislocation patterning behaviour with a continuum dislocation dynamics model on two parallel slip planes equipped with a deep neural network resolving local microstructures. *International Journal of Solids and Structures*, 198:57–71, 2020.

[27] S. Groh, E.B. Marin, M.F. Horstemeyer, and H.M. Zbib. Multiscale modeling of the plasticity in an aluminum single crystal. *International Journal of Plasticity*, 25(8):1456–1473, 2009.

[28] Liming Xiong, Qian Deng, Garritt J Tucker, David L McDowell, and Youping Chen. Coarse-grained atomistic simulations of dislocations in al, ni and cu crystals. *International Journal of Plasticity*, 38:86–101, 2012.

[29] H. Lim, L.M. Hale, J.A. Zimmerman, C.C. Battaile, and C.R. Weinberger. A multiscale model of dislocation plasticity in a-fe: Incorporating temperature, strain rate and non-schmid effects. *International Journal of Plasticity*, 73:100–118, 2015.

[30] J. Amodeo, S. Dancette, and L. Delannay. Atomistically-informed crystal plasticity in mgo polycrystals under pressure. *International Journal of Plasticity*, 82:177–191, 2016.

[31] Thao Nguyen, Darby Jon Luscher, and Justin W Wilkerson. A dislocation-based crystal plasticity framework for dynamic ductile failure of single crystals. *Journal of the Mechanics and Physics of Solids*, 108:1–29, 2017.

[32] A Vattré, Benoit Devincre, F Feyel, R Gatti, S Groh, O Jamond, and A Roos. Modelling crystal plasticity by 3d dislocation dynamics and the finite element method: the discrete-continuous model revisited. *Journal of the Mechanics and Physics of Solids*, 63:491–505, 2014.

[33] S. Li, B. Ren, and H. Minaki. Multiscale crystal defect dynamics: a dual-lattice process zone model. *Philosophical Magazine*, 94(13):1414–1450, 2014.

[34] D. Lyu and S. Li. Multiscale crystal defect dynamics: A coarse-grained lattice defect model based on crystal microstructure. *Journal of the Mechanics and Physics of Solids*, 107:379–410, 2017.

[35] D. Lyu and S. Li. A multiscale dislocation pattern dynamics: Towards an atomistic-informed crystal plasticity theory. *Journal of the Mechanics and Physics of Solids*, 122:613–632, 2019.

[36] MP Ariza and M Ortiz. Discrete crystal elasticity and discrete dislocations in crystals. *Archive for Rational Mechanics and Analysis*, 178(2):149–226, 2005.

[37] D Kuhlmann-Wilsdorf and N. Hansen. Geometrically necessary, incidental and subgrain boundaries. *Scripta metallurgica et materialia*, 25(7):1557–1562, 1991.

[38] A Arsenlis and DM Parks. Crystallographic aspects of geometrically-necessary and statistically-stored dislocation density. *Acta materialia*, 47(5):1597–1611, 1999.

[39] L.-W. Zhang, Y. Xie, D. Lyu, and S. Li. Multiscale modeling of dislocation patterns and simulation of nanoscale plasticity in body-centered cubic (bcc) single crystals. *Journal of the Mechanics and Physics of Solids*, 2019.

[40] J.A. Shields, R. Gibala, and T.E. Mitchell. Dislocation substructure in ta-re-n alloys deformed at 77 k. *Metallurgical Transactions A*, 7(8):1111–1121, 1976.

[41] D. Cereceda, M. Diehl, F. Roters, D. Raabe, J.M. Perlado, and J. Marian. Unraveling the temperature dependence of the yield strength in single-crystal tungsten using atomistically-informed crystal plasticity calculations. *International Journal of Plasticity*, 78:242–265, 2016.

[42] John Price Hirth, Jens Lothe, and T Mura. Theory of dislocations. *Journal of Applied Mechanics*, 50(2):476, 1983.

[43] Wei Cai, Vasily V Bulatov, Jinpeng Chang, Ju Li, and Sidney Yip. Dislocation core effects on mobility. *Dislocations in solids*, 12:1–80, 2004.

[44] Minghua He and Shaofan Li. An embedded atom hyperelastic constitutive model and multiscale cohesive finite element method. *Computational Mechanics*, 49(3):337–355, 2012.

[45] Xiaohu Liu, Shaofan Li, and Ni Sheng. A cohesive finite element for quasi-continua. *Computational Mechanics*, 42(4):543–553, 2008.

[46] Lisheng Liu and Shaofan Li. A finite temperature multiscale interphase zone model and simulations of fracture. *Journal of engineering materials and technology*, 134(3), 2012.

[47] Bo Ren and Shaofan Li. A three-dimensional atomistic-based process zone model simulation of fragmentation in polycrystalline solids. *International Journal for Numerical Methods in Engineering*, 93(9):989–1014, 2013.

[48] A N Hirani. *Discrete exterior calculus.* PhD thesis, California Institute of Technology, 2003.

[49] JR Munkres. *Elements of algebraic topology.* CRC Press, 2018.

[50] C Motz, D Weygand, J Senger, and P Gumbsch. Initial dislocation structures in 3-d discrete dislocation dynamics and their influence on microscale plasticity. *Acta Materialia*, 57(6):1744–1754, 2009.

[51] JF Nye. Some geometrical relations in dislocated crystals. *Acta metallurgica*, 1(2):153–162, 1953.

[52] MF Ashby. The deformation of plastically non-homogeneous materials. *The Philosophical Magazine: A Journal of Theoretical Experimental and Applied Physics*, 21(170):399–424, 1970.

[53] J Hutchinson and N Fleck. Strain gradient plasticity. *Advances in applied mechanics*, 33:295–361, 1997.

[54] Huajian Gao and Yonggang Huang. Geometrically necessary dislocation and size-dependent plasticity. *Scripta Materialia*, 48(2):113–118, 2003.

[55] O Rezvanian, MA Zikry, and AM Rajendran. Statistically stored, geometrically necessary and grain boundary dislocation densities: microstructural representation and modelling. *Proceedings of the Royal Society A: Mathematical, Physical and Engineering Sciences*, 463(2087):2833–2853, 2007.

[56] Dayong An and Stefan Zaefferer. Formation mechanism of dislocation patterns under low cycle fatigue of a high-manganese austenitic trip steel with dominating planar slip mode. *International Journal of Plasticity*, 121:244–260, 2019.

[57] Dayong An, Huan Zhao, Binhan Sun, and Stefan Zaefferer. Direct observations of collinear dislocation interaction in a fe-17.4 mn-1.50 al-0.29 c (wt.%) austenitic steel under cyclic loading by in-situ electron channelling contrast imaging and cross-correlation electron backscatter diffraction. *Scripta Materialia*, 186:341–345, 2020.

[58] P Li and ZF Zhang. Physical origin of surface slip morphologies induced by regular self-organized dislocation patterns in fatigued copper single crystals. *Journal of Applied Physics*, 115(3):033504, 2014.

[59] E. Schmid and W. Boas. *Kristallplastizität Mit Besonderer Bercksichtigung der Metall.*

[60] H Chamati, NI Papanicolaou, Y Mishin, and DA Papaconstantopoulos. Embedded-atom potential for fe and its application to self-diffusion on fe (1 0 0). *Surface Science*, 600(9):1793–1803, 2006.

[61] XW Zhou, RA Johnson, and HNG Wadley. Misfit-energy-increasing dislocations in vapor-deposited cofe/nife multilayers. *Physical Review B*, 69(14):144113, 2004.

[62] R LeSar, R Najafabadi, and DJ Srolovitz. Finite-temperature defect properties from free-energy minimization. *Physical Review Letters*, 63(6):624, 1989.

[63] FH Featherston and JR Neighbours. Elastic constants of tantalum, tungsten, and molybdenum. *Physical Review*, 130(4):1324, 1963.

[64] M. Lazar, G.A. Maugin, and E.C. Aifantis. Dislocations in second strain gradient elasticity. *International Journal of Solids and Structures*, 43(6):1787–1817, 2006.

[65] M. Lazar. Non-singular dislocation continuum theories: strain gradient elasticity vs. peierlsnabarro model. *Philosophical Magazine*, 97(34):3246–3275, 2017.

[66] Thomas JR Hughes. *The finite element method: linear static and dynamic finite element analysis*. Courier Corporation, 2012.

[67] Ted Belytschko and Thomas JR Hughes. Computational methods for transient analysis. *Amsterdam, North-Holland(Computational Methods in Mechanics.*, 1, 1983.

[68] E. L. Wachspress. A rational basis for function approximation. In *Conference on Applications of Numerical Analysis*, pages 223–252. Springer, 1971.

[69] Michael S Floater and Ming-Jun Lai. Polygonal spline spaces and the numerical solution of the poisson equation. *SIAM Journal on Numerical Analysis*, 54(2):797–824, 2016.

[70] A Sinu, Sundararajan Natarajan, and K Shankar. Quadratic serendipity finite elements over convex polyhedra. *International Journal for Numerical Methods in Engineering*, 113(1):109–129, 2018.

[71] J.A. Moriarty, V. Vitek, V.V. Bulatov, and S. Yip. Atomistic simulations of dislocations and defects. *Journal of computer-aided materials design*, 9(2):99–132, 2002.

[72] O. T. Abad, J. M. Wheeler, J. Michler, A. S. Schneider, and E. Arzt. Temperature-dependent size effects on the strength of ta and w micropillars. *Acta Materialia*, 103:483–494, 2016.

[73] W. Wasserbäch. Anomalous slip in high-purity niobium and tantalum single crystals. *Physica status solidi (a)*, 147(2):417–446, 1995.

[74] F. Minari, B. Pichaud, and L. Capella. X-ray topographic observation of dislocation multiplication by cross-slip in cu crystals. *Philosophical Magazine*, 31(2):275–284, 1975.

[75] M. Sudmanns, M. Stricker, D. Weygand, T. Hochrainer, and K. Schulz. Dislocation multiplication by cross-slip and glissile reaction in a dislocation based continuum formulation of crystal plasticity. *Journal of the Mechanics and Physics of Solids*, 132:103695, 2019.

[76] Philippe B. Laval. Chapter9: Rotation about An Aritrary Axis, year = 1999, url = https://ksuweb.kennesaw.edu/ plaval/math4490/rotgen.pdf, urldate = 2010-09-30.

Appendix A

3D Hexagonal Prism Element Shape Functions and Derivatives

In this Appendix, we present the 3D hexagonal prism element shape functions and their first derivatives.

We first present the formulations of the 3D hexagonal prism element shape functions. To do so, we first need the auxiliary shape functions of the plane quadratic hexagonal element that are expressed as follows,

$$
\begin{aligned}
N_1(\xi, \eta) &= w_1(1 - 2w_2 - 2w_6); & N_2(\xi, \eta) &= w_2(1 - 2w_1 - 2w_3) \\
N_3(\xi, \eta) &= w_3(1 - 2w_2 - 2w_4); & N_4(\xi, \eta) &= w_4(1 - 2w_3 - 2w_5) \\
N_5(\xi, \eta) &= w_5(1 - 2w_4 - 2w_6); & N_6(\xi, \eta) &= w_6(1 - 2w_5 - 2w_1) \\
N_7(\xi, \eta) &= 4w_1w_2; \quad N_8(\xi, \eta) = 4w_2w_3; \quad N_9(\xi, \eta) = 4w_3w_4; \\
N_{10}(\xi, \eta) &= 4w_4w_5; \quad N_{11}(\xi, \eta) = 4w_5w_6; \quad N_{12}(\xi, \eta) = 4w_6w_1 \ .
\end{aligned}
\tag{A.1}
$$

in which, basis functions $w_k, k = 1 \sim 6$ are shown below:

$$
\begin{aligned}
w_1(\xi, \eta) &= -\frac{\sqrt{3}}{3} \frac{\left(\frac{\xi}{\sqrt{3}} - \eta + 1\right)\left(\xi + \frac{3}{2}\right)\left(-\frac{\xi}{\sqrt{3}} - \eta - 1\right)\left(\frac{\xi}{3} - \eta - 1\right)}{\xi^2 + \eta^2 - 3}, \\
w_2(\xi, \eta) &= \frac{2}{3} \frac{\left(\xi + \frac{\sqrt{3}}{2}\right)\left(-\frac{\xi}{\sqrt{3}} - \eta - 1\right)\left(\frac{\xi}{\sqrt{3}} - \eta - 1\right)\left(\xi - \frac{\sqrt{3}}{2}\right)}{\xi^2 + \eta^2 - 3}, \\
w_3(\xi, \eta) &= \frac{\sqrt{3}}{3} \frac{\left(-\frac{\xi}{\sqrt{3}} - \eta - 1\right)\left(\frac{\xi}{\sqrt{3}} - \eta - 1\right)\left(\xi - \frac{\sqrt{3}}{2}\right)\left(-\frac{\xi}{\sqrt{3}} - \eta + 1\right)}{\xi^2 + \eta^2 - 3}, \\
w_4(\xi, \eta) &= -\frac{\sqrt{3}}{3} \frac{\left(\frac{\xi}{\sqrt{3}} - \eta - 1\right)\left(\xi - \frac{\sqrt{3}}{2}\right)\left(-\frac{\xi}{\sqrt{3}} - \eta + 1\right)\left(\frac{\xi}{\sqrt{3}} - \eta + 1\right)}{\xi^2 + \eta^2 - 3}, \\
w_5(\xi, \eta) &= \frac{2}{3} \frac{\left(\xi - \frac{\sqrt{3}}{2}\right)\left(-\frac{\xi}{\sqrt{3}} - \eta + 1\right)\left(\frac{\xi}{\sqrt{3}} - \eta + 1\right)\left(\xi + \frac{\sqrt{3}}{2}\right)}{\xi^2 + \eta^2 - 3}, \\
w_6(\xi, \eta) &= \frac{\sqrt{3}}{3} \frac{\left(-\frac{\xi}{\sqrt{3}} - \eta + 1\right)\left(\frac{\xi}{\sqrt{3}} - \eta + 1\right)\left(\xi + \frac{\sqrt{3}}{2}\right)\left(-\frac{\xi}{\sqrt{3}} - \eta - 1\right)}{\xi^2 + \eta^2 - 3}.
\end{aligned}
\tag{A.2}
$$

Thus, it is very natural to extend the 2D hexagonal element shape functions to 3D hexagonal prism element shape functions as shown in Fig.6.9(b) in the text. The shape functions are

given below:

$$N_1 = w_1(1 - 2w_2 - 2w_6)\frac{(1+\zeta)\zeta}{2}; \tag{A.3}$$

$$N_2 = w_2(1 - 2w_1 - 2w_3)\frac{(1+\zeta)\zeta}{2} \tag{A.4}$$

$$N_3 = w_3(1 - 2w_2 - 2w_4)\frac{(1+\zeta)\zeta}{2}; \tag{A.5}$$

$$N_4 = w_4(1 - 2w_3 - 2w_5)\frac{(1+\zeta)\zeta}{2} \tag{A.6}$$

$$N_5 = w_5(1 - 2w_4 - 2w_6)\frac{(1+\zeta)\zeta}{2}; \tag{A.7}$$

$$N_6 = w_6(1 - 2w_5 - 2w_1)\frac{(1+\zeta)\zeta}{2} \tag{A.8}$$

$$N_7 = 4w_1w_2\frac{(1+\zeta)\zeta}{2}; \quad N_8 = 4w_2w_3\frac{(1+\zeta)\zeta}{2}; \tag{A.9}$$

$$N_9 = 4w_3w_4\frac{(1+\zeta)\zeta}{2}; \quad N_{10} = 4w_4w_5\frac{(1+\zeta)\zeta}{2}; \tag{A.10}$$

$$N_{11} = 4w_5w_6\frac{(1+\zeta)\zeta}{2}; \quad N_{12} = 4w_6w_1\frac{(1+\zeta)\zeta}{2}; \tag{A.11}$$

$$N_{13} = w_1(1 - 2w_2 - 2w_6)\frac{(\zeta-1)\zeta}{2}; \tag{A.12}$$

$$N_{14} = w_2(1 - 2w_1 - 2w_3)\frac{(\zeta-1)\zeta}{2} \tag{A.13}$$

$$N_{15} = w_3(1 - 2w_2 - 2w_4)\frac{(\zeta-1)\zeta}{2}; \tag{A.14}$$

$$N_{16} = w_4(1 - 2w_3 - 2w_5)\frac{(\zeta-1)\zeta}{2} \tag{A.15}$$

$$N_{17} = w_5(1 - 2w_4 - 2w_6)\frac{(\zeta-1)\zeta}{2}; \tag{A.16}$$

$$N_{18} = w_6(1 - 2w_5 - 2w_1)\frac{(\zeta-1)\zeta}{2} \tag{A.17}$$

$$N_{19} = 4w_1w_2\frac{(\zeta-1)\zeta}{2}; \quad N_{20} = 4w_2w_3\frac{(\zeta-1)\zeta}{2}; \tag{A.18}$$

$$N_{21} = 4w_3w_4\frac{(\zeta-1)\zeta}{2}; \quad N_{22} = 4w_4w_5\frac{(\zeta-1)\zeta}{2}; \tag{A.19}$$

$$N_{23} = 4w_5w_6\frac{(\zeta-1)\zeta}{2}; \quad N_{24} = 4w_6w_1\frac{(\zeta-1)\zeta}{2}; \tag{A.20}$$

$$N_{25} = -\frac{\sqrt{3}}{3}\frac{\left(\frac{\xi}{\sqrt{3}}-\eta+1\right)\left(\xi+\frac{\sqrt{3}}{2}\right)\left(-\frac{\xi}{\sqrt{3}}-\eta-1\right)\left(\frac{\xi}{\sqrt{3}}-\eta-1\right)}{\xi^2+\eta^2-3}(1-\zeta^2); \tag{A.21}$$

$$N_{26} = \frac{2}{3}\frac{\left(\xi+\frac{\sqrt{3}}{2}\right)\left(-\frac{\xi}{\sqrt{3}}-\eta-1\right)\left(\frac{\xi}{\sqrt{3}}-\eta-1\right)\left(\xi-\frac{\sqrt{3}}{2}\right)}{\xi^2+\eta^2-3}(1-\zeta^2); \tag{A.22}$$

$$N_{27} = \frac{\sqrt{3}}{3}\frac{\left(-\frac{\xi}{\sqrt{3}}-\eta-1\right)\left(\frac{\xi}{\sqrt{3}}-\eta-1\right)\left(\xi-\frac{\sqrt{3}}{2}\right)\left(-\frac{\xi}{\sqrt{3}}-\eta+1\right)}{\xi^2+\eta^2-3}(1-\zeta^2); \tag{A.23}$$

$$N_{28} = -\frac{\sqrt{3}}{3}\frac{\left(\frac{\xi}{\sqrt{3}}-\eta-1\right)\left(\xi-\frac{\sqrt{3}}{2}\right)\left(-\frac{\xi}{\sqrt{3}}-\eta+1\right)\left(\frac{\xi}{\sqrt{3}}-\eta+1\right)}{\xi^2+\eta^2-3}(1-\zeta^2); \tag{A.24}$$

$$N_{29} = \frac{2}{3}\frac{\left(\xi-\frac{\sqrt{3}}{2}\right)\left(-\frac{\xi}{\sqrt{3}}-\eta-1\right)\left(\frac{\xi}{\sqrt{3}}-\eta+1\right)\left(\xi+\frac{\sqrt{3}}{2}\right)}{\xi^2+\eta^2-3}(1-\xi^2); \tag{A.25}$$

$$N_{30} = \frac{\sqrt{3}}{3}\frac{\left(-\frac{\xi}{\sqrt{3}}-\eta+1\right)\left(\frac{\xi}{\sqrt{3}}-\eta+1\right)\left(\xi+\frac{\sqrt{3}}{2}\right)\left(-\frac{\xi}{\sqrt{3}}-\eta-1\right)}{\xi^2+\eta^2-3}(1-\zeta^2). \tag{A.26}$$

To calculate the derivatives of 3D hexagonal prism element shape functions, we first provide the derivatives of derivative of the wedge basis functions, which are shown below,

$$\begin{aligned}
\frac{\partial w_1}{\partial \xi} = {}& -\frac{\sqrt{3}}{3}\frac{1}{18(\xi^2+\eta^2-3)^2}\Big\{-4\sqrt{3}\xi^5+\xi^4(6\eta-9)-8\sqrt{3}\xi^3(\eta^2-3) \\
& + 18\times\xi^2(2\eta^3-\eta^2-5\eta+3)+12\sqrt{3}\xi(\eta^4+4\eta^3-\eta^2-9\eta-3) \\
& - 9(\eta+1)^2(2\eta^3-3\eta^2-6\eta+9)\Big\}, \tag{A.27}
\end{aligned}$$

$$\begin{aligned}
\frac{\partial w_1}{\partial \eta} = {}& -\frac{\sqrt{3}}{3}\frac{2\xi+\sqrt{3}}{18(\xi^2+\eta^2-3)^2}\Big\{3\xi^4+2\sqrt{3}\xi^3(4\eta+3)-6\xi^2\eta(5\eta+2) \\
& - 6\sqrt{3}\xi(\eta^2+4\eta+3)-9(\eta^4-8\eta^2-4\eta+3)\Big\}; \tag{A.28}
\end{aligned}$$

$$\frac{\partial w_2}{\partial \xi} = \frac{2}{3}\left\{-\frac{\xi\left[2\xi^4+4\xi^2(\eta^2-3)+3(-2\eta^4-4\eta^3+2\eta^2+9\eta+6)\right]}{3(\xi^2+\eta^2-3)^2}\right\}, \tag{A.29}$$

$$\frac{\partial w_2}{\partial \eta} = \frac{2}{3}\left\{-\frac{(\sqrt{3}-2\xi)(2\xi+\sqrt{3})\left[\xi^2(4\eta+3)-3(\eta^2+4\eta+3)\right]}{6(\xi^2+\eta^2-3)^2}\right\}; \tag{A.30}$$

$$\frac{\partial w_3}{\partial \xi} = \frac{\sqrt{3}}{54(\xi^2 + \eta^2 - 3)^2}\Big\{4\sqrt{3}\xi^5 + \xi^4(6\eta - 9) + 8\sqrt{3}\xi^3(\eta^2 - 3)$$
$$+ \quad 18\xi^2(2\eta^3 - \eta^2 - 5\eta + 3)$$
$$- \quad 12\sqrt{3}\xi(\eta^4 + 4\eta^3 - \eta^2 - 9\eta - 3) - 9(\eta + 1)^2(2\eta^3 - 3\eta^2 - 6\eta + 9)\Big\}, \quad \text{(A.31)}$$

$$\frac{\partial w_3}{\partial \eta} = \frac{\sqrt{3}}{3}\frac{\sqrt{3} - 2\xi}{18(\xi^2 + \eta^2 - 3)^2}\Big\{-3\xi^4 + 2\sqrt{3}\xi^3(4\eta + 3) + 6\xi^2\eta(5\eta + 2)$$
$$- \quad 6\sqrt{3}\xi(\eta^2 + 4\eta + 3) + 9(\eta^4 - 8\eta^2 - 4\eta + 3)\Big\}; \quad \text{(A.32)}$$

$$\frac{\partial w_4}{\partial \xi} = -\frac{\sqrt{3}}{54(\xi^2 + \eta^2 - 3)^2}\Big\{-4\sqrt{3}\xi^5 + \xi^4(6\eta + 9) - 8\sqrt{3}\xi^3(\eta^2 - 3)$$
$$+ \quad 18\xi^2(2\eta^3 + \eta^2 - 5\eta - 3)$$
$$+ \quad 12\sqrt{3}\xi(\eta^4 - 4\eta^3 - \eta^2 + 9\eta - 3) - 9(\eta - 1)^2(2\eta^3 + 3\eta^2 - 6\eta - 9)\Big\}, \quad \text{(A.33)}$$

$$\frac{\partial w_4}{\partial \eta} = \frac{\sqrt{3}}{3}\frac{\sqrt{3} - 2\xi}{18(\xi^2 + \eta^2 - 3)^2}\Big\{3\xi^4 + 2\sqrt{3}\xi^3(4\eta - 3) - 6\xi^2\eta(5\eta - 2)$$
$$+ \quad 6\sqrt{3}\xi(\eta^2 - 4\eta + 3) - 9(\eta^4 - 8\eta^2 + 4\eta + 3)\Big\}; \quad \text{(A.34)}$$

$$\frac{\partial w_5}{\partial \xi} = \frac{2}{3}\Big\{-\frac{\xi[2\xi^4 + 4\xi^2(\eta^2 - 3) + 3(-2\eta^4 + 4\eta^3 + 2\eta^2 - 9\eta + 6)]}{3(\xi^2 + \eta^2 - 3)^2}\Big\}, \quad \text{(A.35)}$$

$$\frac{\partial w_5}{\partial \eta} = \frac{2}{3}\Big\{-\frac{(\sqrt{3} - 2\xi)(2\xi + \sqrt{3})[\xi^2(4\eta - 3) + 3(\eta^2 - 4\eta + 3)]}{6(\xi^2 + \eta^2 - 3)^2}\Big\}, \quad \text{(A.36)}$$

and

$$\frac{\partial w_6}{\partial \xi} = \frac{\sqrt{3}}{54(\xi^2 + \eta^2 - 3)^2}\Big\{4\sqrt{3}\xi^5 + \xi^4(6\eta + 9) + 8\sqrt{3}\xi^3(\eta^2 - 3)$$
$$+ \quad 18\xi^2(2\eta^3 + \eta^2 - 5\eta - 3)$$
$$- \quad 12\sqrt{3}\xi(\eta^4 - 4\eta^3 - \eta^2 + 9\eta - 3) - 9(\eta - 1)^2(2\eta^3 + 3\eta^2 - 6\eta - 9)\Big\}, \quad \text{(A.37)}$$

$$\frac{\partial w_6}{\partial \eta} = -\frac{\sqrt{3}(2\xi + \sqrt{3})}{54(\xi^2 + \eta^2 - 3)^2}\Big\{-3\xi^4 + 2\sqrt{3}\xi^3(4\eta - 3) + 6\xi^2\eta(5\eta - 2)$$
$$+ \quad 6\sqrt{3}\xi(\eta^2 - 4\eta + 3) + 9(\eta^4 - 8\eta^2 + 4\eta + 3)\Big\}. \quad \text{(A.38)}$$

Therefore, we can have the first order derivatives of 3D hexagonal prism elements shape

functions as shown below:

$$\frac{\partial N_1}{\partial \xi} = \left(\frac{\partial w_1}{\partial \xi} - 2\frac{\partial w_1}{\partial \xi}w_2 - 2w_1\frac{\partial w_2}{\partial \xi} - 2\frac{\partial w_1}{\partial \xi}w_6 - 2w_1\frac{\partial w_6}{\partial \xi}\right)\frac{(1+\zeta)\zeta}{2},$$

$$\frac{\partial N_1}{\partial \eta} = \left(\frac{\partial w_1}{\partial \eta} - 2\frac{\partial w_1}{\partial \eta}w_2 - 2w_1\frac{\partial w_2}{\partial \eta} - 2\frac{\partial w_1}{\partial \eta}w_6 - 2w_1\frac{\partial w_6}{\partial \eta}\right)\frac{(1+\zeta)\zeta}{2}, \qquad \text{(A.39)}$$

$$\frac{\partial N_1}{\partial \zeta} = w_1\left(1 - 2w_1 - 2w_6\right)\frac{1+2\zeta}{2} \ .$$

$$\frac{\partial N_2}{\partial \xi} = \left(\frac{\partial w_2}{\partial \xi} - 2\frac{\partial w_1}{\partial \xi}w_2 - 2w_1\frac{\partial w_2}{\partial \xi} - 2\frac{\partial w_2}{\partial \xi}w_3 - 2w_2\frac{\partial w_3}{\partial \xi}\right)\frac{(1+\zeta)\zeta}{2},$$

$$\frac{\partial N_2}{\partial \eta} = \left(\frac{\partial w_2}{\partial \eta} - 2\frac{\partial w_1}{\partial \eta}w_2 - 2w_1\frac{\partial w_2}{\partial \eta} - 2\frac{\partial w_2}{\partial \eta}w_3 - 2w_2\frac{\partial w_3}{\partial \eta}\right)\frac{(1+\zeta)\zeta}{2}, \qquad \text{(A.40)}$$

$$\frac{\partial N_2}{\partial \zeta} = \left(w_2 - 2w_1w_2 - 2w_2w_3\right)\frac{1+2\zeta}{2} \ .$$

$$\frac{\partial N_3}{\partial \xi} = \left(\frac{\partial w_3}{\partial \xi} - 2\frac{\partial w_2}{\partial \xi}w_3 - 2w_2\frac{\partial w_3}{\partial \xi} - 2\frac{\partial w_3}{\partial \xi}w_4 - 2w_3\frac{\partial w_4}{\partial \xi}\right)\frac{(1+\zeta)\zeta}{2},$$

$$\frac{\partial N_3}{\partial \eta} = \left(\frac{\partial w_3}{\partial \eta} - 2\frac{\partial w_2}{\partial \eta}w_3 - 2w_2\frac{\partial w_3}{\partial \eta} - 2\frac{\partial w_3}{\partial \eta}w_4 - 2w_3\frac{\partial w_4}{\partial \eta}\right)\frac{(1+\zeta)\zeta}{2}, \qquad \text{(A.41)}$$

$$\frac{\partial N_3}{\partial \zeta} = \left(w_3 - 2w_2w_3 - 2w_3w_4\right)\frac{1+2\zeta}{2} \ .$$

$$\frac{\partial N_4}{\partial \xi} = \left(\frac{\partial w_4}{\partial \xi} - 2\frac{\partial w_3}{\partial \xi}w_4 - 2w_3\frac{\partial w_4}{\partial \xi} - 2\frac{\partial w_4}{\partial \xi}w_5 - 2w_4\frac{\partial w_5}{\partial \xi}\right)\frac{(1+\zeta)\zeta}{2},$$

$$\frac{\partial N_4}{\partial \eta} = \left(\frac{\partial w_4}{\partial \eta} - 2\frac{\partial w_3}{\partial \eta}w_4 - 2w_3\frac{\partial w_4}{\partial \eta} - 2\frac{\partial w_4}{\partial \eta}w_5 - 2w_4\frac{\partial w_5}{\partial \eta}\right)\frac{(1+\zeta)\zeta}{2}, \qquad \text{(A.42)}$$

$$\frac{\partial N_4}{\partial \zeta} = \left(w_4 - 2w_3w_4 - 2w_4w_5\right)\frac{1+2\zeta}{2} \ .$$

$$\frac{\partial N_5}{\partial \xi} = \left(\frac{\partial w_5}{\partial \xi} - 2\frac{\partial w_4}{\partial \xi}w_5 - 2w_4\frac{\partial w_5}{\partial \xi} - 2\frac{\partial w_5}{\partial \xi}w_6 - 2w_5\frac{\partial w_6}{\partial \xi}\right)\frac{(1+\zeta)\zeta}{2},$$

$$\frac{\partial N_5}{\partial \eta} = \left(\frac{\partial w_5}{\partial \eta} - 2\frac{\partial w_4}{\partial \eta}w_5 - 2w_4\frac{\partial w_5}{\partial \eta} - 2\frac{\partial w_5}{\partial \eta}w_6 - 2w_5\frac{\partial w_6}{\partial \eta}\right)\frac{(1+\zeta)\zeta}{2}, \qquad \text{(A.43)}$$

$$\frac{\partial N_5}{\partial \zeta} = \left(w_5 - 2w_4w_5 - 2w_5w_6\right)\frac{1+2\zeta}{2} \ .$$

$$\frac{\partial N_6}{\partial \xi} = \left(\frac{\partial w_6}{\partial \xi} - 2\frac{\partial w_5}{\partial \xi}w_6 - 2w_5\frac{\partial w_6}{\partial \xi} - 2\frac{\partial w_1}{\partial \xi}w_6 - 2w_1\frac{\partial w_6}{\partial \xi}\right)\frac{(1+\zeta)\zeta}{2},$$

$$\frac{\partial N_6}{\partial \eta} = \left(\frac{\partial w_6}{\partial \eta} - 2\frac{\partial w_5}{\partial \eta}w_6 - 2w_5\frac{\partial w_6}{\partial \eta} - 2\frac{\partial w_1}{\partial \eta}w_6 - 2w_1\frac{\partial w_6}{\partial \eta}\right)\frac{(1+\zeta)\zeta}{2}, \qquad \text{(A.44)}$$

$$\frac{\partial N_6}{\partial \zeta} = \left(w_6 - 2w_5w_6 - 2w_1w_6\right)\frac{1+2\zeta}{2} \ .$$

$$\frac{\partial N_7}{\partial \xi} = 2(1+\zeta)\zeta\left[\frac{\partial w_1}{\partial \xi}w_2 + w_1\frac{\partial w_2}{\partial \xi}\right],$$

$$\frac{\partial N_7}{\partial \eta} = 2(1+\zeta)\zeta\left[\frac{\partial w_1}{\partial \eta}w_2 + w_1\frac{\partial w_2}{\partial \eta}\right], \tag{A.45}$$

$$\frac{\partial N_7}{\partial \zeta} = 2w_1w_2(1+2\zeta) \ .$$

$$\frac{\partial N_8}{\partial \xi} = 2(1+\zeta)\zeta\left[\frac{\partial w_2}{\partial \xi}w_3 + w_2\frac{\partial w_3}{\partial \xi}\right],$$

$$\frac{\partial N_8}{\partial \eta} = 2(1+\zeta)\zeta\left[\frac{\partial w_2}{\partial \eta}w_3 + w_2\frac{\partial w_3}{\partial \eta}\right], \tag{A.46}$$

$$\frac{\partial N_8}{\partial \zeta} = 2w_2w_3(1+2\zeta) \ .$$

$$\frac{\partial N_9}{\partial \xi} = 2(1+\zeta)\zeta\left[\frac{\partial w_3}{\partial \xi}w_4 + w_3\frac{\partial w_4}{\partial \xi}\right],$$

$$\frac{\partial N_9}{\partial \eta} = 2(1+\zeta)\zeta\left[\frac{\partial w_3}{\partial \eta}w_4 + w_3\frac{\partial w_4}{\partial \eta}\right], \tag{A.47}$$

$$\frac{\partial N_9}{\partial \zeta} = 2(1+2\zeta)w_3w_4 \ .$$

$$\frac{\partial N_{10}}{\partial \xi} = 2(1+\zeta)\zeta\left[\frac{\partial w_4}{\partial \xi}w_5 + w_4\frac{\partial w_5}{\partial \xi}\right],$$

$$\frac{\partial N_{10}}{\partial \eta} = 2(1+\zeta)\zeta\left[\frac{\partial w_4}{\partial \eta}w_5 + w_4\frac{\partial w_5}{\partial \eta}\right], \tag{A.48}$$

$$\frac{\partial N_{10}}{\partial \zeta} = 2(1+2\zeta)w_4w_5 \ .$$

$$\frac{\partial N_{11}}{\partial \xi} = 2(1+\zeta)\zeta\left[\frac{\partial w_5}{\partial \xi}w_6 + w_5\frac{\partial w_6}{\partial \xi}\right],$$

$$\frac{\partial N_{11}}{\partial \eta} = 2(1+\zeta)\zeta\left[\frac{\partial w_5}{\partial \eta}w_6 + w_5\frac{\partial w_6}{\partial \eta}\right], \tag{A.49}$$

$$\frac{\partial N_{11}}{\partial \zeta} = 2(1+2\zeta)w_5w_6 \ .$$

$$\frac{\partial N_{12}}{\partial \xi} = 2(1+\zeta)\zeta\left[\frac{\partial w_1}{\partial \xi}w_6 + w_1\frac{\partial w_6}{\partial \xi}\right],$$

$$\frac{\partial N_{12}}{\partial \eta} = 2(1+\zeta)\zeta\left[\frac{\partial w_1}{\partial \eta}w_6 + w_1\frac{\partial w_6}{\partial \eta}\right], \tag{A.50}$$

$$\frac{\partial N_{12}}{\partial \zeta} = 2(1+2\zeta)w_1w_6 \ .$$

$$\frac{\partial N_{13}}{\partial \xi} = \Big(\frac{\partial w_1}{\partial \xi} - 2\frac{\partial w_1}{\partial \xi}w_2 - 2w_1\frac{\partial w_2}{\partial \xi} - 2\frac{\partial w_1}{\partial \xi}w_6 - 2w_1\frac{\partial w_6}{\partial \xi}\Big)\frac{(\zeta-1)\zeta}{2},$$

$$\frac{\partial N_{13}}{\partial \eta} = \Big(\frac{\partial w_1}{\partial \eta} - 2\frac{\partial w_1}{\partial \eta}w_2 - 2w_1\frac{\partial w_2}{\partial \eta} - 2\frac{\partial w_1}{\partial \eta}w_6 - 2w_1\frac{\partial w_6}{\partial \eta}\Big)\frac{(\zeta-1)\zeta}{2}, \qquad (A.51)$$

$$\frac{\partial N_{13}}{\partial \zeta} = w_1\Big(1 - 2w_1 - 2w_6\Big)\frac{2\zeta-1}{2}.$$

$$\frac{\partial N_{14}}{\partial \xi} = \Big(\frac{\partial w_2}{\partial \xi} - 2\frac{\partial w_1}{\partial \xi}w_2 - 2w_1\frac{\partial w_2}{\partial \xi} - 2\frac{\partial w_2}{\partial \xi}w_3 - 2w_2\frac{\partial w_3}{\partial \xi}\Big)\frac{(\zeta-1)\zeta}{2},$$

$$\frac{\partial N_{14}}{\partial \eta} = \Big(\frac{\partial w_2}{\partial \eta} - 2\frac{\partial w_1}{\partial \eta}w_2 - 2w_1\frac{\partial w_2}{\partial \eta} - 2\frac{\partial w_2}{\partial \eta}w_3 - 2w_2\frac{\partial w_3}{\partial \eta}\Big)\frac{(\zeta-1)\zeta}{2}, \qquad (A.52)$$

$$\frac{\partial N_{14}}{\partial \zeta} = \Big(w_2 - 2w_1w_2 - 2w_2w_3\Big)\frac{2\zeta-1}{2}.$$

$$\frac{\partial N_{15}}{\partial \xi} = \Big(\frac{\partial w_3}{\partial \xi} - 2\frac{\partial w_2}{\partial \xi}w_3 - 2w_2\frac{\partial w_3}{\partial \xi} - 2\frac{\partial w_3}{\partial \xi}w_4 - 2w_3\frac{\partial w_4}{\partial \xi}\Big)\frac{(\zeta-1)\zeta}{2},$$

$$\frac{\partial N_{15}}{\partial \eta} = \Big(\frac{\partial w_3}{\partial \eta} - 2\frac{\partial w_2}{\partial \eta}w_3 - 2w_2\frac{\partial w_3}{\partial \eta} - 2\frac{\partial w_3}{\partial \eta}w_4 - 2w_3\frac{\partial w_4}{\partial \eta}\Big)\frac{(\zeta-1)\zeta}{2}, \qquad (A.53)$$

$$\frac{\partial N_{15}}{\partial \zeta} = \Big(w_3 - 2w_2w_3 - 2w_3w_4\Big)\frac{2\zeta-1}{2}.$$

$$\frac{\partial N_{16}}{\partial \xi} = \Big(\frac{\partial w_4}{\partial \xi} - 2\frac{\partial w_3}{\partial \xi}w_4 - 2w_3\frac{\partial w_4}{\partial \xi} - 2\frac{\partial w_4}{\partial \xi}w_5 - 2w_4\frac{\partial w_5}{\partial \xi}\Big)\frac{(\zeta-1)\zeta}{2},$$

$$\frac{\partial N_{16}}{\partial \eta} = \Big(\frac{\partial w_4}{\partial \eta} - 2\frac{\partial w_3}{\partial \eta}w_4 - 2w_3\frac{\partial w_4}{\partial \eta} - 2\frac{\partial w_4}{\partial \eta}w_5 - 2w_4\frac{\partial w_5}{\partial \eta}\Big)\frac{(\zeta-1)\zeta}{2}, \qquad (A.54)$$

$$\frac{\partial N_{16}}{\partial \zeta} = \Big(w_4 - 2w_3w_4 - 2w_4w_5\Big)\frac{2\zeta-1}{2}.$$

$$\frac{\partial N_{17}}{\partial \xi} = \Big(\frac{\partial w_5}{\partial \xi} - 2\frac{\partial w_4}{\partial \xi}w_5 - 2w_4\frac{\partial w_5}{\partial \xi} - 2\frac{\partial w_5}{\partial \xi}w_6 - 2w_5\frac{\partial w_6}{\partial \xi}\Big)\frac{(\zeta-1)\zeta}{2},$$

$$\frac{\partial N_{17}}{\partial \eta} = \Big(\frac{\partial w_5}{\partial \eta} - 2\frac{\partial w_4}{\partial \eta}w_5 - 2w_4\frac{\partial w_5}{\partial \eta} - 2\frac{\partial w_5}{\partial \eta}w_6 - 2w_5\frac{\partial w_6}{\partial \eta}\Big)\frac{(\zeta-1)\zeta}{2}, \qquad (A.55)$$

$$\frac{\partial N_{17}}{\partial \zeta} = \Big(w_5 - 2w_4w_5 - 2w_5w_6\Big)\frac{2\zeta-1}{2}.$$

$$\frac{\partial N_{18}}{\partial \xi} = \Big(\frac{\partial w_6}{\partial \xi} - 2\frac{\partial w_5}{\partial \xi}w_6 - 2w_5\frac{\partial w_6}{\partial \xi} - 2\frac{\partial w_1}{\partial \xi}w_6 - 2w_1\frac{\partial w_6}{\partial \xi}\Big)\frac{(\zeta-1)\zeta}{2},$$

$$\frac{\partial N_{18}}{\partial \eta} = \Big(\frac{\partial w_6}{\partial \eta} - 2\frac{\partial w_5}{\partial \eta}w_6 - 2w_5\frac{\partial w_6}{\partial \eta} - 2\frac{\partial w_1}{\partial \eta}w_6 - 2w_1\frac{\partial w_6}{\partial \eta}\Big)\frac{(\zeta-1)\zeta}{2}, \qquad (A.56)$$

$$\frac{\partial N_{18}}{\partial \zeta} = \Big(w_6 - 2w_5w_6 - 2w_1w_6\Big)\frac{2\zeta-1}{2}.$$

$$\frac{\partial N_{19}}{\partial \xi} = 2(\zeta - 1)\zeta \left[\frac{\partial w_1}{\partial \xi} w_2 + w_1 \frac{\partial w_2}{\partial \xi} \right],$$

$$\frac{\partial N_{19}}{\partial \eta} = 2(\zeta - 1)\zeta \left[\frac{\partial w_1}{\partial \eta} w_2 + w_1 \frac{\partial w_2}{\partial \eta} \right], \tag{A.57}$$

$$\frac{\partial N_{19}}{\partial \zeta} = 2w_1 w_2 (2\zeta - 1) \ .$$

$$\frac{\partial N_{20}}{\partial \xi} = 2(\zeta - 1)\zeta \left[\frac{\partial w_2}{\partial \xi} w_3 + w_2 \frac{\partial w_3}{\partial \xi} \right],$$

$$\frac{\partial N_{20}}{\partial \eta} = 2(\zeta - 1)\zeta \left[\frac{\partial w_2}{\partial \eta} w_3 + w_2 \frac{\partial w_3}{\partial \eta} \right], \tag{A.58}$$

$$\frac{\partial N_{20}}{\partial \zeta} = 2w_2 w_3 (2\zeta - 1) \ .$$

$$\frac{\partial N_{21}}{\partial \xi} = 2(\zeta - 1)\zeta \left[\frac{\partial w_3}{\partial \xi} w_4 + w_3 \frac{\partial w_4}{\partial \xi} \right],$$

$$\frac{\partial N_{21}}{\partial \eta} = 2(\zeta - 1)\zeta \left[\frac{\partial w_3}{\partial \eta} w_4 + w_3 \frac{\partial w_4}{\partial \eta} \right], \tag{A.59}$$

$$\frac{\partial N_{21}}{\partial \zeta} = 2(2\zeta - 1)w_3 w_4 \ .$$

$$\frac{\partial N_{22}}{\partial \xi} = 2(\zeta - 1)\zeta \left[\frac{\partial w_4}{\partial \xi} w_5 + w_4 \frac{\partial w_5}{\partial \xi} \right],$$

$$\frac{\partial N_{22}}{\partial \eta} = 2(\zeta - 1)\zeta \left[\frac{\partial w_4}{\partial \eta} w_5 + w_4 \frac{\partial w_5}{\partial \eta} \right], \tag{A.60}$$

$$\frac{\partial N_{22}}{\partial \zeta} = 2(2\zeta - 1)w_4 w_5 \ .$$

$$\frac{\partial N_{23}}{\partial \xi} = 2(\zeta - 1)\zeta \left[\frac{\partial w_5}{\partial \xi} w_6 + w_5 \frac{\partial w_6}{\partial \xi} \right],$$

$$\frac{\partial N_{23}}{\partial \eta} = 2(\zeta - 1)\zeta \left[\frac{\partial w_5}{\partial \eta} w_6 + w_5 \frac{\partial w_6}{\partial \eta} \right], \tag{A.61}$$

$$\frac{\partial N_{23}}{\partial \zeta} = 2(2\zeta - 1)w_5 w_6 \ .$$

$$\frac{\partial N_{24}}{\partial \xi} = 2(\zeta - 1)\zeta \left[\frac{\partial w_1}{\partial \xi} w_6 + w_1 \frac{\partial w_6}{\partial \xi} \right],$$

$$\frac{\partial N_{24}}{\partial \eta} = 2(\zeta - 1)\zeta \left[\frac{\partial w_1}{\partial \eta} w_6 + w_1 \frac{\partial w_6}{\partial \eta} \right], \tag{A.62}$$

$$\frac{\partial N_{24}}{\partial \zeta} = 2(2\zeta - 1)w_1 w_6 \ .$$

$$\frac{\partial N_{25}}{\partial \xi} = -\frac{\sqrt{3}}{3}\frac{1-\zeta^2}{18(\xi^2+\eta^2-3)^2}\Big\{-4\sqrt{3}\xi^5 + \xi^4(6\eta-9) - 8\sqrt{3}\xi^3(\eta^2-3)$$

$$+ 18\xi^2(2\eta^3 - \eta^2 - 5\eta + 3) + 12\sqrt{3}\xi(\eta^4 + 4\eta^3 - \eta^2 - 9\eta - 3)$$

$$- 9(\eta+1)^2(2\eta^3 - 3\eta^2 - 6\eta + 9)\Big\},$$

$$\frac{\partial N_{25}}{\partial \eta} = -\frac{\sqrt{3}}{3}\frac{(1-\zeta^2)(2\xi+\sqrt{3})}{18(\xi^2+\eta^2-3)^2}\Big\{3\xi^4 + 2\sqrt{3}\xi^3(4\eta+3) - 6\xi^2\eta(5\eta+2) \tag{A.63}$$

$$- 6\sqrt{3}\xi(\eta^2+4\eta+3) - 9(\eta^4 - 8\eta^2 - 4\eta + 3)\Big\},$$

$$\frac{\partial N_{25}}{\partial \xi} = -\frac{\sqrt{3}}{3}\Big(\frac{\xi}{\sqrt{3}} - \eta + 1\Big)\frac{(\xi+\frac{\sqrt{3}}{2})(-\frac{\xi}{\sqrt{3}}-\eta-1)(\frac{\xi}{\sqrt{3}}-\eta-1)}{\xi^2+\eta^2-3}(-2\xi)\ .$$

$$\frac{\partial N_{26}}{\partial \xi} = -\frac{2(1-\zeta^2)}{3}\Bigg\{\frac{\xi\Big[2\xi^4 + 4\xi^2(\eta^2-3) + 3(-2\eta^4 - 4\eta^3 + 2\eta^2 + 9\eta + 6)\Big]}{3(\xi^2+\eta^2-3)^2}\Bigg\},$$

$$\frac{\partial N_{26}}{\partial \eta} = -\frac{2(1-\zeta^2)}{3}\Bigg\{\frac{(\sqrt{3}-2\xi)(2\xi+\sqrt{3})\Big[\xi^2(4\eta+3) - 3(\eta^2+4\eta+3)\Big]}{6(\xi^2+\eta^2-3)^2}\Bigg\}, \tag{A.64}$$

$$\frac{\partial N_{26}}{\partial \zeta} = \frac{2}{3}(-2\zeta)\frac{(\xi+\frac{\sqrt{3}}{2})(-\frac{\xi}{\sqrt{3}}-\eta-1)(\frac{\xi}{\sqrt{3}}-\eta-1)(\xi-\frac{\sqrt{3}}{2})}{\xi^2+\eta^2-3}\ .$$

$$\frac{\partial N_{27}}{\partial \xi} = \frac{\sqrt{3}(1-\zeta^2)}{54(\xi^2+\eta^2-3)^2}\Big\{4\sqrt{3}\xi^5 + \xi^4(6\eta-9) + 8\sqrt{3}\xi^3(\eta^2-3)$$

$$+ 18\xi^2(2\eta^3 - \eta^2 - 5\eta + 3)$$

$$- 12\sqrt{3}\xi(\eta^4 + 4\eta^3 - \eta^2 - 9\eta - 3) - 9(\eta+1)^2(2\eta^3 - 3\eta^2 - 6\eta + 9)\Big\},$$

$$\frac{\partial N_{27}}{\partial \eta} = \frac{\sqrt{3}}{3}\frac{(1-\zeta^2)(\sqrt{3}-2\xi)}{18(\xi^2+\eta^2-3)^2}\Big\{-3\xi^4 + 2\sqrt{3}\xi^3(4\eta+3) + 6\xi^2\eta(5\eta+2) \tag{A.65}$$

$$- 6\sqrt{3}\xi(\eta^2+4\eta+3) + 9(\eta^4 - 8\eta^2 - 4\eta + 3)\Big\},$$

$$\frac{\partial N_{27}}{\partial \zeta} = \frac{\sqrt{3}}{3}(-2\zeta)\frac{(-\frac{\xi}{\sqrt{3}}-\eta-1)(\frac{\xi}{\sqrt{3}}-\eta-1)(\xi-\frac{\sqrt{3}}{2})(-\frac{\xi}{\sqrt{3}}-\eta+1)}{\xi^2+\eta^2-3}\ .$$

$$\frac{\partial N_{28}}{\partial \xi} = -\frac{\sqrt{3}(1-\zeta^2)}{54(\xi^2 + \eta^2 - 3)^2}\Big\{ -4\sqrt{3}\xi^5 + \xi^4(6\eta + 9) - 8\sqrt{3}\xi^3(\eta^2 - 3)$$

$$+ 18\xi^2(2\eta^3 + \eta^2 - 5\eta - 3)$$

$$+ 12\sqrt{3}\xi(\eta^4 - 4\eta^3 - \eta^2 + 9\eta - 3) - 9(\eta - 1)^2(2\eta^3 + 3\eta^2 - 6\eta - 9)\Big\},$$

$$\frac{\partial N_{28}}{\partial \eta} = \frac{\sqrt{3}}{3}\frac{(1-\zeta^2)(\sqrt{3}-2\xi)}{18(\xi^2 + \eta^2 - 3)^2}\Big\{ 3\xi^4 + 2\sqrt{3}\xi^3(4\eta - 3) - 6\xi^2\eta(5\eta - 2)$$

$$+ 6\sqrt{3}(\eta^2 - 4\eta + 3) - 9(\eta^4 - 8\eta^2 + 4\eta + 3)\Big\},$$

$$\frac{\partial N_{28}}{\partial \zeta} = \frac{\sqrt{3}}{3}(2\zeta)\frac{\left(\frac{\xi}{\sqrt{3}} - \eta - 1\right)\left(\xi - \frac{\sqrt{3}}{2}\right)\left(-\frac{\xi}{\sqrt{3}} - \eta + 1\right)\left(\frac{\xi}{\sqrt{3}} - \eta + 1\right)}{\xi^2 + \eta^2 - 3} .$$

(A.66)

$$\frac{\partial N_{29}}{\partial \xi} = \frac{2}{3}(1-\zeta^2)\Big\{ -\frac{\xi\left[2\xi^4 + 4\xi^2(\eta^2 - 3) + 3(-2\eta^4 + 4\eta^3 + 2\eta^2 - 9\eta + 6)\right]}{3(\xi^2 + \eta^2 - 3)^2}\Big\},$$

$$\frac{\partial N_{29}}{\partial \eta} = \frac{2}{3}(1-\zeta^2)\Big\{ -\frac{(\sqrt{3}-2\xi)(2\xi + \sqrt{3})(\xi^2(4\eta - 3) + 3(\eta^2 - 4\eta + 3))}{6(\xi^2 + \eta^2 - 3)^2}\Big\},$$

(A.67)

$$\frac{\partial N_{29}}{\partial \zeta} = \frac{2}{3}(-2\zeta)\frac{\left(\xi - \frac{\sqrt{3}}{2}\right)\left(-\frac{\xi}{\sqrt{3}} - \eta + 1\right)\left(\frac{\xi}{\sqrt{3}} - \eta + 1\right)\left(\xi + \frac{\sqrt{3}}{2}\right)}{\xi^2 + \eta^2 - 3} .$$

$$\frac{\partial N_{30}}{\partial \xi} = \frac{\sqrt{3}}{3}\frac{1-\zeta^2}{18(\xi^2 + \eta^2 - 3)^2}\Big\{ 4\sqrt{3}\xi^5 + \xi^4(6\eta + 9) + 8\sqrt{3}\xi^3(\eta^2 - 3) + 18\xi^2(2\eta^3 + \eta^2 - 5\eta - 3)$$

$$- 12\sqrt{3}\xi(\eta^4 - 4\eta^3 - \eta^2 + 9\eta - 3) - 9(\eta - 1)^2(2\eta^3 + 3\eta^2 - 6\eta - 9)\Big\},$$

$$\frac{\partial N_{30}}{\partial \eta} = -\frac{\sqrt{3}}{3}\frac{(1-\zeta^2)(2\xi + \sqrt{3})}{18(\xi^2 + \eta^2 - 3)^2}\Big\{ -3\xi^4 + 2\sqrt{3}\xi^3(4\eta - 3) + 6\xi^2\eta(5\eta - 2)$$

$$+ 6\sqrt{3}\xi(\eta^2 - 4\eta + 3) + 9(\eta^4 - 8\eta^2 + 4\eta + 3)\Big\},$$

$$\frac{\partial N_{30}}{\partial \zeta} = \frac{\sqrt{3}}{3}(-2\zeta)\frac{\left(-\frac{\xi}{\sqrt{3}} - \eta + 1\right)\left(\frac{\xi}{\sqrt{3}} - \eta + 1\right)\left(\xi + \frac{\sqrt{3}}{2}\right)\left(-\frac{\xi}{\sqrt{3}} - \eta - 1\right)}{\xi^2 + \eta^2 - 3} .$$

(A.68)

Appendix B

Lattice Rotation and Projection Operator

To capture the anisotropic feature of crystal plasticity, we need a lattice rotation and projection operator in computations[76], so that we can rotate a given vector $\mathbf{v} = (x, y, z)$ about an arbitrary axis with direction vector $\hat{\boldsymbol{r}}$ by a finite angle θ based on the specific crystal orientation as shown in Fig. B.1(a).

In this Appendix, we show that such operation can be written as the product of a matrix $\mathbb{R}$ and the vector $[\boldsymbol{v}]$, i.e. $\mathbb{R}[\boldsymbol{v}]$.

Firstly, we decompose $\mathbf{v}$ into two components:

$$\mathbf{v} = \mathbf{v}_{\parallel} + \mathbf{v}_{\perp}$$

where $\mathbf{v}_{\parallel}$ is parallel to $\hat{\boldsymbol{r}}$ and $\mathbf{v}_{\perp}$ is perpendicular to $\hat{\boldsymbol{r}}$.

Therefore, we have following relations,

$$\mathbf{v}_{\parallel} = \frac{\mathbf{v} \cdot \hat{\boldsymbol{r}}}{|\hat{r}|^2} \hat{\boldsymbol{r}} = (\mathbf{v} \cdot \hat{\boldsymbol{r}})\hat{\boldsymbol{r}}, \quad and \quad \mathbf{v}_{\perp} = \mathbf{v} - (\mathbf{v} \cdot \hat{\boldsymbol{r}})\hat{\boldsymbol{r}} \ .$$

Considering the fact that

$$\mathbf{v} = \mathbf{v}_{\parallel} + \mathbf{v}_{\perp}$$

we can have the following relation based on linearity of operator T,

$$T(\mathbf{v}) = T(\mathbf{v}_{\parallel} + \mathbf{v}_{\perp}) = T(\mathbf{v}_{\parallel}) + T(\mathbf{v}_{\perp})$$

Due to the fact that $\mathbf{v}_{\parallel}$ is parallel to $\hat{\boldsymbol{r}}$, we have,

$$T(\mathbf{v}_{\parallel}) = \mathbf{v}_{\parallel} \ .$$

Therefore,

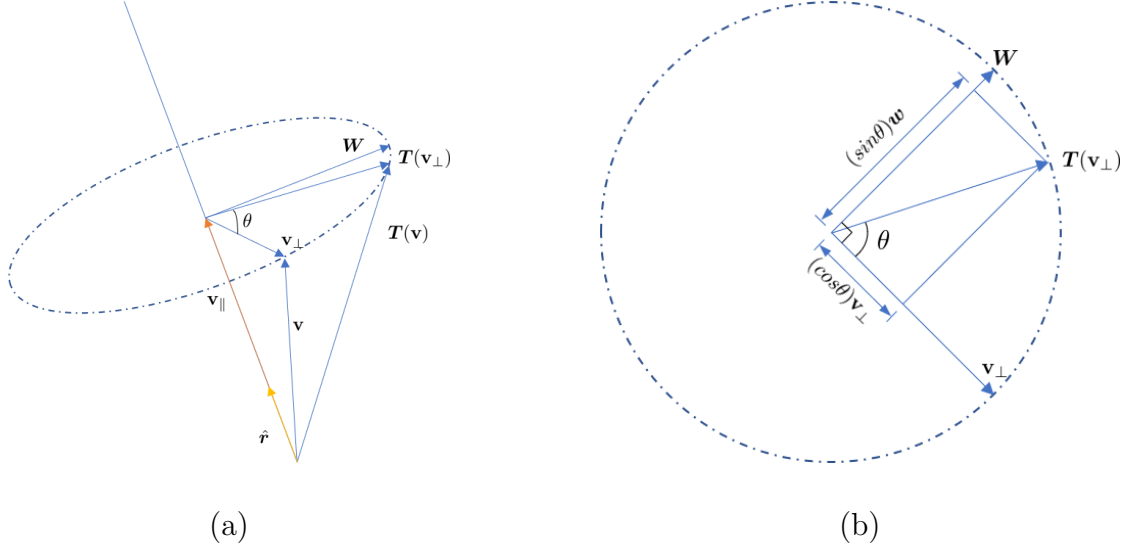$$T(\mathbf{v}) = \mathbf{v}_{\parallel} + T(\mathbf{v}_{\perp})$$

Figure B.1: Rotation about an arbitrary axis: (a) rotation axis and rotation plane; (b) rotated vector on rotation plane.

To calculate $T(\mathbf{v}_\perp)$, the basis in 2D rotation plane is created in Fig.B.1(b),

$$\{\mathbf{v}_\perp, \boldsymbol{w}\}$$

in which,

$$\boldsymbol{w} = \hat{\boldsymbol{r}} \times \mathbf{v}_\perp = \hat{\boldsymbol{r}} \times \mathbf{v}$$

Based on Fig. B.1(b), we see that

$$T(\mathbf{v}_\perp) = \cos\theta \mathbf{v}_\perp + \sin\theta \boldsymbol{w} = \cos\theta \mathbf{v}_\perp + \sin\theta(\hat{\boldsymbol{r}} \times \mathbf{v})$$

and therefore,

$$\begin{aligned}
T(\mathbf{v}) &= \mathbf{v}_\parallel + T(\mathbf{v}_\perp) \\
&= (\mathbf{v} \cdot \hat{\boldsymbol{r}})\hat{\boldsymbol{r}} + \cos\theta \mathbf{v}_\perp + \sin\theta(\hat{\boldsymbol{r}} \times \mathbf{v}) \\
&= (1 - \cos\theta)(\mathbf{v} \cdot \hat{\boldsymbol{r}})\hat{\boldsymbol{r}} + \cos\theta \mathbf{v} + \sin\theta(\hat{\boldsymbol{r}} \times \mathbf{v})
\end{aligned} \tag{B.1}$$

Eq.(B.1) implies that there exists a rotation matrix $\mathbb{R}$ such that $T(\mathbf{v}) = \mathbb{R}\mathbf{v}$. To derive the explicit expression of $\mathbb{R}$, we first need two intermediary results.

Lemma 1 *If* $\mathbf{u} = (u_x, u_y, u_z)$ *and* $\mathbf{v} = (v_x, v_y, v_z)$, *then*

$$\mathbf{u} \times \mathbf{v} = \begin{bmatrix} 0 & -u_z & u_y \\ u_z & 0 & -u_x \\ -u_y & u_x & 0 \end{bmatrix} [\mathbf{v}]$$

Lemma 2 *Using the notation of the previous lemma, we have*

$$(\mathbf{u} \cdot \mathbf{v})\mathbf{u} = \begin{bmatrix} u_x^2 & u_x u_y & u_x u_z \\ u_x u_y & u_y^2 & u_y u_z \\ u_x u_z & u_y u_z & u_z^2 \end{bmatrix} [\boldsymbol{v}]$$

Therefore, we are able to write $T(\mathbf{v})$ as a matrix transformation or multiplication,

$$T(\mathbf{v}) = (1 - \cos\theta)(\mathbf{v} \cdot \hat{\boldsymbol{r}})\hat{\boldsymbol{r}} + \cos\theta \mathbf{v} + \sin\theta(\hat{\boldsymbol{r}} \times \mathbf{v})$$

$$= (1 - \cos\theta) \begin{bmatrix} u_x^2 & u_x u_y & u_x u_z \\ u_x u_y & u_y^2 & u_y u_z \\ u_x u_z & u_y u_z & u_z^2 \end{bmatrix} \mathbf{v} + \begin{bmatrix} 1 & 0 & 0 \\ 0 & 1 & 0 \\ 0 & 0 & 1 \end{bmatrix} \cos\theta \mathbf{v} + \sin\theta \begin{bmatrix} 0 & -u_z & u_y \\ u_z & 0 & -u_x \\ -u_y & u_x & 0 \end{bmatrix} \mathbf{v},$$

$$= \begin{bmatrix} tu_x^2 + C & tu_x u_y - Su_z & tu_x u_z + Su_y \\ tu_x u_y + Su_z & tu_y^2 + C & tu_y u_z - Su_x \\ tu_x u_z - Su_y & tu_y u_z + Su_x & tu_z^2 + C \end{bmatrix}$$

$$(\text{B.2})$$

where

$$\hat{\boldsymbol{r}} = (u_x, u_y, u_z) \qquad C := \cos\theta \qquad S := \sin\theta \qquad t := 1 - \cos\theta \ .$$

Appendix C

Detailed Formulations of Derivative of D_{kk} in Different Process Zones

In this appendix, we will discuss the expanded formulations of derivative of D_{kk} in different process zones.

C.1 Derivative of D_{kk} in 1st-order Process Zone

The first order derivative of D_{kk} in 1st-order process zone is:

$$
\begin{aligned}
\frac{\partial D_{kk}}{\partial \boldsymbol{G}} = \frac{1}{\Omega_0^u} \bigg\{ & F'''(\bar{\rho}) \sum_j \left[\rho'(l_j) \frac{\partial l_j}{\partial \boldsymbol{G}} \right] \cdot \sum_j \left[\rho'(l_j) \frac{r_{jk}}{l_j} \right] \cdot \sum_j \left[\rho'(l_j) \frac{r_{jk}}{l_j} \right] \\
& + 2F''(\bar{\rho}) \sum_j \left[\frac{\partial}{\partial \boldsymbol{G}} (\rho'(l_j) \frac{r_{jk}}{l_j}) \right] \cdot \sum_j \left[\rho'(l_j) \frac{r_{jk}}{l_j} \right] \\
& + F''(\bar{\rho}) \sum_j \left[\rho'(l_j) \frac{\partial l_j}{\partial \boldsymbol{G}} \right] \cdot \sum_j \left[(\rho''(l_j) - \frac{\rho'(l_j)}{l_j})(\frac{r_{jk}}{l_j})^2 + \frac{\rho'(l_j)}{l_j} \right] \\
& + F'(\bar{\rho}) \sum_j \left[\frac{\partial}{\partial \boldsymbol{G}} (\rho''(l_j) - \frac{\rho'(l_j)}{l_j})(\frac{r_{jk}}{l_j})^2 + 2(\rho''(l_j) - \frac{\rho'(l_j)}{l_j})\frac{r_{jk}}{l_j} \frac{\partial}{\partial \boldsymbol{G}}(\frac{r_{jk}}{l_j}) + \frac{\partial}{\partial \boldsymbol{G}}(\frac{\rho'(l_j)}{l_j}) \right] \\
& + \frac{1}{2} \sum_j \left[\frac{\partial}{\partial \boldsymbol{G}} (\phi''(l_j) - \frac{\phi'(l_j)}{l_j})(\frac{r_{jk}}{l_j})^2 + 2(\phi''(l_j) - \frac{\phi'(l_j)}{l_j})\frac{r_{jk}}{l_j} \frac{\partial}{\partial \boldsymbol{G}}(\frac{r_{jk}}{l_j}) + \frac{\partial}{\partial \boldsymbol{G}}(\frac{\phi'(l_j)}{l_j}) \right] \bigg\}
\end{aligned}
$$
$$\text{(C.1)}$$

in which,

$$\frac{\partial F''(\bar{\rho})}{\partial \boldsymbol{G}} = F'''(\bar{\rho}) \sum_j \left[\rho'(l_j) \frac{\boldsymbol{r}_j \otimes \boldsymbol{R}_j \otimes \boldsymbol{R}_j}{2l_j} \right] \tag{C.2}$$

$$\frac{\partial}{\partial \boldsymbol{G}} (\rho'(l_j) \frac{r_{jk}}{l_j}) = \rho''(l_j) \frac{\partial l_j}{\partial \boldsymbol{G}} \frac{r_{jk}}{l_j} + \rho'(l_j) \frac{\partial}{\partial \boldsymbol{G}} (\frac{r_{jk}}{l_j})$$

$$= \rho''(l_j) \frac{r_{jk}}{l_j} \frac{\boldsymbol{r}_j \otimes \boldsymbol{R}_j \otimes \boldsymbol{R}_j}{2l_j} + \rho'(l_j) \left[\frac{1}{l_j} \frac{\partial r_{jk}}{\partial \boldsymbol{G}} - \frac{r_{jk}}{l_j^2} \frac{\boldsymbol{r}_j \otimes \boldsymbol{R}_j \otimes \boldsymbol{R}_j}{2l_j} \right] \tag{C.3}$$

$$\frac{\partial F'(\bar{\rho})}{\partial \boldsymbol{G}} = F''(\bar{\rho}) \sum_j \left[\rho'(l_j) \frac{\boldsymbol{r}_j \otimes \boldsymbol{R}_j \otimes \boldsymbol{R}_j}{2l_j} \right] \tag{C.4}$$

$$\frac{\partial}{\partial \boldsymbol{G}} (\rho''(l_j) - \frac{\rho'(l_j)}{l_j}) = \left[\rho'''(l_j) - \frac{\rho''(l_j)}{l_j} + \frac{\rho'(l_j)}{l_j^2} \right] \frac{\boldsymbol{r}_j \otimes \boldsymbol{R}_j \otimes \boldsymbol{R}_j}{2l_j} \tag{C.5}$$

$$\frac{\partial}{\partial \boldsymbol{G}} (\frac{r_{jk}}{l_j}) = \frac{1}{l_j} \frac{\partial r_{jk}}{\partial \boldsymbol{G}} - \frac{r_{jk}}{l_j^2} \frac{\boldsymbol{r}_j \otimes \boldsymbol{R}_j \otimes \boldsymbol{R}_j}{2l_j} \tag{C.6}$$

$$\frac{\partial}{\partial \boldsymbol{G}} (\frac{\rho'(l_j)}{l_j}) = (\frac{\rho''(l_j)}{l_j} - \frac{\rho'(l_j)}{l_j^2}) \frac{\boldsymbol{r}_j \otimes \boldsymbol{R}_j \otimes \boldsymbol{R}_j}{2l_j} \tag{C.7}$$

$$\frac{\partial}{\partial \boldsymbol{G}} (\phi''(l_j) - \frac{\phi'(l_j)}{l_j}) = \left[\phi'''(l_j) - \frac{\phi''(l_j)}{l_j} + \frac{\phi'(l_j)}{l_j^2} \right] \frac{\boldsymbol{r}_j \otimes \boldsymbol{R}_j \otimes \boldsymbol{R}_j}{2l_j} \tag{C.8}$$

$$\frac{\partial}{\partial \boldsymbol{G}} (\frac{\phi'(l_j)}{l_j}) = (\frac{\phi''(l_j)}{l_j} - \frac{\phi'(l_j)}{l_j^2}) \frac{\boldsymbol{r}_j \otimes \boldsymbol{R}_j \otimes \boldsymbol{R}_j}{2l_j} \tag{C.9}$$

$$\frac{\partial r_{jk}}{\partial \boldsymbol{G}} = \frac{1}{2} \delta_{ik} \boldsymbol{e}_i \otimes \boldsymbol{R}_j \otimes \boldsymbol{R}_j \tag{C.10}$$

$$\frac{\partial l_j}{\partial \boldsymbol{G}} = \frac{1}{2l_j} \frac{\boldsymbol{r}_j \cdot \boldsymbol{r}_j}{\partial \boldsymbol{G}} = \frac{1}{2l_j} \frac{\partial r_m r_m}{\partial G_{nPQ}} \boldsymbol{e}_n \otimes \boldsymbol{E}_P \otimes \boldsymbol{E}_Q$$

$$= \frac{1}{2l_j} (2r_m \frac{\partial r_m}{\partial G_{nPQ}}) \boldsymbol{e}_n \otimes \boldsymbol{E}_P \otimes \boldsymbol{E}_Q$$

$$= \frac{1}{2l_j} \left[2r_m \frac{\partial}{\partial G_{nPQ}} (F_{mA} R_A + \frac{1}{2} G_{mAB} R_A R_B) \right] \boldsymbol{e}_n \otimes \boldsymbol{E}_P \otimes \boldsymbol{E}_Q$$

$$= \frac{1}{2l_j} \left[2r_m \frac{1}{2} \delta_{mn} \delta_{PA} \delta_{QB} R_A R_B \right] \boldsymbol{e}_n \otimes \boldsymbol{E}_P \otimes \boldsymbol{E}_Q$$

$$= \frac{1}{2l_j} r_n R_P R_Q \boldsymbol{e}_n \otimes \boldsymbol{E}_P \otimes \boldsymbol{E}_Q = \frac{\boldsymbol{r}_j \otimes \boldsymbol{R}_j \otimes \boldsymbol{R}_j}{2l_j} \tag{C.11}$$

so that we have the expanded formulation of $\frac{\partial D_{kk}}{\partial \boldsymbol{G}}$:

$$
\begin{aligned}
\frac{\partial D_{kk}}{\partial \boldsymbol{G}} = \frac{1}{\Omega_0^u} \Bigg\{ & F'''(\bar{\rho}) \sum_j \left[\rho'(l_j) \frac{\boldsymbol{r}_j \otimes \boldsymbol{R}_j \otimes \boldsymbol{R}_j}{2l_j} \right] \cdot \sum_j \left[\rho'(l_j) \frac{r_{jk}}{l_j} \right] \cdot \sum_j \left[\rho'(l_j) \frac{r_{jk}}{l_j} \right] \\
& + 2F''(\bar{\rho}) \sum_j \left[\rho''(l_j) \frac{r_{jk}}{l_j} \frac{\boldsymbol{r}_j \otimes \boldsymbol{R}_j \otimes \boldsymbol{R}_j}{2l_j} + \rho'(l_j) \left(\frac{1}{l_j} \frac{\partial r_{jk}}{\partial \boldsymbol{G}} - \frac{r_{jk}}{l_j^2} \frac{\boldsymbol{r}_j \otimes \boldsymbol{R}_j \otimes \boldsymbol{R}_j}{2l_j} \right) \right] \cdot \sum_j \left[\rho'(l_j) \frac{r_{jk}}{l_j} \right] \\
& + F''(\bar{\rho}) \sum_j \left[\rho'(l_j) \frac{\boldsymbol{r}_j \otimes \boldsymbol{R}_j \otimes \boldsymbol{R}_j}{2l_j} \right] \cdot \sum_j \left[(\rho''(l_j) - \frac{\rho'(l_j)}{l_j})(\frac{r_{jk}}{l_j})^2 + \frac{\rho'(l_j)}{l_j} \right] \\
& + F'(\bar{\rho}) \sum_j \Bigg[(\rho'''(l_j) - \frac{\rho''(l_j)}{l_j} + \frac{\rho'(l_j)}{l_j^2}) \frac{\boldsymbol{r}_j \otimes \boldsymbol{R}_j \otimes \boldsymbol{R}_j}{2l_j} (\frac{r_{jk}}{l_j})^2 \\
& \quad + 2(\rho''(l_j) - \frac{\rho'(l_j)}{l_j}) \frac{r_{jk}}{l_j} (\frac{1}{2l_j} \delta_{ik} \boldsymbol{e}_i \otimes \boldsymbol{R}_j \otimes \boldsymbol{R}_j - \frac{r_{jk}}{l_j^2} \frac{\boldsymbol{r}_j \otimes \boldsymbol{R}_j \otimes \boldsymbol{R}_j}{2l_j}) \\
& \quad + (\frac{\rho''(l_j)}{l_j} - \frac{\rho'(l_j)}{l_j^2}) \frac{\boldsymbol{r}_j \otimes \boldsymbol{R}_j \otimes \boldsymbol{R}_j}{2l_j} \Bigg] \\
& + \frac{1}{2} \sum_j \Bigg[(\phi'''(l_j) - \frac{\phi''(l_j)}{l_j} + \frac{\phi'(l_j)}{l_j}) \frac{\boldsymbol{r}_j \otimes \boldsymbol{R}_j \otimes \boldsymbol{R}_j}{2l_j} (\frac{r_{jk}}{l_j})^2 \\
& \quad + 2(\phi''(l_j) - \frac{\phi'(l_j)}{l_j}) \frac{r_{jk}}{l_j} (\frac{1}{2l_j} \delta_{ik} \boldsymbol{e}_i \otimes \boldsymbol{R}_j \otimes \boldsymbol{R}_j - \frac{r_{jk}}{l_j^2} \frac{\boldsymbol{r}_j \otimes \boldsymbol{R}_j \otimes \boldsymbol{R}_j}{2l_j}) \\
& \quad + (\frac{\phi''(l_j)}{l_j} - \frac{\phi'(l_j)}{l_j^2}) \frac{\boldsymbol{r}_j \otimes \boldsymbol{R}_j \otimes \boldsymbol{R}_j}{2l_j} \Bigg] \Bigg\}
\end{aligned}
$$

$$(C.12)$$

C.2 Derivative of D_{kk} in 2nd-order Process Zone

The first order derivative of D_{kk} in 2nd-order process zone is:

$$
\begin{aligned}
\frac{\partial D_{kk}}{\partial \boldsymbol{H}} = \frac{1}{\Omega_0^u} \Bigg\{ & \frac{\partial F''(\bar{\rho})}{\partial \boldsymbol{H}} \cdot \sum_j \left[\rho'(l_j) \frac{r_{jk}}{l_j} \right] \cdot \sum_j \left[\rho'(l_j) \frac{r_{jk}}{l_j} \right] \\
& + 2F''(\bar{\rho}) \sum_j \left[\frac{\partial}{\partial \boldsymbol{H}} (\rho'(l_j) \frac{r_{jk}}{l_j}) \right] \cdot \sum_j \left[\rho'(l_j) \frac{r_{jk}}{l_j} \right] \\
& + \frac{F'(\bar{\rho})}{\partial \boldsymbol{H}} \cdot \sum_j \left[(\rho''(l_j) - \frac{\rho'(l_j)}{l_j})(\frac{r_{jk}}{l_j})^2 + \frac{\rho'(l_j)}{l_j} \right] \\
& + F'(\bar{\rho}) \sum_j \Bigg[\frac{\partial}{\partial \boldsymbol{H}} (\rho''(l_j) - \frac{\rho'(l_j)}{l_j})(\frac{r_{jk}}{l_j})^2 \\
& \qquad + 2(\rho''(l_j) - \frac{\rho'(l_j)}{l_j}) \frac{r_{jk}}{l_j} \frac{\partial}{\partial \boldsymbol{H}} (\frac{r_{jk}}{l_j}) + \frac{\partial}{\partial \boldsymbol{H}} (\frac{\rho'(l_j)}{l_j}) \Bigg] \\
& + \frac{1}{2} \sum_j \Bigg[\frac{\partial}{\partial \boldsymbol{H}} (\phi''(l_j) - \frac{\phi'(l_j)}{l_j})(\frac{r_{jk}}{l_j})^2 \\
& \qquad + 2(\phi''(l_j) - \frac{\phi'(l_j)}{l_j}) \frac{r_{jk}}{l_j} \frac{\partial}{\partial \boldsymbol{H}} (\frac{r_{jk}}{l_j}) + \frac{\partial}{\partial \boldsymbol{H}} (\frac{\phi'(l_j)}{l_j}) \Bigg] \Bigg\}
\end{aligned}
\tag{C.13}
$$

in which,

$$\frac{\partial F''(\bar{\rho})}{\partial \boldsymbol{H}} = F'''(\bar{\rho}) \sum_j \left[\rho'(l_j) \frac{\boldsymbol{r}_j \otimes \boldsymbol{R}_j \otimes \boldsymbol{R}_j \otimes \boldsymbol{R}_j}{6l_j} \right] \tag{C.14}$$

$$\frac{\partial}{\partial \boldsymbol{H}}(\rho'(l_j)\frac{r_{jk}}{l_j}) = \rho''(l_j)\frac{\partial l_j}{\partial \boldsymbol{H}}\frac{r_{jk}}{l_j} + \rho'(l_j)\frac{\partial}{\partial \boldsymbol{H}}(\frac{r_{jk}}{l_j})$$

$$= \rho''(l_j)\frac{r_{jk}}{l_j}\frac{\boldsymbol{r}_j \otimes \boldsymbol{R}_j \otimes \boldsymbol{R}_j \otimes \boldsymbol{R}_j}{6l_j} + \rho'(l_j)\left[\frac{1}{l_j}\frac{\partial r_{jk}}{\partial \boldsymbol{H}} - \frac{r_{jk}}{l_j^2}\frac{\boldsymbol{r}_j \otimes \boldsymbol{R}_j \otimes \boldsymbol{R}_j \otimes \boldsymbol{R}_j}{6l_j}\right] \tag{C.15}$$

$$\frac{\partial F'(\bar{\rho})}{\partial \boldsymbol{H}} = F''(\bar{\rho}) \sum_j \left[\rho'(l_j) \frac{\boldsymbol{r}_j \otimes \boldsymbol{R}_j \otimes \boldsymbol{R}_j \otimes \boldsymbol{R}_j}{6l_j} \right] \tag{C.16}$$

$$\frac{\partial}{\partial \boldsymbol{H}}(\rho''(l_j) - \frac{\rho'(l_j)}{l_j}) = \left[\rho'''(l_j) - \frac{\rho''(l_j)}{l_j} + \frac{\rho'(l_j)}{l_j^2} \right] \frac{\boldsymbol{r}_j \otimes \boldsymbol{R}_j \otimes \boldsymbol{R}_j \otimes \boldsymbol{R}_j}{6l_j} \tag{C.17}$$

$$\frac{\partial}{\partial \boldsymbol{H}}(\frac{r_{jk}}{l_j}) = \frac{1}{l_j}\frac{\partial r_{jk}}{\partial \boldsymbol{H}} - \frac{r_{jk}}{l_j^2}\frac{\boldsymbol{r}_j \otimes \boldsymbol{R}_j \otimes \boldsymbol{R}_j \otimes \boldsymbol{R}_j}{6l_j} \tag{C.18}$$

$$\frac{\partial}{\partial \boldsymbol{H}}(\frac{\rho'(l_j)}{l_j}) = (\frac{\rho''(l_j)}{l_j} - \frac{\rho'(l_j)}{l_j^2})\frac{\boldsymbol{r}_j \otimes \boldsymbol{R}_j \otimes \boldsymbol{R}_j \otimes \boldsymbol{R}_j}{6l_j} \tag{C.19}$$

$$\frac{\partial}{\partial \boldsymbol{H}}(\phi''(l_j) - \frac{\phi'(l_j)}{l_j}) = \left[\phi'''(l_j) - \frac{\phi''(l_j)}{l_j} + \frac{\phi'(l_j)}{l_j^2} \right] \frac{\boldsymbol{r}_j \otimes \boldsymbol{R}_j \otimes \boldsymbol{R}_j \otimes \boldsymbol{R}_j}{6l_j} \tag{C.20}$$

$$\frac{\partial}{\partial \boldsymbol{H}}(\frac{\phi'(l_j)}{l_j}) = (\frac{\phi''(l_j)}{l_j} - \frac{\phi'(l_j)}{l_j^2})\frac{\boldsymbol{r}_j \otimes \boldsymbol{R}_j \otimes \boldsymbol{R}_j \otimes \boldsymbol{R}_j}{6l_j} \tag{C.21}$$

$$\frac{\partial r_{jk}}{\partial \boldsymbol{H}} = \frac{\partial(F_{kA}R_A + \frac{1}{2}G_{kBC}R_BR_C + \frac{1}{6}H_{kDEF}R_DR_ER_F)}{\partial H_{mPQR}}\boldsymbol{e}_m \otimes \boldsymbol{E}_P \otimes \boldsymbol{E}_Q \otimes \boldsymbol{E}_R$$

$$= \frac{1}{6}\delta_{km}\delta_{PD}\delta_{EQ}\delta_{FR}R_DR_ER_F\boldsymbol{e}_m \otimes \boldsymbol{E}_P \otimes \boldsymbol{E}_Q \otimes \boldsymbol{E}_R$$

$$= \frac{1}{6}\delta_{km}\boldsymbol{e}_m \otimes \boldsymbol{R}_j \otimes \boldsymbol{R}_j \otimes \boldsymbol{R}_j \tag{C.22}$$

$$\frac{\partial l_j}{\partial \boldsymbol{H}} = \frac{1}{2l_j}\frac{\partial r_m r_m}{\partial H_{nPQS}}\boldsymbol{e}_n \otimes \boldsymbol{E}_P \otimes \boldsymbol{E}_Q \otimes \boldsymbol{E}_S$$

$$= \frac{1}{2l_j}2r_m\frac{\partial \frac{1}{6}H_{mXYZ}R_XR_YR_Z}{\partial H_{nPQS}}\boldsymbol{e}_n \otimes \boldsymbol{E}_P \otimes \boldsymbol{E}_Q \otimes \boldsymbol{E}_S$$

$$= \frac{1}{2l_j}\frac{1}{3}r_m\delta_{mn}\delta_{XP}\delta_{YQ}\delta_{ZS}R_XR_YR_Z\boldsymbol{e}_n \otimes \boldsymbol{E}_P \otimes \boldsymbol{E}_Q \otimes \boldsymbol{E}_S$$

$$= \frac{1}{2l_j}\frac{1}{3}r_m\delta_{mn}\delta_{XP}\delta_{YQ}\delta_{ZS}R_XR_YR_Z\boldsymbol{e}_n \otimes \boldsymbol{E}_P \otimes \boldsymbol{E}_Q \otimes \boldsymbol{E}_S$$

$$= \frac{\boldsymbol{r}_j \otimes \boldsymbol{R}_j \otimes \boldsymbol{R}_j \otimes \boldsymbol{R}_j}{6l_j} \tag{C.23}$$

so that we have the expanded formulation of $\frac{\partial D_{kk}}{\partial \boldsymbol{H}}$:

$$
\begin{aligned}
\frac{\partial D_{kk}}{\partial \boldsymbol{H}} = \frac{1}{\Omega_0^u} \Bigg\{ & F'''(\bar{\rho}) \sum_j \left[\rho'(l_j) \frac{\boldsymbol{r}_j \otimes \boldsymbol{R}_j \otimes \boldsymbol{R}_j \otimes \boldsymbol{R}_j}{6l_j} \right] \cdot \sum_j \left[\rho'(l_j) \frac{r_{jk}}{l_j} \right] \cdot \sum_j \left[\rho'(l_j) \frac{r_{jk}}{l_j} \right] \\
& + 2F''(\bar{\rho}) \sum_j \left[\rho''(l_j) \frac{r_{jk}}{l_j} \frac{\boldsymbol{r}_j \otimes \boldsymbol{R}_j \otimes \boldsymbol{R}_j \otimes \boldsymbol{R}_j}{6l_j} \right. \\
& \left. + \rho'(l_j) \left(\frac{1}{6l_j} \delta_{km} \boldsymbol{e}_m \otimes \boldsymbol{R}_j \otimes \boldsymbol{R}_j \otimes \boldsymbol{R}_j - \frac{r_{jk}}{l_j^2} \frac{\boldsymbol{r}_j \otimes \boldsymbol{R}_j \otimes \boldsymbol{R}_j \otimes \boldsymbol{R}_j}{6l_j} \right) \right] \cdot \sum_j \left[\rho'(l_j) \frac{r_{jk}}{l_j} \right] \\
& + F''(\bar{\rho}) \sum_j \left[\rho'(l_j) \frac{\boldsymbol{r}_j \otimes \boldsymbol{R}_j \otimes \boldsymbol{R}_j \otimes \boldsymbol{R}_j}{6l_j} \right] \cdot \sum_j \left[(\rho''(l_j) - \frac{\rho'(l_j)}{l_j})(\frac{r_{jk}}{l_j})^2 + \frac{\rho'(l_j)}{l_j} \right] \\
& + F'(\bar{\rho}) \sum_j \left[(\rho'''(l_j) - \frac{\rho''(l_j)}{l_j} + \frac{\rho'(l_j)}{l_j^2}) \frac{\boldsymbol{r}_j \otimes \boldsymbol{R}_j \otimes \boldsymbol{R}_j \otimes \boldsymbol{R}_j}{6l_j} (\frac{r_{jk}}{l_j})^2 \right. \\
& + 2(\rho''(l_j) - \frac{\rho'(l_j)}{l_j}) \frac{r_{jk}}{l_j} (\frac{1}{6l_j} \delta_{km} \boldsymbol{e}_m \otimes \boldsymbol{R}_j \otimes \boldsymbol{R}_j \otimes \boldsymbol{R}_j - \frac{r_{jk}}{l_j^2} \frac{\boldsymbol{r}_j \otimes \boldsymbol{R}_j \otimes \boldsymbol{R}_j \otimes \boldsymbol{R}_j}{6l_j}) \\
& \left. + (\frac{\rho''(l_j)}{l_j} - \frac{\rho'(l_j)}{l_j^2}) \frac{\boldsymbol{r}_j \otimes \boldsymbol{R}_j \otimes \boldsymbol{R}_j \otimes \boldsymbol{R}_j}{6l_j} \right] \\
& + \frac{1}{2} \sum_j \left[(\phi'''(l_j) - \frac{\phi''(l_j)}{l_j} + \frac{\phi'(l_j)}{l_j^2}) \frac{\boldsymbol{r}_j \otimes \boldsymbol{R}_j \otimes \boldsymbol{R}_j \otimes \boldsymbol{R}_j}{6l_j} (\frac{r_{jk}}{l_j})^2 \right. \\
& + 2(\phi''(l_j) - \frac{\phi'(l_j)}{l_j}) \frac{r_{jk}}{l_j} (\frac{1}{6l_j} \delta_{km} \boldsymbol{e}_m \otimes \boldsymbol{R}_j \otimes \boldsymbol{R}_j \otimes \boldsymbol{R}_j - \frac{r_{jk}}{l_j} \frac{\boldsymbol{r}_j \otimes \boldsymbol{R}_j \otimes \boldsymbol{R}_j \otimes \boldsymbol{R}_j}{6l_j}) \\
& \left. + (\frac{\phi''(l_j)}{l_j} - \frac{\phi'(l_j)}{l_j^2}) \frac{\boldsymbol{r}_j \otimes \boldsymbol{R}_j \otimes \boldsymbol{R}_j \otimes \boldsymbol{R}_j}{6l_j} \right] \Bigg\}
\end{aligned}
$$

$$(C.24)$$

C.3   Derivative of D_{kk} in 3rd-order Process Zone

The first order derivative of D_{kk} in 3rd-order process zone is:

$$
\begin{aligned}
\frac{\partial D_{kk}}{\partial \boldsymbol{K}} = \frac{1}{\Omega_0^u} \Bigg\{ & \frac{\partial F''(\bar{\rho})}{\partial \boldsymbol{K}} \cdot \sum_j \left[\rho'(l_j) \frac{r_{jk}}{l_j} \right] \cdot \sum_j \left[\rho'(l_j) \frac{r_{jk}}{l_j} \right] \\
& + 2F''(\bar{\rho}) \sum_j \left[\frac{\partial}{\partial \boldsymbol{K}} (\rho'(l_j) \frac{r_{jk}}{l_j}) \right] \cdot \sum_j \left[\rho'(l_j) \frac{r_{jk}}{l_j} \right] \\
& + \frac{F'(\bar{\rho})}{\partial \boldsymbol{K}} \cdot \sum_j \left[(\rho''(l_j) - \frac{\rho'(l_j)}{l_j})(\frac{r_{jk}}{l_j})^2 + \frac{\rho'(l_j)}{l_j} \right] \\
& + F'(\bar{\rho}) \sum_j \left[\frac{\partial}{\partial \boldsymbol{K}} (\rho''(l_j) - \frac{\rho'(l_j)}{l_j})(\frac{r_{jk}}{l_j})^2 \right. \\
& \left. \qquad + 2(\rho''(l_j) - \frac{\rho'(l_j)}{l_j})\frac{r_{jk}}{l_j} \frac{\partial}{\partial \boldsymbol{K}}(\frac{r_{jk}}{l_j}) + \frac{\partial}{\partial \boldsymbol{K}}(\frac{\rho'(l_j)}{l_j}) \right] \\
& + \frac{1}{2} \sum_j \left[\frac{\partial}{\partial \boldsymbol{K}} (\phi''(l_j) - \frac{\phi'(l_j)}{l_j})(\frac{r_{jk}}{l_j})^2 \right. \\
& \left. \qquad + 2(\phi''(l_j) - \frac{\phi'(l_j)}{l_j})\frac{r_{jk}}{l_j} \frac{\partial}{\partial \boldsymbol{K}}(\frac{r_{jk}}{l_j}) + \frac{\partial}{\partial \boldsymbol{K}}(\frac{\phi'(l_j)}{l_j}) \right] \Bigg\}
\end{aligned}
\tag{C.25}
$$

in which,

$$\frac{\partial F''(\bar{\rho})}{\partial \boldsymbol{K}} = F'''(\bar{\rho}) \sum_j \left[\rho'(l_j) \frac{\boldsymbol{r}_j \otimes \boldsymbol{R}_j \otimes \boldsymbol{R}_j \otimes \boldsymbol{R}_j \otimes \boldsymbol{R}_j}{24 l_j} \right] \tag{C.26}$$

$$\frac{\partial}{\partial \boldsymbol{K}}(\rho'(l_j) \frac{r_{jk}}{l_j}) = \rho''(l_j) \frac{\partial l_j}{\partial \boldsymbol{K}} \frac{r_{jk}}{l_j} + \rho'(l_j) \frac{\partial}{\partial \boldsymbol{K}}(\frac{r_{jk}}{l_j})$$
$$= \rho''(l_j) \frac{r_{jk}}{l_j} \frac{\boldsymbol{r}_j \otimes \boldsymbol{R}_j \otimes \boldsymbol{R}_j \otimes \boldsymbol{R}_j \otimes \boldsymbol{R}_j}{24 l_j}$$
$$+ \rho'(l_j) \left[\frac{1}{l_j} \frac{\partial r_{jk}}{\partial \boldsymbol{K}} - \frac{r_{jk}}{l_j^2} \frac{\boldsymbol{r}_j \otimes \boldsymbol{R}_j \otimes \boldsymbol{R}_j \otimes \boldsymbol{R}_j \otimes \boldsymbol{R}_j}{24 l_j} \right] \tag{C.27}$$

$$\frac{\partial F'(\bar{\rho})}{\partial \boldsymbol{K}} = F''(\bar{\rho}) \sum_j \left[\rho'(l_j) \frac{\boldsymbol{r}_j \otimes \boldsymbol{R}_j \otimes \boldsymbol{R}_j \otimes \boldsymbol{R}_j \otimes \boldsymbol{R}_j}{24 l_j} \right] \tag{C.28}$$

$$\frac{\partial}{\partial \boldsymbol{K}}(\rho''(l_j) - \frac{\rho''(l_j)}{l_j}) = \left[\rho'''(l_j) - \frac{\rho''(l_j)}{l_j} + \frac{\rho'(l_j)}{l_j^2} \right] \frac{\boldsymbol{r}_j \otimes \boldsymbol{R}_j \otimes \boldsymbol{R}_j \otimes \boldsymbol{R}_j \otimes \boldsymbol{R}_j}{24 l_j} \tag{C.29}$$

$$\frac{\partial}{\partial \boldsymbol{K}}(\frac{r_{jk}}{l_j}) = \frac{1}{l_j} \frac{\partial r_{jk}}{l_j} - \frac{r_{jk}}{l_j^2} \frac{\boldsymbol{r}_j \otimes \boldsymbol{R}_j \otimes \boldsymbol{R}_j \otimes \boldsymbol{R}_j \otimes \boldsymbol{R}_j}{24 l_j} \tag{C.30}$$

$$\frac{\partial}{\partial \boldsymbol{K}}(\frac{\rho'(l_j)}{l_j}) = (\frac{\rho''(l_j)}{l_j} - \frac{\rho'(l_j)}{l_j^2}) \frac{\boldsymbol{r}_j \otimes \boldsymbol{R}_j \otimes \boldsymbol{R}_j \otimes \boldsymbol{R}_j \otimes \boldsymbol{R}_j}{24 l_j} \tag{C.31}$$

$$\frac{\partial}{\partial \boldsymbol{K}}(\phi''(l_j) - \frac{\phi'(l_j)}{l_j}) = (\phi'''(l_j) - \frac{\phi''(l_j)}{l_j} + \frac{\phi'(l_j)}{l_j^2}) \frac{\boldsymbol{r}_j \otimes \boldsymbol{R}_j \otimes \boldsymbol{R}_j \otimes \boldsymbol{R}_j \otimes \boldsymbol{R}_j}{24 l_j} \tag{C.32}$$

$$\frac{\partial}{\partial \boldsymbol{H}}(\frac{\phi'(l_j)}{l_j}) = (\frac{\phi''(l_j)}{l_j} - \frac{\phi'(l_j)}{l_j^2}) \frac{\boldsymbol{r}_j \otimes \boldsymbol{R}_j \otimes \boldsymbol{R}_j \otimes \boldsymbol{R}_j \otimes \boldsymbol{R}_j}{24 l_j} \tag{C.33}$$

$$\frac{\partial r_{jk}}{\partial \boldsymbol{K}} = \frac{\partial(F_{kA} R_A + \frac{1}{2} G_{kBC} R_B R_C + \frac{1}{6} H_{kDEF} R_D R_E R_F + \frac{1}{24} K_{kWXYZ} R_W R_X R_Y R_Z)}{\partial K_{mPQRS}}$$
$$\boldsymbol{e}_m \otimes \boldsymbol{E}_P \otimes \boldsymbol{E}_Q \otimes \boldsymbol{E}_R \otimes \boldsymbol{E}_S$$
$$= \frac{1}{24} \delta_{km} \delta_{WP} \delta_{XQ} \delta_{YR} \delta_{ZS} R_W R_X R_Y R_Z \boldsymbol{e}_m \otimes \boldsymbol{E}_P \otimes \boldsymbol{E}_Q \otimes \boldsymbol{E}_R \otimes \boldsymbol{E}_S$$
$$= \frac{1}{24} \delta_{km} \boldsymbol{e}_m \otimes \boldsymbol{R}_j \otimes \boldsymbol{R}_j \otimes \boldsymbol{R}_j \otimes \boldsymbol{R}_j \tag{C.34}$$

$$\frac{\partial l_j}{\partial \boldsymbol{K}} = \frac{1}{2l_j} \frac{\partial r_m r_m}{\partial K_{nPQRS}} \boldsymbol{e}_n \otimes \boldsymbol{E}_P \otimes \boldsymbol{E}_Q \otimes \boldsymbol{E}_R \otimes \boldsymbol{E}_S$$
$$= \frac{1}{2l_j} 2 r_m \frac{\partial \frac{1}{24} K_{mWXYZ} R_W R_X R_Y R_Z}{\partial K_{nPQRS}} \boldsymbol{e}_n \otimes \boldsymbol{E}_P \otimes \boldsymbol{E}_Q \otimes \boldsymbol{E}_R \otimes \boldsymbol{E}_S$$
$$= \frac{1}{24 l_j} r_m \delta_{mn} \delta_{WP} \delta_{XQ} \delta_{YR} \delta_{ZS} R_W R_X R_Y R_Z \boldsymbol{e}_n \otimes \boldsymbol{E}_P \otimes \boldsymbol{E}_Q \otimes \boldsymbol{E}_R \boldsymbol{E}_S$$
$$= \frac{\boldsymbol{r}_j \otimes \boldsymbol{R}_j \otimes \boldsymbol{R}_j \otimes \boldsymbol{R}_j \otimes \boldsymbol{R}_j}{24 l_j} \tag{C.35}$$

so that we have the expanded formulation of $\frac{\partial D_{kk}}{\partial \boldsymbol{K}}$:

$$
\begin{aligned}
\frac{\partial D_{kk}}{\partial \boldsymbol{K}} = \frac{1}{\Omega_0^u} \Bigg\{ & F'''(\bar{\rho}) \sum_j \left[\rho'(l_j) \frac{\boldsymbol{r}_j \otimes \boldsymbol{R}_j \otimes \boldsymbol{R}_j \otimes \boldsymbol{R}_j \otimes \boldsymbol{R}_j}{24 l_j} \right] \cdot \sum_j \left[\rho'(l_j) \frac{r_{jk}}{l_j} \right] \cdot \sum_j \left[\rho'(l_j) \frac{r_{jk}}{l_j} \right] \\
& + 2 F''(\bar{\rho}) \sum_j \left[\rho''(l_j) \frac{r_{jk}}{l_j} \frac{\boldsymbol{r}_j \otimes \boldsymbol{R}_j \otimes \boldsymbol{R}_j \otimes \boldsymbol{R}_j \otimes \boldsymbol{R}_j}{24 l_j} \right. \\
& + \rho'(l_j) \left(\frac{1}{l_j} \frac{\partial r_{jk}}{\partial \boldsymbol{K}} - \frac{r_{jk}}{l_j^2} \frac{\boldsymbol{r}_j \otimes \boldsymbol{R}_j \otimes \boldsymbol{R}_j \otimes \boldsymbol{R}_j \otimes \boldsymbol{R}_j}{24 l_j} \right) \Bigg] \cdot \sum_j \left[\rho'(l_j) \frac{r_{jk}}{l_j} \right] \\
& + F''(\bar{\rho}) \sum_j \left[\rho'(l_j) \frac{\boldsymbol{r}_j \otimes \boldsymbol{R}_j \otimes \boldsymbol{R}_j \otimes \boldsymbol{R}_j \otimes \boldsymbol{R}_j}{24 l_j} \right] \cdot \sum_j \left[(\rho''(l_j) - \frac{\rho'(l_j)}{l_j})(\frac{r_{jk}}{l_j})^2 + \frac{\rho'(l_j)}{l_j} \right] \\
& + F'(\bar{\rho}) \sum_j \left[(\rho'''(l_j) - \frac{\rho''(l_j)}{l_j} + \frac{\rho'(l_j)}{l_j^2}) \frac{\boldsymbol{r}_j \otimes \boldsymbol{R}_j \otimes \boldsymbol{R}_j \otimes \boldsymbol{R}_j \otimes \boldsymbol{R}_j}{24 l_j} (\frac{r_{jk}}{l_j})^2 \right. \\
& + 2(\rho''(l_j) - \frac{\rho'(l_j)}{l_j}) \frac{r_{jk}}{l_j} (\frac{1}{24 l_j} \delta_{km} \boldsymbol{e}_m \otimes \boldsymbol{R}_j \otimes \boldsymbol{R}_j \otimes \boldsymbol{R}_j \otimes \boldsymbol{R}_j - \frac{r_{jk}}{l_j^2} \frac{\boldsymbol{r}_j \otimes \boldsymbol{R}_j \otimes \boldsymbol{R}_j \otimes \boldsymbol{R}_j}{24 l_j}) \\
& + (\frac{\rho''(l_j)}{l_j} - \frac{\rho'(l_j)}{l_j^2}) \frac{\boldsymbol{r}_j \otimes \boldsymbol{R}_j \otimes \boldsymbol{R}_j \otimes \boldsymbol{R}_j \otimes \boldsymbol{R}_j}{24 l_j} \Bigg] \\
& + \frac{1}{2} \sum_j \left[(\phi'''(l_j) - \frac{\phi''(l_j)}{l_j} + \frac{\phi'(l_j)}{l_j^2}) \frac{\boldsymbol{r}_j \otimes \boldsymbol{R}_j \otimes \boldsymbol{R}_j \otimes \boldsymbol{R}_j \otimes \boldsymbol{R}_j}{24 l_j} (\frac{r_{jk}}{l_j})^2 \right. \\
& + 2(\phi''(l_j) - \frac{\phi'(l_j)}{l_j}) \frac{r_{jk}}{l_j} (\frac{1}{24 l_j} \delta_{km} \boldsymbol{e}_m \otimes \boldsymbol{R}_j \otimes \boldsymbol{R}_j \otimes \boldsymbol{R}_j \otimes \boldsymbol{R}_j - \frac{r_{jk}}{l_j^2} \frac{\boldsymbol{r}_j \otimes \boldsymbol{R}_j \otimes \boldsymbol{R}_j \otimes \boldsymbol{R}_j \otimes \boldsymbol{R}_j}{24 l_j}) \\
& + (\frac{\phi''(l_j)}{l_j} - \frac{\phi'(l_j)}{l_j^2}) \frac{\boldsymbol{r}_j \otimes \boldsymbol{R}_j \otimes \boldsymbol{R}_j \otimes \boldsymbol{R}_j \otimes \boldsymbol{R}_j}{24 l_j} \Bigg] \Bigg\}
\end{aligned}
$$

$$(\text{C.36})$$

Appendix D

Crystal Lattice-informed MCDD Model Mesh on FCC Crystals

D.1 Dual Lattice Tessellation on FCC Crystals

The crystal lattice-based Finite Element mesh of MCDD model can also be applied on Face-centered Cubic (FCC) crystals. Different from Body-centered Cubic (BCC) crystals, FCC crystal has the most close-packed plane, i.e. {111}. Therefore, the first nearest atom shell having 12 atoms will be selected as the representative atoms to construct the corresponding Voronoi-Dirichlet Polyhedron (VDP) that is rhombic dodecahedron, which is referred as the unit cell of dual lattice tessellation in FCC crystal structure (see Fig.D.1(b)). The FCC unit cell of crystal lattice is a cuboctahedron (see Fig.D.1(a)).

(a)   (b)
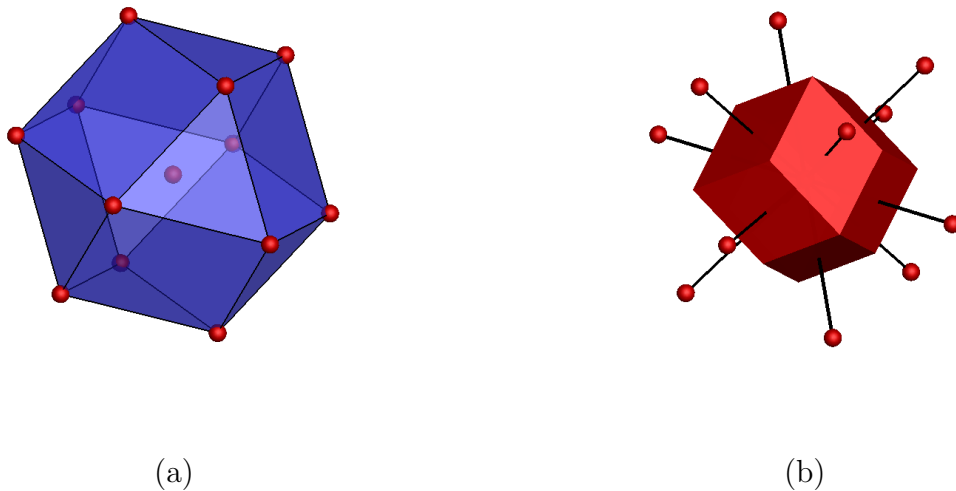
Figure D.1: (a) unit cell of FCC crystal lattice; (b) unit cell of FCC dual-lattice.

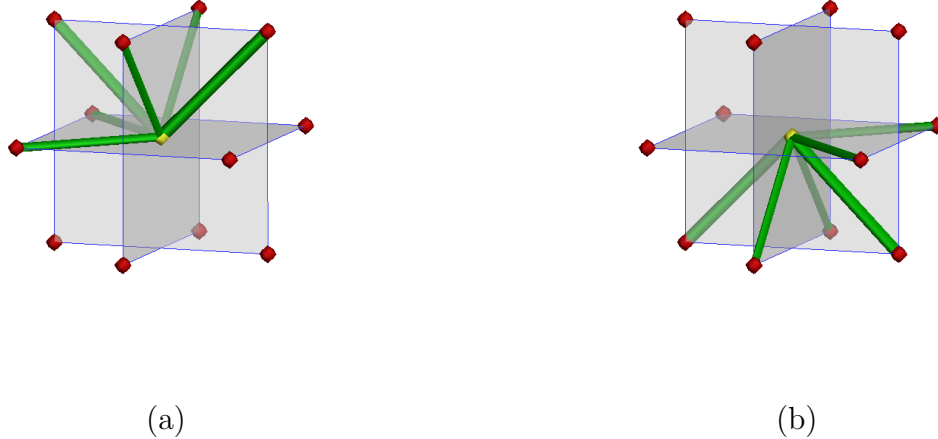(a)   (b)

Figure D.2: (a) upper six prism elements (second-order process zones); (b) lower six prism elements.

The similar construction procedure of a three-dimensional FCC dual-lattice process zone tessellation is shown as follows. Based on representative atoms, the Voronoi-Dirichlet Polyhedron (VDP) can be determined and is labeled as the highest order process zone element in the MCDD theory. The square prism element is termed as 2nd-order process zone, the wedge element is termed as 1st-order process zone and the bulk element is termed as 0th-order process zone.

Due to the specialties of the rhombic dodecahedron as the VDP of FCC crystal structure, 12 facets of the highest order process zone element (rhombic dodecahedron element) denote 12 square prism elements needed to fill in the gaps of facet-to-facet of rhombic dodecahedron elements (see Fig.D.2 and Fig.D.3(a)) and 24 edges of rhombic dodecahedron element denote 24 wedge elements needed to fill in the gaps of edge-to-edge of rhombic dodecahedron elements (see Fig.D.3(b)-(e)), and 14 vertices of rhombic dodecahedron denote 14 bulk elements (8 tetrahedron and 6 pentahedron elements) needed to fill in the gaps of the vertex-to-vertex of rhombic dodecahedron elements (see Fig.D.3(f)-(l)).

For a dual-lattice tessellation unit cell of Face-centered Cubic crystal, there are 13 rhombic dodecahedron elements (one locates at the centre of the dual-lattice structure and other 14 represent the nearest atom shell locations); Besides, a rhombic dodecahedron element has totally 12 facets therefore corresponding 3D square prism elements are needed; Finally 24 wedge elements (see Fig.D.3(b)-(e)) and 14 bulk elements including 8 tetrahedron and 6 pentahedron elements (see Fig.D.3(f)-(l)) will cover the remained void space.

The vertex-to-vertex between rhombic dodecahedron element and square prism element, the edge-to-edge between rhombic dodecahedron element and wedge element, the facet-to-facet between rhombic dodecahedron element and prism element are shown in Fig.D.4.
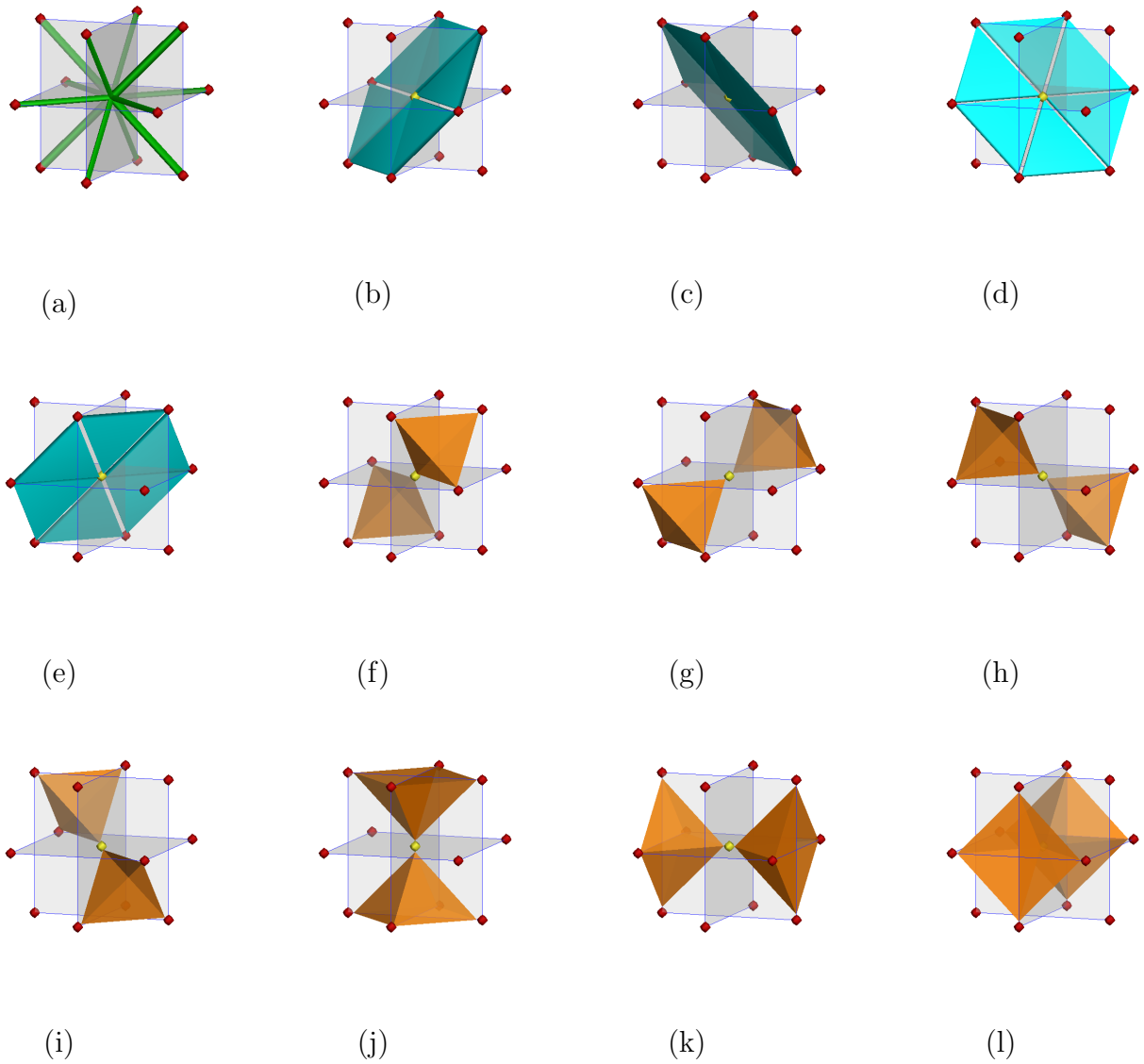
Figure D.3: Components of FCC dual lattice tessellation unit cell: (a) four wedge element
sets and each set has six wedge elements ((b)-(e)); and seven bulk element sets and each set
has two bulk elements ((f)-(l)).

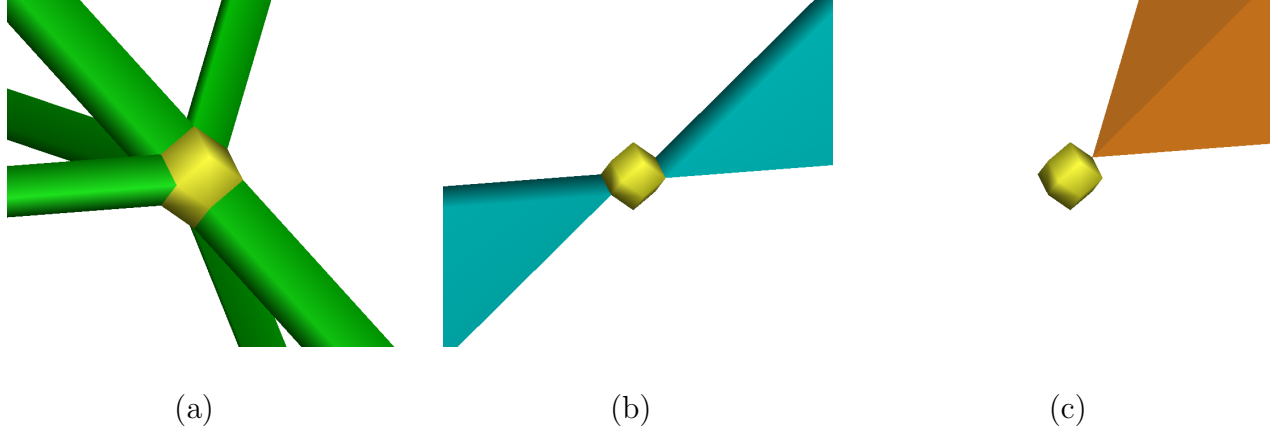<div align="center">(a)   (b)   (c)</div>

Figure D.4: Detailed connections of 3rd-order process zone in FCC crystals with: (a) 2nd-order process zone (prism element); (b) 1st-order process zone (wedge element); (c) 0th-order process zone (bulk element).

D.2   Discrete crystal defect model for FCC crystals

The super dual-lattice tessellation for a Face-centered Cubic (FCC) crystal lattice will be discussed. The lattice basis in FCC crystal lattice is introduced as shown in Fig.D.5(a),

$$a_1 = \left(0, \frac{a}{2}, \frac{a}{2}\right), a_2 = \left(\frac{a}{2}, 0, \frac{a}{2}\right), \text{ and } a_3 = \left(\frac{a}{2}, \frac{a}{2}, 0\right)$$

Secondly, the "super" lattice (see Fig.D.5(c)) created has proportional size to a regular crystal lattice, a coefficient β_1 is introduced to change basis vectors,

$$b_i = \beta_1 a_i, \quad i = 1, 2, 3 \quad \beta_1 > 1$$

Thirdly, the dual lattice of Face-centered Cubic crystal is chosen as a frame of super lattice sites and accordingly the coordinate of each vertex is,

$$\varepsilon_1 = a\,(1, 1, 1), \quad \varepsilon_2 = a\,(-1, 1, 1), \quad \varepsilon_3 = a\,(1, -1, 1), \quad \varepsilon_4 = a\,(-1, -1, 1)$$
$$\varepsilon_5 = a\,(1, 1, -1), \quad \varepsilon_6 = a\,(-1, 1, -1), \quad \varepsilon_7 = a\,(1, -1, -1), \quad \varepsilon_8 = a\,(-1, -1, -1)$$
$$\varepsilon_9 = a\,(0, 0, 2), \quad \varepsilon_{10} = a\,(0, 0, -2), \quad \varepsilon_{11} = a\,(0, 2, 0), \quad \varepsilon_{12} = a\,(0, -2, 0)$$
$$\varepsilon_{13} = a\,(2, 0, 0), \quad \varepsilon_{14} = a\,(-2, 0, 0)$$

and the scaled Voronoi-Dirichlet Polyhedron (VDP) cell of FCC crystals (see Fig.D.5(b)) is placed at each super lattice site. The scalability of VDP cell is described as $r_i = \beta_2 \varepsilon_i, \quad \beta_2 > 0$. The location of each atom in the super lattice can be labelled as $l \pm \epsilon_i, i = 1, 2, \cdots, 6$, as shown in Fig.D.5(c) in which

$$\epsilon_1 = (0, 1, 1), \quad \epsilon_2 = (1, 0, 1), \quad \epsilon_3 = (1, 1, 0)$$
$$\epsilon_4 = (1, -1, 0), \quad \epsilon_5 = (1, 0, -1), \quad \epsilon_6 = (0, 1, -1)$$

Also the coordinate of each vertex in FCC super dual lattice mesh is denoted as

$$x(l) = l^j \boldsymbol{b}, \text{ and } x(l, \epsilon_i) = l^j \boldsymbol{b} + r_i, \quad i = 1, 2, \cdots, 14$$

in which, l^j denotes $l \pm \epsilon_j$ and $\boldsymbol{b} = (b_1, b_2, b_3)$.
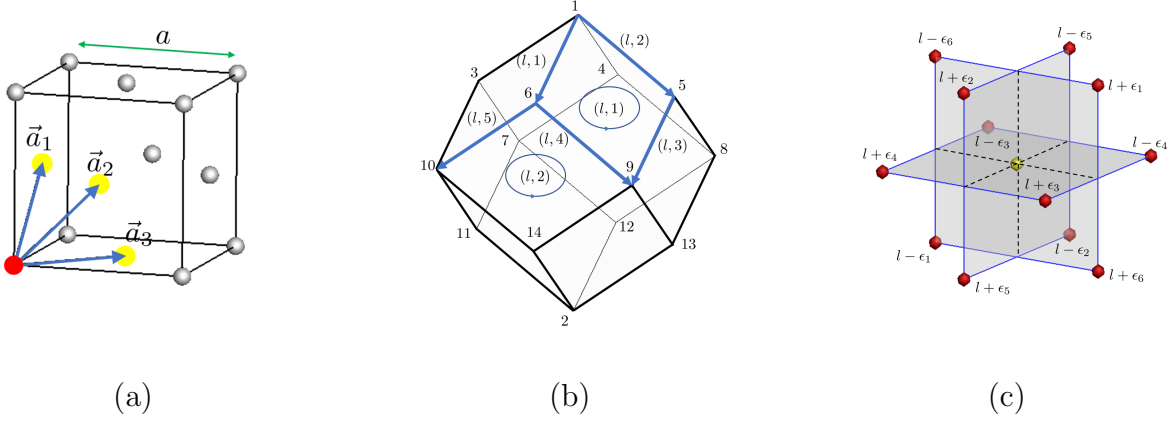

| (a) | (b) | (c) |

Figure D.5: Exterior calculus on super dual-lattice complex: (a) Face-centered Cubic crystal lattice basis; (b) the scaled Voronoi-Dirichlet Polyhedral (rhombic dodecahedron) cell at lattice site l; (c) neighboring scaled VDPs position numbering in a super dual-lattice tessellation unit cell.

Accordingly, each scaled VDP cell will sit at each lattice site of Face-centered Cubic crystal super lattice. The gaps or remained spaces among them can be filled by other 3D polytopal complexes without overlapping. The way of combining different polytopal complexes is through surface-to-surface (prism cell and rhombic dodecahedron cell), edge-to-edge (wedge cell and rhombic dodecahedron cell) and vertex-to-vertex (bulk cell and rhombic dodecahedron cell) connection.

We applied consistent symbols $\tau_j^i(l(\ell), m)$ to describe the relations among different 3D polytopal complexes as follows. For example, for central scaled rhombic dodecahedron $\tau_3^3(l)$, we have

$$\begin{align} \partial\tau_3^1(l, 1) &= \tau_3^0(l, 6) - \tau_3^0(l, 1) \tag{D.1} \\ \partial\tau_3^2(l, 1) &= \tau_3^1(l, 1) + \tau_3^1(l, 2) - \tau_3^1(l, 3) - \tau_3^1(l, 4) \tag{D.2} \end{align}$$

and

$$\begin{align} \partial\tau_3^2(l, 1) = {}& \tau_3^2(l, 1) + \tau_3^2(l, 2) - \tau_3^2(l, 3) + \tau_3^2(l, 4) - \tau_3^2(l, 5) \\ & - \tau_3^2(l, 6) + \tau_3^2(l, 7) + \tau_3^2(l, 8) - \tau_3^2(l, 9) \\ & - \tau_3^2(l, 10) + \tau_3^2(l, 11) + \tau_3^2(l, 12) \tag{D.3} \end{align}$$
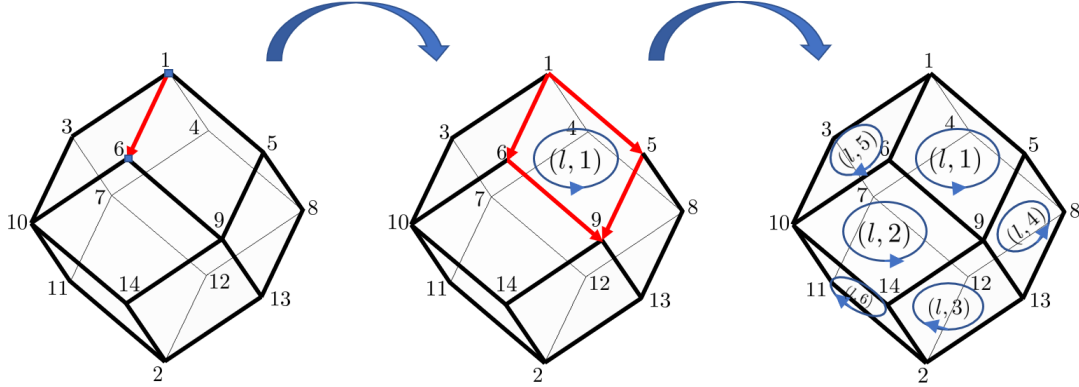
which are shown in Fig.D.6.

Figure D.6: Boundary operator illustration:from vertex to edge, from edge to surface, from surface to volume

The co-boundary δ is used to define the relations among different types of elements. For example, for the central scaled rhombic dodecahedron $\tau_3^3(l)$, we have

$$\delta\tau_3^0(l,2) = \tau_3^1(l,1) + \tau_3^1(l,2) + \tau_3^1(l,3) + \tau_2^1(l(1),3) + \tau_2^1(l(2),2) + \tau_2^1(l(3),1) \quad \text{(D.4)}$$

$$\delta\tau_3^1(l,3) = -\tau_3^2(l(2),1) - \tau_3^2(l(3),2) - \tau_3^2(l,3) - \tau_3^2(l,4) \quad \text{(D.5)}$$

$$\delta\tau_3^2(l,2) = \tau_3^3(l) - \tau_2^3(l,1) \quad \text{(D.6)}$$

which established the links from vertex to edge, from edge to surface and surface to volumes as shown in Fig.D.7.
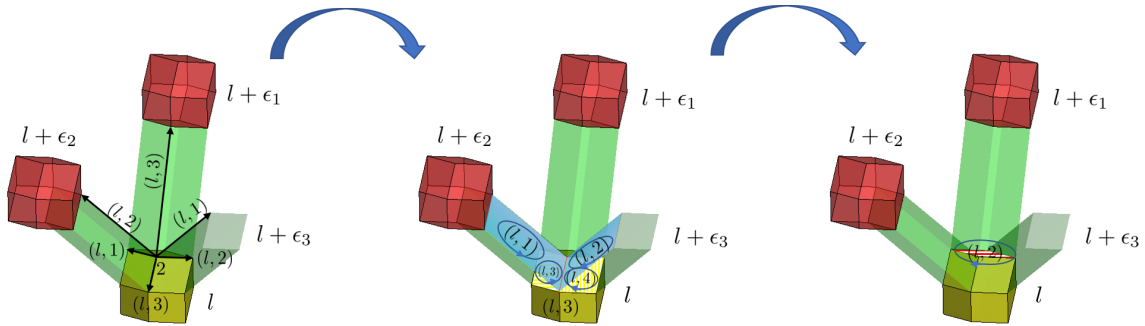

Figure D.7: Co-boundary operator illustration: from edge to vertex, from surface to edge, from volume to surface

Furthermore, we can also apply the cell complex notation defined above to represent other types of elements. For example, the prism element $\tau_2^3(l,m), m = 1, 2, \cdots, 12$, (see Fig.D.8(a)). We write the exterior representation by using boundary operator as shown

in Fig.D.8(b),

$$\partial \tau_2^1(l(2), 1) = -\tau_3^0(l, 2) + \tau_3^0(l + \epsilon_2, 7) \tag{D.7}$$

$$\partial \tau_2^1(l(2), 2) = -\tau_3^0(l, 14) + \tau_3^0(l + \epsilon_2, 11) \tag{D.8}$$

in which, $\tau_3^0(l+\epsilon_2, j)$ denotes it is the j-th vertex $j = 1, 2, \cdots, 14$ of on the $l \pm \epsilon_i, i = 1, 2, \cdots, 6$ polytopal cell. Also we have (shown in Fig.D.8(c)-(d)),

$$\partial \tau_2^2(l(2), 1) = \tau_2^1(l(2), 2) - \tau_3^1(l + \epsilon_2, 15) - \tau_2^1(l(2), 1) + \tau_3^1(l, 9) \tag{D.9}$$

$$\partial \tau_2^3(l, 2) = \tau_2^2(l(2), 1) + \tau_2^2(l(2), 2) + \tau_2^2(l(2), 3) - \tau_2^2(l(2), 4) - \tau_3^2(l, 4) \tag{D.10}$$

$$+ \tau_3^2(l + \epsilon_2, 9) \tag{D.11}$$

The wedge complex cell (1st-order process zone), $\tau_1^3(l, m), m = 1, 2, \cdots, 24$, (see Fig.D.9(a)) is discussed here. The geometry of the wedge complex cell can be described by topology boundary operator. For example, from vertex to edge (as shown in Fig.D.9(b))

$$\partial \tau_1^1(l(1), 1) = -\tau_3^0(l, 2) + \tau_3^0(l + \epsilon_1, 8) \tag{D.12}$$

$$\partial \tau_1^1(l(1), 2) = -\tau_3^0(l, 2) + \tau_3^0(l + \epsilon_2, 7) \tag{D.13}$$

And from edge to surface, surface to volume (as shown in Fig.D.9(c)-(d))

$$\partial \tau_1^2(l(1), 1) = \tau_1^1(l(1), 2) - \tau_1^1(l(1), 1) + \tau_1^1(l(1), 3) \tag{D.14}$$

$$\partial \tau_1^3(l, 1) = \tau_1^2(l(1), 1) - \tau_1^2(l(1), 2) - \tau_1^2(l(1), 3) \tag{D.15}$$

$$- \tau_1^2(l(1), 4) + \tau_1^2(l(1), 5) \tag{D.16}$$

The bulk complex cell is discussed here. Different from other polytopal complexes, the bulk complex cell in FCC dual lattice tessellation includes tetrahedron and pentahedron. The tetrahedron is simplex and a pentahedron can be divided into two tetrahedron. In each rhombic dodecahedron complex cell, 14 vertices correspond to 14 bulk complex cells (0th-order process zone), i.e. $\tau_0^3(l, m), m = 1, 2, \cdots, 14$, (see Fig.D.10(a)). The geometry of a bulk complex cell is described by topology boundary operator. For example, from vertex to edge (as shown in Fig.D.10(b)),
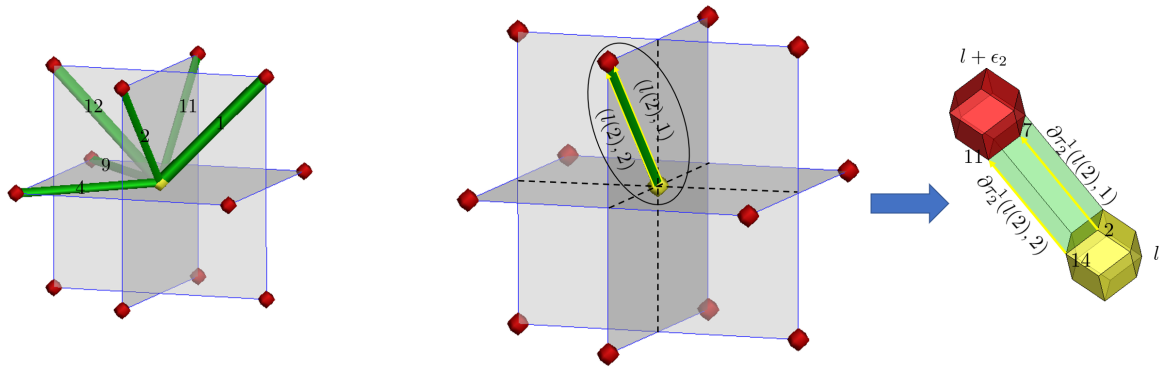
$$\partial \tau_0^1(l(1), 1) = -\tau_3^0(l + \epsilon_3, 5) + \tau_3^0(l + \epsilon_1, 8) \tag{D.17}$$

$$\partial \tau_0^1(l(1), 2) = -\tau_3^0(l + \epsilon_3, 5) + \tau_3^0(l + \epsilon_2, 7) \tag{D.18}$$

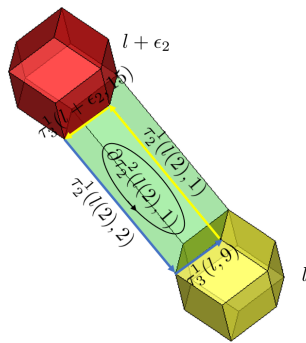And from edge to surface, from surface to volume (see Fig.D.10(c)-(d)),

$$\partial \tau_0^2(l(1), 1) = \tau_0^1(l(1), 2) + \tau_0^1(l(1), 3) - \tau_0^1(l(1), 1) \tag{D.19}$$

$$\partial \tau_0^3(l, 1) = -\tau_0^2(l(1), 1) + \tau_0^2(l(1), 2) + \tau_0^2(l(1), 3) - \tau_0^2(l(1), 4) \tag{D.20}$$
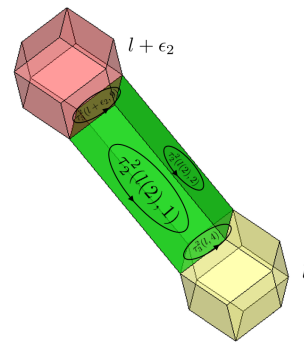
(a)

(b)

(c)

(d)

Figure D.8: Boundary operator on prism element: (a) prism cells (2nd-order process zone);
(b) from vertex to edge; (c) from edge to surface; (d) from surface to volume.
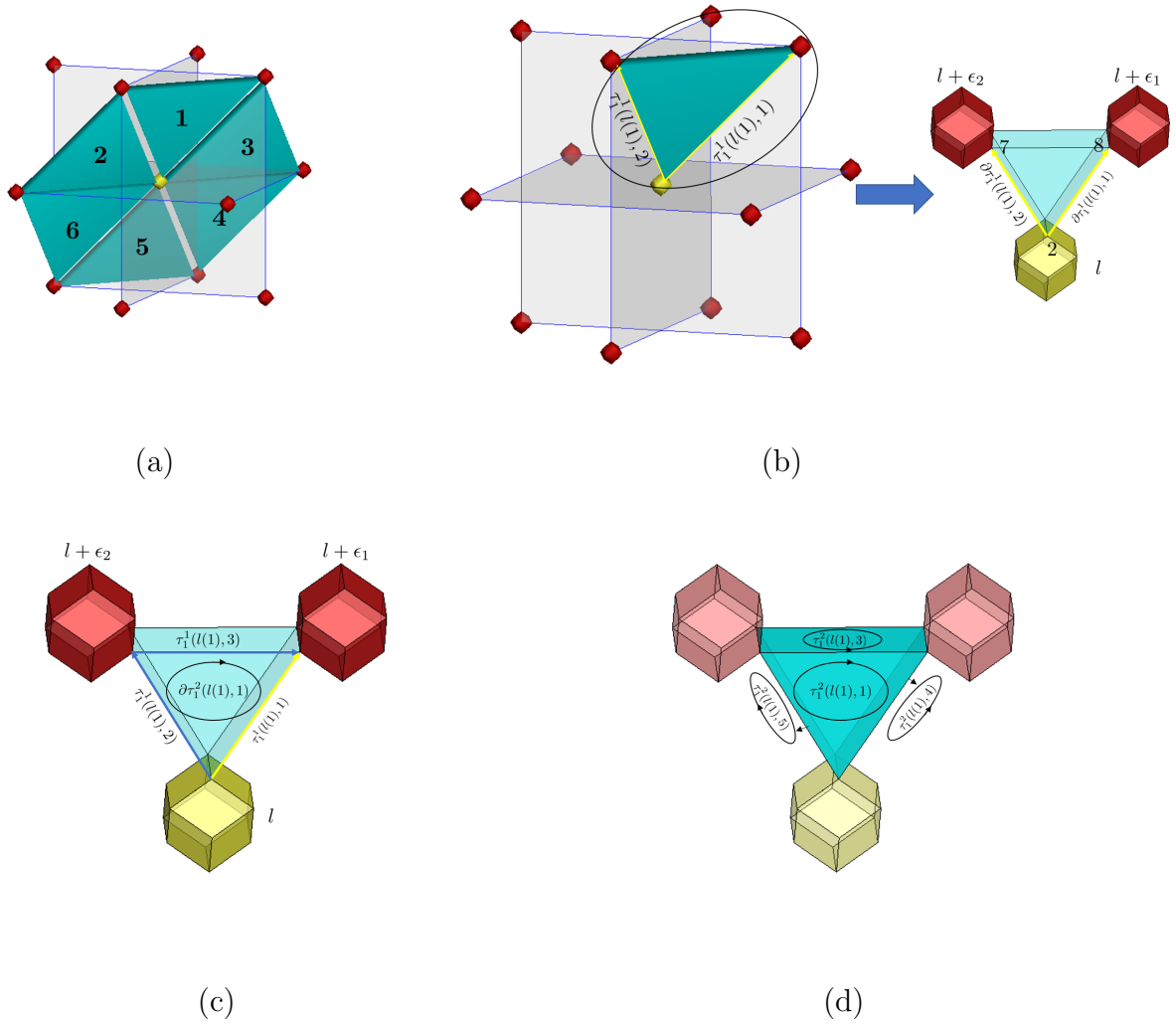
(a)

(b)

(c)

(d)

Figure D.9: Boundary operator on wedge element: (a) 1st-order process zone (wedge) elements; (b) from vertex to edge; (c) from edge to surface; (d) from surface to volume.
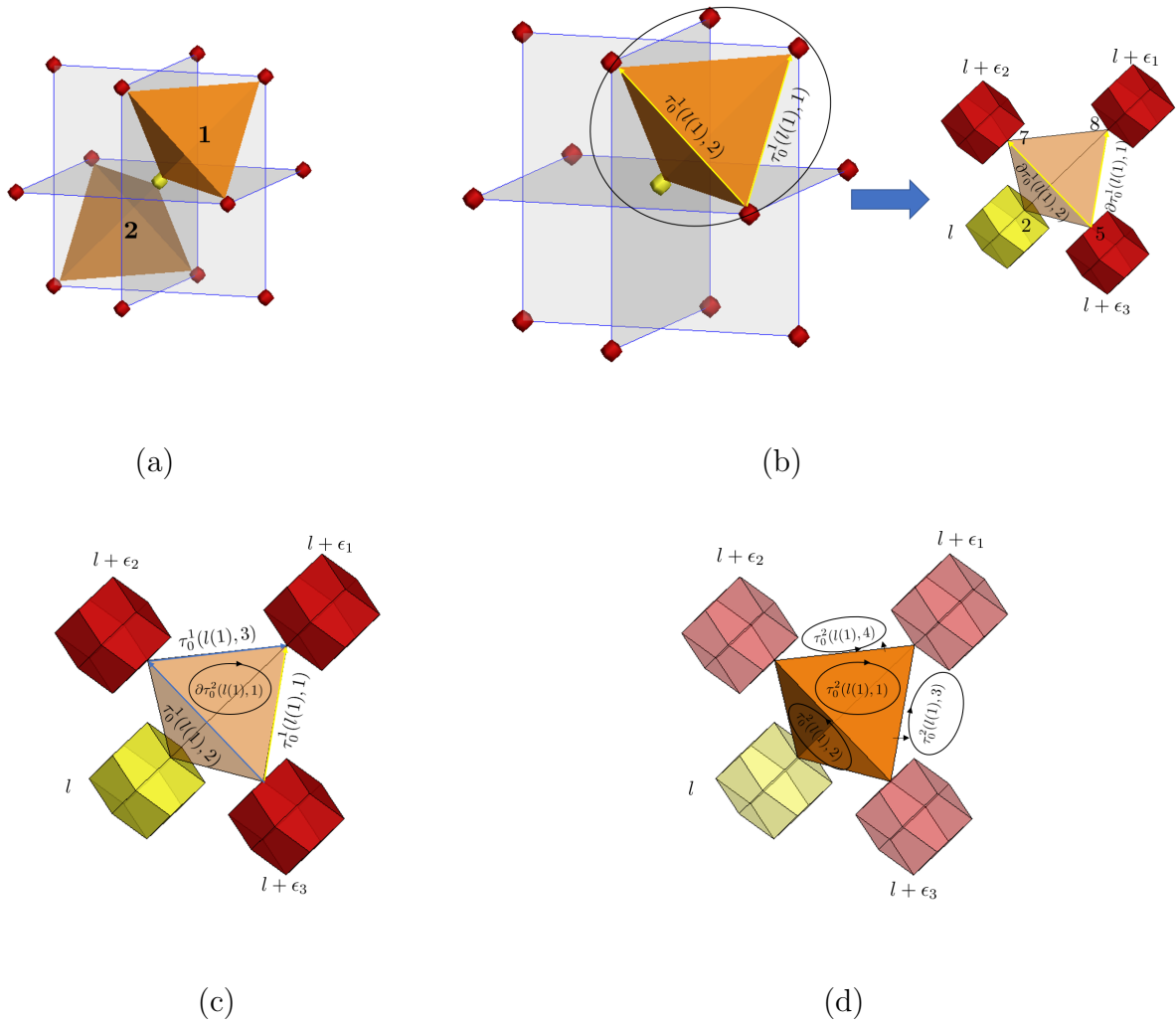
(a)

(b)

(c)

(d)

Figure D.10: Boundary operator on bulk element: (a) 0th-order process zone (bulk) elements; (b) from vertex to edge; (c) from edge to surface; (d) from surface to volume.